NUCLEAR STRUCTURE NEAR N=Z=28: STUDY OF NEUTRON-DEFICIENT NICKEL ISOTOPES VIA ONE-NEUTRON KNOCKOUT AND INTERMEDIATE-ENERGY COULOMB EXCITATION

By

Kathleen Louise Miller

A DISSERTATION

Submitted to
Michigan State University
in partial fulfillment of the requirements
for the degree of

DOCTOR OF PHILOSOPHY

Department of Physics and Astronomy

2003

ABSTRACT

NUCLEAR STRUCTURE NEAR N=Z=28: STUDY OF NEUTRON-DEFICIENT NICKEL ISOTOPES VIA ONE-NEUTRON KNOCKOUT AND INTERMEDIATE-ENERGY COULOMB EXCITATION

By

Kathleen Louise Miller

Two experiments were performed at the National Superconducting Cyclotron Laboratory to study nuclear structure in the vicinity of the $N = Z = 28$ doubly-magic shell closure. The ^{56}Ni nucleus is the lightest radioactive doubly-closed-shell nucleus. Previous measurements of large reduced transition probabilities to the first excited state of ^{56}Ni have suggested that the properties of radioactive doubly-magic nuclei may not mirror those of stable closed-shell nuclei.

The single-particle structure of the neighboring nucleus ^{57}Ni was studied via one-neutron knockout. Spectroscopic factors of $C^2S = 0.56(11)$ to the ground state and $C^2S = 4.3(3)$ to excited states of the core fragment ^{56}Ni were measured for the ground state of ^{57}Ni. The measured spectroscopic factors only exhaust 50–60% of those predicted by the nuclear shell model. The measured reductions are consistent with those observed from other nucleon-knockout and electron scattering experiments on well-bound stable nuclei. In addition to other known excited states, an excited state in ^{56}Ni was observed at 5661(72) keV with de-excitation gamma rays of 1726(10) keV and 3027(71) keV. This confirms the existence of a state previously suggested at 5668 keV, but due to angular momentum selection rules does not agree with the suggested spin and parity of $J^\pi = 6^+$.

The excited states and reduced transition probabilities for the nuclei ^{52}Fe and ^{54,55,56,58}Ni were measured in an intermediate-energy Coulomb excitation experiment. A $B(E2\uparrow)$ of 494(119) e^2fm^4 to the first excited state of ^{56}Ni was measured, and a weighted average of 548(51) e^2fm^4 for the three previous measurements and the

current measurement was determined. The average value was found to disagree with a theoretical prediction which assumed a structure for ^{56}Ni like that for the doubly-magic stable nuclei. An energy of 1396(5) keV for the first excited state of ^{54}Ni was measured for the first time. The transition probability to the first excited state was measured to be $B(E2\uparrow) = 626(169)$ e^{2}fm^4. The energy of the excited state and $B(E2\uparrow)$ for ^{54}Ni are both comparable to the same quantities for the mirror nucleus ^{54}Fe. A shell model calculation predicted that the transition probability for ^{54}Ni would be lower than that for doubly-magic ^{56}Ni, while the opposite trend was observed. The doubly-magic status of the ^{56}Ni nucleus is reinforced, although the disagreement between the shell-model predictions and measured transition probabilities for ^{56}Ni still leave the strength of the $N = Z = 28$ shell closure in question.

A reduced transition probability of $B(E2\uparrow) = 817(102)$ e^{2}fm^4 to the first excited state of ^{52}Fe was measured for the first time, and the increase in $B(E2\uparrow)$ with respect to ^{54}Fe agrees with shell-model expectations. The transition strength to an excited state of ^{55}Ni with a de-excitation gamma ray at 2879(10) keV was observed. The spin and parity of the associated excited state at 2888(7) keV was unknown, thus transition probabilities were calculated for excited states with $J^\pi = 9/2^-$ and $J^\pi = 11/2^-$. Both transition probabilities were higher than those predicted in a shell model calculation, possibly explained by the existence of an unobserved gamma-ray doublet or feeding from higher-lying states.

to my family, all my love and thanks

ACKNOWLEDGMENTS

I am indebted to many people for helping me during my time as a graduate student at MSU and the NSCL. First I would like to thank my advisor Thomas Glasmacher, whose support and advice made my graduate career possible. I am grateful to Thomas for his willingness to explain the intricacies of nuclear physics and the associated politics, for allowing me to pursue opportunities as they arose during my graduate career, and for reminding me often of what is important in research and in life.

I would like to thank Gregers Hansen for his advice and help with the analysis of the knockout experiment, and for serving as a member of my guidance committee.

The members of the "knockout" group - most notably Navin, Valentina, Joachim and Russ - struggled with me through my first data analysis and the delights of VMS and the PAW program, for which I am very grateful.

The Gamma Group has changed quite a bit since I arrived in '98 - especially the female/male ratio! I thank all the members, past and present, for their invaluable assistance. Thanks to those who helped me learn how to survive in Thomas' group - how to order parts, get from the Baymont Hotel to the Atlas accelerator, sit through daily meetings, and most importantly how to use the LabelShop labelmaker. Thanks to those who assisted with my thesis experiments - sitting shifts, updating web pages, and answering filling alarms. I hope that second "automatic" filling system is done soon!

Many thanks to Heather Olliver for her development of the Mathematica notebook to calculate angular distributions, Coulomb excitation cross sections, and B(Eλ,Mλ); Wilhelm Mueller for his development of the GEANT simulations for SeGA; Ryan Clement for his development of the Mathematica notebook to determine measured efficiencies; and Russ Terry for the FORTRAN function to fit the efficiency calibration gamma rays.

Special thanks to Alex Brown, Wayne Repko, and Simon Billinge for serving on

my guidance committee.

Without the support of the NSCL staff members, none of this would have been possible. I would like to express my gratitude to all members of the NSCL community who helped in the preparation, running, and analysis of my thesis experiments.

I am grateful to the National Science Foundation and the Michigan State University Distinguished Fellowship Program for their financial support.

Without my fellow graduate students, my graduate student career would have been much more difficult and much more boring. Jen, CA, Cluze, Steve, Joy, Josh, and Dan P., thanks for getting me through my first few years in Michigan. Without some of you I never would have discovered MSU basketball! Thanks especially to Jen and Steve for putting up with me as a roommate. Thanks to my "NSCL friends" Pat, Joann, Don, Barry, Valentina, Heather, Michelle, Dan G., Jennychurch, Mark, Paul, Russ and the rest of the atrium and Peanut Barrel lunch crews for the great discussions about everything from the USDA food pyramid and obscure sci-fi television shows to flesh-eating pineapple enzymes and children's tv theme songs. Pat, thanks for befriending me upon my arrival at the NSCL and sharing Sesame Street memories. Joann, I will always remember the trip out west - flashlight fury, outhouse fear and Buffalo Bill. Heather, thanks so much for helping me through my thesis experiment and the whole last year, for being willing to chat in the office when I needed to, and for reading my thesis! Michelle, thanks for being my aerobics buddy and for lending an ear when I needed to talk. Thanks to all of you for being great friends.

I would like to thank my family, without whom there would be much less laughter in my life. Their support has made all the difference.

And finally, thanks to Adam. As the one-and-a-half years stretched into two, and then two-and-a-half, thanks for all your support, the many hours on the phone and webcam and Yahoo! Messenger, and your love.

Contents

List of Figures

IMAGES IN THIS DISSERTATION ARE PRESENTED IN COLOR.

List of Tables

Chapter 1

Introduction

1.1 The study of nuclear structure

The atomic nucleus is a system composed of nucleons bound together by the strong force. Protons with charge e and neutrons with zero charge are treated theoretically as different states of the nucleon. Elements are named according to proton number Z, and nuclei are further characterized by the number of neutrons N and the mass number $A = N + Z$. Nuclei with the same Z but different N are isotopes, while those with the same N and different Z are isotones.

The goals of the study of nuclear physics are to understand the force between nucleons, the structure of nuclei, and the nature of nuclear interactions with each other and with other subatomic particles. Nuclear structure research focuses on properties of nuclei such as the energies of excited states, nuclear shapes, electromagnetic moments and transition rates between excited states and the ground state, and how nuclei transform into different nuclei. Transformations between nuclei can occur through the processes of β decay, fission, fusion, and nucleon transfer. Experimental techniques used to study nuclear structure include Coulomb excitation, β decay, fusion-evaporation reactions, transfer reactions, Coulomb dissociation, and breakup reactions. In addition to providing information about the structure of individual nu-

clei, nuclear structure studies provide experimental information that can be used by theorists to explain the nature of nuclear forces.

Experimental nuclear physics initially focused on stable nuclei, which comprise only about 300 of the 10,000 nuclei predicted to exist. With the advent of facilities capable of producing radioactive beams with sufficient intensity for study, the focus of many experimentalists has turned to studying such radioactive, or "exotic," nuclei. At radioactive beam facilities, nuclei are studied in inverse kinematics. A beam of the exotic nucleus of interest is created which interacts with a stationary target of stable nuclei. The target nuclei are used to induce the type of reaction under study. The target can be used to add nucleons to, or remove nucleons from, the radioactive nucleus to induce a transformation to another nucleus. As an example, the one-nucleon knockout technique uses a light stable target to remove one nucleon from the radioactive nucleus of interest, to study both the wavefunction of the initial nucleus and the excited state structure of the final nucleus. One-nucleon knockout on the radioactive nucleus ^{57}Ni is discussed in Chapter 2. The target can alternately be used to inject energy into a nucleus to promote it to an excited state. The behavior of the nucleus as it de-excites is subsequently observed. An example of such a technique is intermediate-energy Coulomb excitation. In this technique, discussed in detail in Chapter 3, the stable target nuclei are used to excite the radioactive nucleus of interest via the well-understood electromagnetic force, and de-excitation gamma rays are measured to determine transition rates between states.

1.2 The nuclear shell model

There have been many attempts to explain the structure of nuclei since the discovery of the nucleus at the beginning of the 20th century. While the strong force plays the dominant role in the forces between nucleons, the electromagnetic and weak forces also influence the nucleons' interaction. However, unlike the electromagnetic force,

the residual strong force between nucleons is still poorly understood. Thus nuclear models, or simplified views of nuclear structure which contain the essentials of nuclear physics, have been developed to explain the behavior of stable and radioactive nuclei. A successful model must account for previously measured nuclear properties and be able to make reasonably accurate predictions for future measurements. The models of nuclear structure developed to date fall into two categories, collective and microscopic.

Collective models focus on the behavior of the nucleons as they act together. The vibrational model, where nuclear excited states are described by the vibration of the nucleons as a whole, is one example of a collective model. Another example is the rotational model, where excitations are induced by the rotation of statically-deformed nuclei.

Microscopic models describe the nucleus in terms of the individual degrees of freedom of the nucleons, as opposed to collective degrees of freedom for all A nucleons. The most well-known microscopic model of nuclear structure is the nuclear shell model. In this model, the individual nucleons move in a potential created by all other $A - 1$ nucleons. This potential is also called the mean field, and various forms for the potential have been used in an attempt to describe observed nuclear structure trends. For example, there are large energy gaps between groupings of energy levels (shells) in the single-particle energy spectrum. If the isotropic, three-dimensional harmonic oscillator potential is used for the mean field, the first few magic numbers, or numbers of nucleons needed to fill the last shell before a large energy gap, are 2, 8, 20, and 40. Experimental evidence reveals a different set of magic numbers, however, so the spin-orbit interaction was added to the harmonic oscillator potential to explain empirical evidence [1]. With the spin-orbit interaction, the magic numbers are 2, 8, 20, 28, 50, 82, and 126. The single-particle spectrum for the three-dimensional isotropic harmonic oscillator is shown in the left half of Figure 1.1, while that with the spin-orbit interaction included is shown in the right half. While the major shell gaps are indicated in the figure, minor shell gaps occur when shells that can hold a

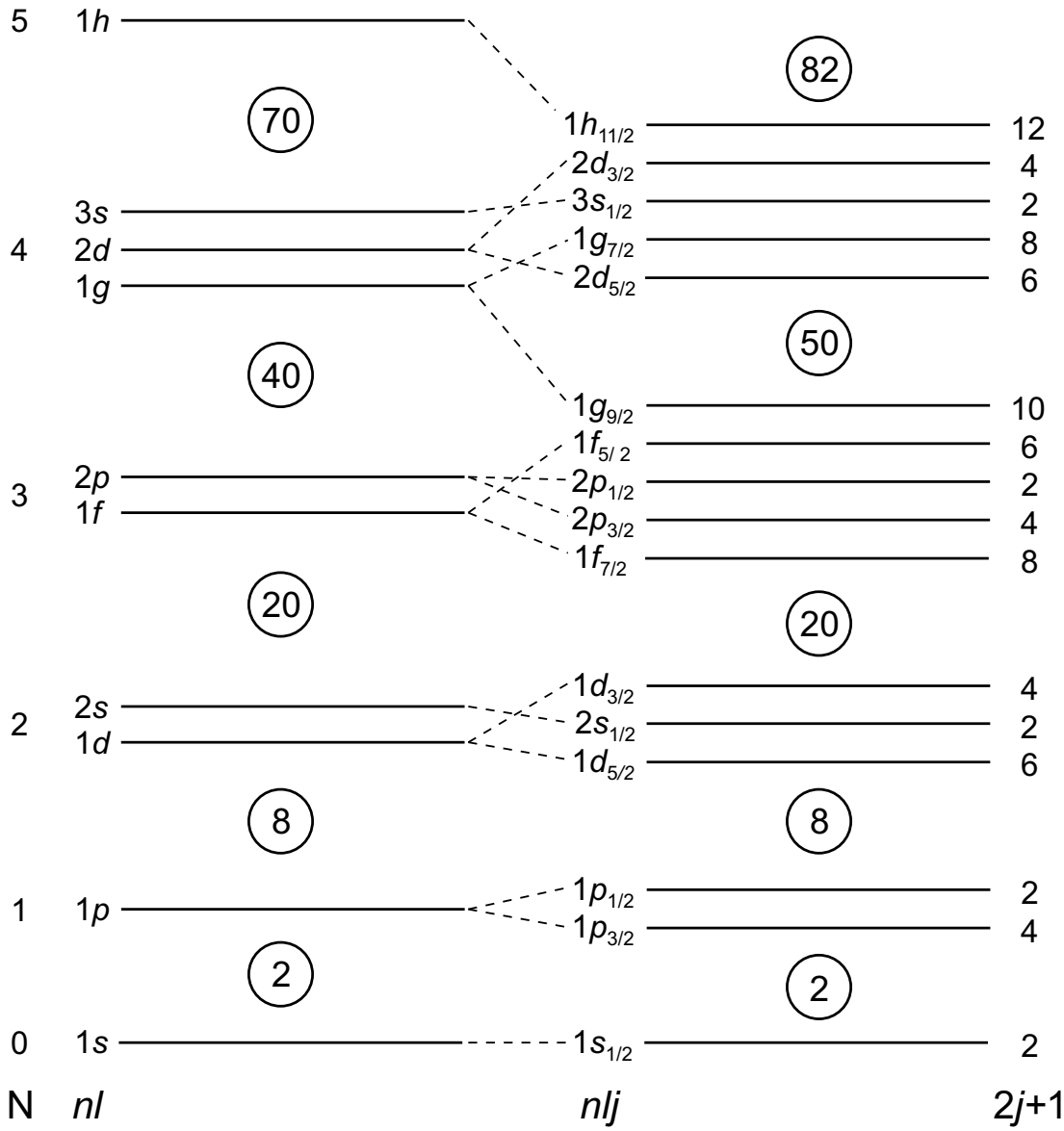

Figure 1.1: Schematic diagram of the single-particle spectrum for the spherical shell model, shown up to the $1h_{11/2}$ level. On the left is shown the single-particle spectrum produced by an isotropic, three-dimensional harmonic oscillator potential. On the right is the single-particle spectrum with the spin-orbit interaction included. N is the number of harmonic oscillator quanta in a major shell. The angular momentum l is represented by the labels s, p, d, f, g, h, corresponding to $l = 0, 1, 2, 3, 4, 5$. The number of occurrences of a particular l value is labeled by n, in ascending order according to energy. The projection of the total spin $\mathbf{j} = \mathbf{l} + \mathbf{s}$ of the shell is j. The magic numbers are indicated between each major shell gap.

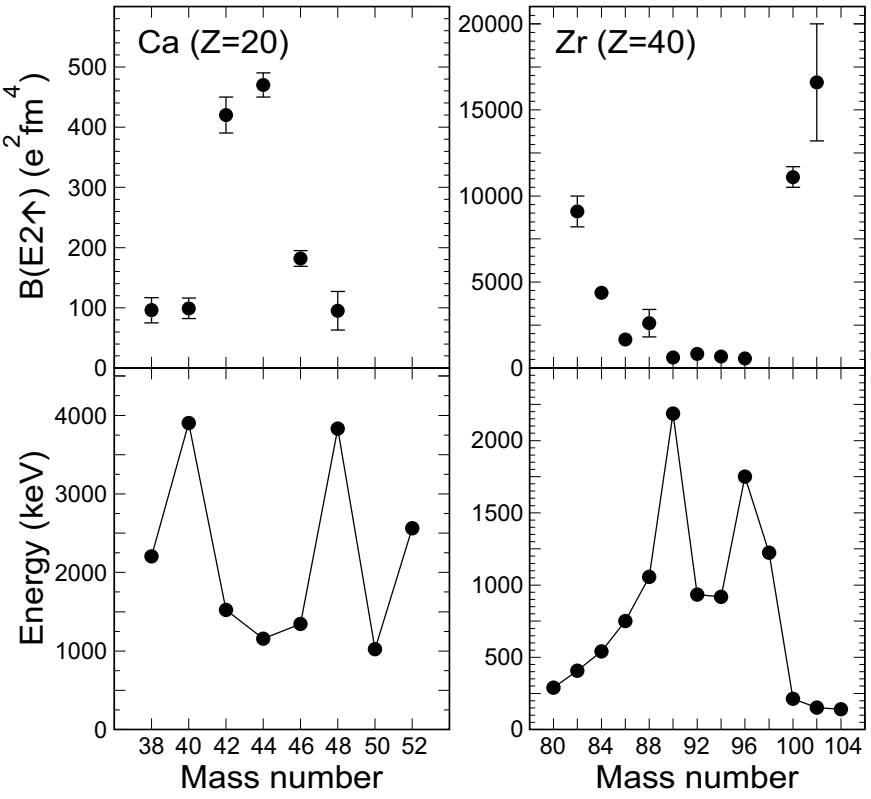

Figure 1.2: Reduced transition probability $B(E2\uparrow)$ to the first ($J^\pi = 2^+$) excited state (top) and corresponding excitation energy (bottom) for even-even isotopes of Ca and Zr. Data are taken from [3].

large number of nucleons are filled, such as at the magic numbers 28, 40, and 56.

The best evidence for single-particle behavior is found near magic (also called closed-shell) nuclei, where the number of protons and/or neutrons in a nucleus fills the last shell before a major or minor shell gap. For example, the nucleus ^{17}O can be modeled as a doubly-magic ^{16}O core ($N = Z = 8$), with one additional (valence) neutron in the $1d_{5/2}$ level. The ground-state spin and parity of ^{17}O is $J^\pi = 5/2^+$ [2], which corresponds to the spin and parity of the level where the valence neutron resides. The spin J is equal to the projection of $\mathbf{J} = \mathbf{l} + \mathbf{s}$, and the parity π is equal to $(-1)^l$. The independent-particle shell model would predict that the first excited state of ^{17}O has $J^\pi = 1/2^+$, which corresponds to the promotion of the valence neutron to the next available shell, the $2s_{1/2}$ shell. Experimental measurements have shown that the first excited state of ^{17}O indeed has $J^\pi = 1/2^+$ [2].

Nuclei with magic numbers of both protons and neutrons are predicted to have special characteristics. These include a high energy of the first excited state, a large neutron and proton separation energy, and low reduced transition probability ($B(E2\uparrow)$ for $J^\pi = 2^+$) to the first excited state. Such trends have been experimentally observed. Systematics for reduced transition probability and energy of the first excited state for two isotope chains of Ca and Zr are shown in Figure 1.2. The elements Ca and Zr both have a magic number of protons, Ca with $Z = 20$ and Zr with $Z = 40$. As the number of neutrons for each element approaches a magic number, the reduced transition probability decreases. At a magic number of neutrons, the energy of the first excited state is much higher than that for the neighboring isotopes. Two doubly-magic isotopes are shown for Ca, ^{40}Ca with $N = Z = 20$ and ^{48}Ca with $N = 28$, $Z = 20$. In both cases the energy of the first excited state is markedly higher than that of the neighboring isotopes, while the $B(E2\uparrow)$ values are low. For the element Zr, large energies of the first excited state are apparent at $N = 50$ and 56. A major shell gap occurs at nucleon number 50, as shown in Figure 1.1. A minor shell gap also occurs at nucleon number 56, when the $2d_{5/2}$ shell is filled. Corresponding lower $B(E2\uparrow)$ values are apparent around the region of the two shell closures. For the mid-shell isotopes ^{44}Ca and ^{102}Zr, the energy of the first excited states is comparatively low, while the $B(E2\uparrow)$ values are high. Large $B(E2\uparrow)$ values are indicative of many nucleons acting together in a transition, a characteristic of collective behavior. The collective behavior such as vibrational and rotational excitations are usually evident in mid-shell nuclei.

1.3 Nuclear structure at $N = Z = 28$

The shell model discussed in the previous section was originally derived to explain existing experimental information on stable nuclei. Discoveries of phenomena such as the island of inversion [4,5] and halo nuclei [6] have shown that exotic nuclei may not

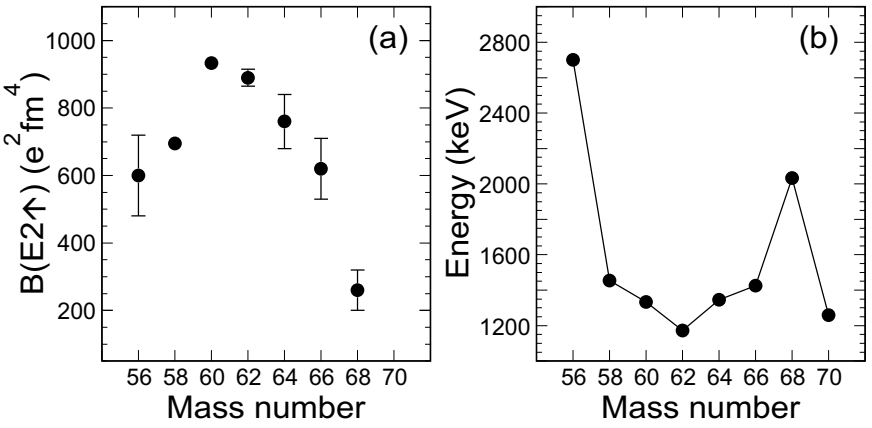

Figure 1.3: Reduced transition probability $B(E2\uparrow)$ to the first ($J^\pi = 2^+$) excited states (a) and corresponding excitation energies (b) for the even-even Ni isotopes. Data are taken from [3] and do not include results from the present work. The high energy of the first excited state of ^{56}Ni does not correspond to an expected low $B(E2\uparrow)$.

have the same structure as stable nuclei. The first magic number created with the inclusion of the spin-orbit interaction is 28. The magic number 28 is created by a minor shell gap between the $1f_{7/2}$ and $2p_{3/2}$ shells. The nucleus ^{56}Ni, with $N = Z = 28$, is the first radioactive doubly-magic nucleus. Studying the region around the $N = Z = 28$ shell closure provides some insight as to whether radioactive nuclei have the same magic numbers and shell structure as stable nuclei. The study of exotic nuclei near closed shells allows single-particle states to be investigated. In the present work, the Ni isotopes from ^{54}Ni to ^{58}Ni as well as ^{52}Fe were studied to investigate the evolution of nuclear structure for $N = 28$ and $Z = 28$ magic numbers.

For the doubly-magic $N = Z = 28$ nucleus ^{56}Ni, it is expected that the energy of the first excited state is high and the corresponding $B(E2\uparrow)$ to that state is low compared to the neighboring Ni isotopes. Systematics for the $B(E2\uparrow)$ values and energies of the first excited states for the even-even Ni isotopes are shown in Figure 1.3. A large energy of the first excited state occurs for ^{56}Ni ($N = 28$) and ^{68}Ni ($N = 40$), both doubly-closed-shell nuclei. The higher energy of the first excited state for ^{56}Ni does not correspond to a very low $B(E2\uparrow)$ to that state compared to ^{68}Ni, which has a lower energy of the first excited state but a significantly lower $B(E2\uparrow)$

to that state.

The energy of the first excited state of ^{56}Ni ($J^{\pi} = 2^{+}$) at 2700.6(7) keV [7] appears to agree with trends from stable doubly-magic nuclei such as ^{40}Ca and ^{90}Zr. The transition rate from the first excited state of ^{56}Ni to the ground state was first measured in 1973 using the Doppler-shift attenuation method (DSAM) [8]. An E2 transition rate ($B(E2\downarrow)$) to the 2700.6 keV state of 77(32) e^{2}fm^4 was observed. The corresponding transition probability $B(E2\uparrow) = 385(160)$ e^{2}fm^4 agreed with predictions based on the behavior of stable nuclei for a good-closed shell nucleus. A later shell-model calculation, which assumed a good closed-shell structure for the ^{56}Ni nucleus, calculated a $B(E2\uparrow)$ of 400 e^{2}fm^4 [9]. This lent further credence to the view that radioactive ^{56}Ni behaves like stable doubly-magic nuclei. The DSAM measurement had an uncertainty of almost 50%, however, so no definite conclusions could be made.

Advancements in radioactive beam facilities in the the early 1990's facilitated new measurements of the E2 transition strength for ^{56}Ni. The next measurements of the excitation strength to the first 2^{+} state of ^{56}Ni were higher than expected. In 1994 a $B(E2\uparrow)$ of 600(120) e^{2}fm^4 was measured via proton inelastic scattering [10], followed by an intermediate-energy Coulomb excitation measurement of 580(70) e^{2}fm^4 [11]. Both measurements were not in agreement with the predictions for a good closed shell structure for ^{56}Ni, indicating that the degree of collectivity was higher than that for a stable doubly-magic nucleus. These findings spurred more theoretical and experimental interest in the region. As advances in experimental facilities aided experimental interest in the ^{56}Ni region, advances in computing technology furthered shell-model calculations for the fp-shell nuclei.

Several experiments designed to study nuclear structure in the vicinity of the $N = Z = 28$ double-magic nucleus ^{56}Ni are discussed in this work. A nucleon-knockout experiment on the neighboring ^{57}Ni nucleus, which explores the structure of both ^{57}Ni and ^{56}Ni, is discussed in Chapter 2. An intermediate-energy Coulomb excitation

experiment to study the structure of the neutron-deficient nuclei ^{54,55,56}Ni and ^{52}Fe is discussed in Chapter 3.

Chapter 2

Structure of ^{56}Ni and ^{57}Ni via One-Neutron Knockout

2.1 The one-nucleon knockout technique

2.1.1 Background

The technique of nucleon knockout with exotic beams was first used to study the characteristics of halo nuclei, which have one or more weakly-bound nucleons and radii far larger than expected. Identified in 1985, the valence nucleons in halo nuclei are very weakly bound and thus have a large probability of existing far from the nuclear core. The wide spatial distribution of a halo nucleus translates into a narrow distribution in momentum space. In 1947, Serber applied the sudden approximation to the collision of the deuteron with a light nuclear target at high energy (95 MeV/nucleon) [12]. The deuteron, a nuclear system composed of only one proton and one neutron, has an average distance between the proton and neutron of 3.9 fm. Serber was interested in the study of neutron production in deuteron stripping reactions. The application of the sudden approximation implied that the removal of the neutron as a consequence of the interaction with the target would be essentially instantaneous. This instantaneous

removal of the neutron would leave the proton with the momentum it had prior to the collision. This model, that the momentum distribution of a projectile fragment (analogous to the proton in the deuteron case) is equal to the momentum distribution of the initial wave function, was later applied to halo nuclei.

The structure of the halo nuclei ^{8}B, ^{11}Be, ^{11}Li, and ^{19}C was explored using breakup methods [13–19]. Following breakup of the halo nucleus into a valence nucleon plus a core fragment, a heavy fragment with the mass and charge of the core was detected. The measured cross sections and momentum distributions were used to study the halo structure of the nucleus. The technique of one-nucleon knockout represented the next advance in measurements of nuclear structure through breakup. This technique, which is performed in inverse kinematics at beam energies of greater than 50 MeV/nucleon, allows for the use of semiclassical theories such as the eikonal model to assign angular momenta and determine spectroscopic factors. The nucleus of interest, with mass A, is incident on a light target, and the $(A-1)$ nuclear fragment is detected in a high-resolution spectrograph designed to provide an energy resolution of $E/\Delta E = 10,000$ and a momentum resolution of $p/\Delta p = 20,000$. The novel aspect of this technique is the detection of gamma rays associated with the de-excitation of the core fragment in coincidence with the fragment. This allows for an identification of cross sections and momentum distributions to different final states of the fragments. It was initally assumed that the measured cross section from breakup of halo nuclei was dominated by valence nucleon removal to the ground state of the core. Once it became possible to identify specific core states, it was discovered that in some cases an appreciable fraction of the cross section came from excited states of the core [20, 21].

The technique of one-nucleon knockout has been used to measure single-particle configurations over a range of nuclei since its development as a spectroscopic tool [22–27]. More deeply-bound states [22, 27] and particle-unbound states [28] have also been probed using one-nucleon knockout.

In one-nucleon knockout, single-particle spectroscopy of the nuclei of interest is

performed by extracting the following quantities: partial and differential cross sections to ground and excited states of the core fragments; spectroscopic factors for removal of the valence nucleon from a specific state of the core; and the angular momentum of the removed nucleon in the initial state of the nucleus. The measured cross sections are used to calculate the one-nucleon removal spectroscopic factors via an extension of the eikonal model [21]. The clarification of the occupancies of single-particle states in the initial nucleus is made possible by measurements of such spectroscopic factors. The angular momentum of the removed nucleon is obtained from the recoil of the heavy residue, in analogy to the angular distributions used in low-energy transfer reactions. The shape of the measured parallel momentum distribution of the fragments is used to assign angular momenta. The parallel momentum distribution of the fragments, defined as the projection of the fragment's momentum on the beam direction, is used to measure the fragment momentum as it has less dependence on the reaction mechanism than the components of momentum perpendicular to the beam axis [29]. As the heavy fragments have small angular deviations from the beam direction, the parallel momentum contains most of the incident momentum.

The classic tools used to extract spectroscopic factors have been electron scattering $(e, e'p)$ reactions and low-energy transfer reactions [30,31]. Transfer reactions have also been used to assign angular momenta to valence nucleons. For the study of radioactive nuclei, the $(e, e'p)$ reactions are not viable as there is not yet an experimental facility to perform electron scattering on radioactive ions. In addition, electron scattering only probes the spectroscopic factors of protons, while the one-nucleon knockout technique can be used to measure the spectroscopic factors of neutrons as well. Spectroscopic factors are deduced in transfer reactions from the magnitudes of observed cross sections. Models such as the distorted-wave Born approximation (DWBA) with optical model potentials must be used to interpret the measured angular distributions to make angular momentum assignments [32]. Experimental results calculated using these methods are then quite dependent on the input parameters for the optical po-

tentials used in the DWBA calculations. Analyses based on the sudden approximation and the eikonal model, such as those used for the one-nucleon knockout reactions, have fewer free parameters and are thus less model-dependent than DWBA calculations.

An experimental advantage of the one-nucleon knockout technique is the ability to use heavy-ion detectors instead of proton detectors in the experimental apparatus. In addition, the higher beam energies allow for thicker nuclear targets, increasing the number of nucleon removal reactions per second. The beam of fragments after interaction with the nuclear target is forward-focused due to the high mass and velocity of the fragments, allowing for easier detection of the residues. Transfer reactions cannot be performed at energies higher than approximately 20 MeV/nucleon, as the proton angular distributions lose much of the angular momentum dependence and the magnitudes of the cross sections drop with increasing energy [32, 33]. It has been shown that the eikonal description of nucleon-knockout reaction theory is accurate to 20% at energies as low as 20 MeV/nucleon [34]. Such features make the one-nucleon knockout technique attractive for studies of exotic nuclear species such as the ^{19}C isotopes, on which one-neutron knockout was successfully performed with an intensity of less than one ^{19}C ion per second [26].

In the experiment discussed in the following, one-neutron knockout was performed on the ^{57}Ni nucleus. Information about the ground-state structure of ^{57}Ni as well as the excited state structure of the heavy residue ^{56}Ni was obtained. This experiment represents the first attempt to extend the one-nucleon knockout technique beyond $A = 40$ and to an $l = 3$ angular momentum distribution. The theory of one-nucleon knockout analysis will be discussed in Section 2.1.2. Previous theoretical and experimental results for ^{57}Ni and ^{56}Ni will be discussed in Section 2.2. The experimental setup will be outlined in Section 2.3 and the results and discussion of the data analysis will follow in Sections 2.4 and 2.5, respectively.

2.1.2 Theory

Theory of the single-particle cross sections

The basis of the theoretical analysis of the cross sections uses the spectator core eikonal model to relate the measured cross sections for one-nucleon removal to theoretical spectroscopic information using a fixed set of input parameters [21, 29]. The eikonal model, an impact-parameter based model originally used for nucleus-nucleus scattering at high energies, has been shown to give a good description of the observed cross sections for knockout reactions of halo nuclei (^{11}Li, ^{11}Be, and ^{8}B) on light targets [35–37]. The same analysis technique has also proved useful for more deeply-bound states [22, 27].

In the analysis of data from one-nucleon knockout, the single-particle structure of the projectile ground state is of interest. Information about this single-particle structure can be provided by the spectroscopic factor for the removal of a nucleon from the projectile's ground state and the angular momentum of the nucleon before its removal. It is assumed that before the interaction, the $(A + 1)$-body projectile has A of its nucleons in the core state ϕ^c which is accessible by the removal of the least-bound (valence) nucleon. The quantity C^2S is the spectroscopic factor for the removal of a nucleon with given single-particle quantum numbers nlj. This factor expresses the parentage of this specific nucleon-core configuration in the initial state with respect to the specific core state c of the remaining nucleons. The measured cross section to a specific core state is related to the quantity C^2S, where the sum must be taken over all non-vanishing nucleon-core configurations. The cross section for populating a given core state c is:

$$\sigma(c) = \sum_j \left(\frac{A}{A-1}\right)^N C^2S(c, nlj)\, \sigma_{\mathrm{sp}}(S_n, nlj). \tag{2.1}$$

In Equation 2.1, the contribution from nuclear structure enters in the spectroscopic

factor, while the single-particle cross section $\sigma_{\rm sp}$ comes from reaction theory. Once the cross section $\sigma(c)$ has been measured, the spectroscopic factor is determined and can be compared to theory. The factor $(A/(A-1))^N$ is the center-of-mass correction to the spectroscopic factor, where A is the mass number of the initial nucleus and N is the main harmonic oscillator quantum number associated with each major shell [38, 39]. For the present experiment, one-nucleon removal from ^{57}Ni will occur in the framework of the fp shell, resulting in a center-of-mass correction of 1.054 for $N = 3$.

Theoretical excited levels of ^{56}Ni and associated spectroscopic factors were calculated in the many-body shell model [40–42] with the FPD6 effective interaction [43]. For ^{57}Ni, the $\nu(f_{7/2})$ and $\pi(f_{7/2})$ closed shells plus one neutron in the $p_{3/2}$ shell were assumed. For ^{56}Ni, calculations were performed with the $\nu(f_{7/2})$ and $\pi(f_{7/2})$ closed shells for the ground state, and for the excited state $\pi(f_{7/2})^8$ and $\nu(f_{7/2})^7$ with the $p_{3/2}$, $f_{5/2}$, and $p_{1/2}$ neutron shells active.

The single-particle cross sections, which are highly dependent on the separation energy of the valence nucleon (S_n) and the orbital angular momentum (l) of the valence nucleon, are calculated in the eikonal model and contain contributions from both stripping and diffraction processes [21]. Stripping occurs when the valence nucleon is absorbed and subsequently excites the target. In the diffractive process, the target remains in its ground state and the valence nucleon continues on with essentially beam velocity. As the removed nucleon is not detected in the one-nucleon knockout experimental method, the incoherent sum of both processes must be included. For weakly bound states such as halo nuclei, the two processes are comparable in strength. For knockout from more bound states such as core nucleons or tightly bound valence nuclei, the stripping process dominates. The latter is the case for the study presented here, where the valence neutron in ^{57}Ni is bound by more than 10 MeV and the core is the doubly-magic nucleus ^{56}Ni. The single-particle cross sections are calculated as [21]:

$$\sigma_{\rm sp} = \sigma_{\rm sp}({\rm str}) + \sigma_{\rm sp}({\rm diff}), \tag{2.2}$$

where the cross section for stripping is

$$\sigma_{\rm sp}({\rm str}) = \frac{1}{2I+1}\int d\mathbf{b}\sum_{M}\langle\phi^{c}_{IM}|(1-|S_{nt}|^2)|S_{ct}|^2|\phi^{c}_{IM}\rangle \tag{2.3}$$

and that for diffraction is

$$\sigma_{\rm sp}({\rm diff}) = \frac{1}{2I+1}\int d\mathbf{b}\left[\sum_{M}\langle\phi^{c}_{IM}\|(1-S_{ct}S_{nt})|^2|\phi^{c}_{IM}\rangle - \sum_{MM'}|\langle\phi^{c}_{IM}|(1-S_{ct}S_{nt})|\phi^{c}_{IM}\rangle|^2\right]. \tag{2.4}$$

The integral is over the projectile center-of-mass impact parameter $\mathbf{b}$, defined as the distance between the centers of the projectile and target nuclei. The impact parameter is classical, its use justified by the high projectile energies involved in nucleon knockout reactions. The projectile ground state configuration $|\phi^{c}_{IM}\rangle$ is described as a valence nucleon with single particle quantum numbers nlj with an associated spectroscopic factor for the core state c. Detection of the de-excitation gamma rays allows identification of the specific core states. I is the intrinsic spin and M is the spin projection of the projectile ground state. The angular momenta follow the usual selection rules $\mathbf{I} = \mathbf{c} + \mathbf{j}$, where $\mathbf{j}$ is the angular momentum of the nucleon, $\mathbf{c}$ is that of the core, and $\mathbf{I}$ is that of the projectile ground state. The $|\phi^{c}_{IM}\rangle$ are calculated in a Woods-Saxon potential well model with radius and diffuseness parameters 1.25 fm and 0.6 fm, respectively. The Woods-Saxon potential well depth is set to reproduce the separation energy of the nucleon in the initial state, $S_n = 10.247$ MeV for ^{57}Ni [44].

S_{ct} and S_{nt} are the profile functions, or S-matrices, for the core-target and the removed nucleon-target systems, calculated in the optical limit of Glauber theory [45]:

$$S(\mathbf{b}) = \exp\left[\frac{-i}{\hbar v}\int dz V(\mathbf{b}+z\hat{z})\right], \tag{2.5}$$

where v is the beam velocity, V is the interaction potential, and the S-matrices

are functions of their own impact parameter b [37, 46]. The quantity $|S(\mathbf{b})|^2$ is the transmission probability at the impact parameter **b**. The input parameters in the calculation of the profile functions are an effective nucleon-nucleon interaction and core and target nuclear matter distributions.

For the current analysis, the ^{56}Ni core fragment's matter distribution was described by a two-parameter Fermi distribution

$$\rho_{\mathrm{2pF}}(r) = \frac{\rho_o}{1 + \exp((r-c)/z)} \tag{2.6}$$

where the quantity c is the distance from the center of the matter distribution, with a density of ρ_o, to the point where the density drops to one-half ρ_o. The diffuseness of the matter distribution is described by the quantity z. Previous analyses assumed a Gaussian distribution for the core fragment, an assumption only valid for light nuclei. The ^{56}Ni core *rms* radius ($< r^2 >^{1/2}$) was assumed to be 3.62 fm, from the ^{56}Fe matter radius. The *rms* radius of the lighter ^{9}Be target was taken to be 2.36 fm, with a Gaussian matter distribution assumed. The effective nucleon-nucleon interaction was assumed to be Gaussian, with a finite interaction range parameter 0.5 fm [21]. Also assumed are free neutron-neutron and neutron-proton cross sections, and real to imaginary ratios of the forward scattering amplitude at 100 MeV [47].

Theory of the parallel momentum distributions

The parallel momentum distributions were calculated with a slightly different set of theoretical assumptions than those made for the calculations of the cross sections [29]. The classical impact parameter **b** is again assumed, justified by the high projectile energies. Most notably, the black disk model is assumed. Collisions occurring at impact parameters less than a specified $b_{min} = r_{core} + r_{target}$ are assumed to result in fragmentation of the core fragment, and are not included in the analysis. In addition, the wave function of the valence nucleon is assumed to exist unchanged throughout

all space, except in a cylinder with a radius equal to that of the core, where it is set to zero. The profile functions S_{ct} and S_{nt} are assumed to be unity outside of a cutoff impact parameter and zero inside. The core-target profile functions S_{ct} are highly absorptive, in general, which upholds the use of the black-disk approximation for nuclear collisions at the energies of interest in these studies, 50–100 MeV/nucleon. By requiring that the core survive the interaction with the target, the core-target interaction must be highly peripheral. Thus the removed nucleon's wave function is probed at and beyond the surface of the projectile. The sudden approximation is also assumed in these calculations, where the core acts as a spectator in the reaction, and at the moment of collision the state of the system is fixed. The core can react at most elastically with the target. The black disk model uses effective interaction radii chosen to reproduce the reaction cross sections of the free constituents. In this analysis, *rms* radii of 4.286 fm and 4.059 fm were obtained for the $p_{3/2}$ and $f_{7/2}$ levels of ^{57}Ni, respectively. A core-target radius of 1.217 fm, neutron-target radius of 2.983 fm, and reaction cross section for a free neutron of 279.6 mb were assumed. A minimum impact parameter of $b_{min} = 7.188$ fm was chosen. The measured neutron separation energy (S_n) of 10.247 MeV for the $p_{3/2}$ level was assumed [44]. A S_n of 14 MeV for the $f_{7/2}$ level was estimated from the center of the $p_{3/2}f_{7/2}$ multiplet [48]. Comparison between the shapes of the theoretical momentum distributions and measured parallel momentum distributions can provide angular momentum assignments because the distributions are relatively insensitive to the details of the reaction but are sensitive to the binding energy and orbital angular momentum of the removed nucleon. The theoretical momentum distributions were transformed into the laboratory system, which broadens them by the relativistic γ factor.

2.2 Previous experimental results

As discussed in Section 1.3, it has been shown that the $N = Z = 28$ doubly-magic shell closure nucleus ^{56}Ni may not have the same characteristics as stable doubly-magic nuclei. It thus becomes of interest to study the single-particle structure of the nearest neighbors of ^{56}Ni with one proton or neutron on top of the doubly-magic core. According to the shell model, the ground state of ^{57}Ni should be well represented as one neutron in the $1f_{7/2}$ state coupled to the ground state of the ^{56}Ni core (see Figure 2.1). The naive picture of one-neutron knockout from the ground state of ^{57}Ni would remove the valence nucleon from the $2p_{3/2}$ level, with the ^{56}Ni core remaining in its 0^+ ground state. At the intermediate beam energies used in this study, there is also the possibility of one-neutron knockout to excited states of ^{56}Ni, which in the simple shell-model picture would occur as a result of removal of one of the $1f_{7/2}$-shell neutrons. The spectroscopic factors for removal to the ground and excited states of ^{56}Ni have been calculated in the many-body shell model as discussed in Section 2.1.2, and will be compared to measured spectroscopic factors to look for evidence of mixing of the ^{56}Ni first excited state ($J^\pi = 2^+$) in the ^{57}Ni ground state.

The level scheme of ^{57}Ni is well known as a result of various experiments dating from 1965 [44]. The ground state of ^{57}Ni has a spin and parity of $J^\pi = 3/2^-$, with the first two excited states at 768 keV ($J^\pi = 5/2^-$) and 1113 keV ($J^\pi = 1/2^-$). The first excited state represents promotion of the valence $2p_{3/2}$ neutron to the $1f_{5/2}$ level, while the second excited state $2p_{3/2}$ to $2p_{1/2}$. It was suggested in one of the early experiments on ^{57}Ni [49] that the first two excited states and a state at 2577 keV ($J^\pi = 7/2^-$) may not be pure single-particle states, but may include contributions from ^{56}Ni excited states. The authors acknowledged that the degree of observed impurity in the ^{57}Ni wave functions may be slight as the measurements were made via gamma decay. Later measurements of large excitation strengths to the first excited state of ^{56}Ni [10, 11] created more interest in the single-particle character of the

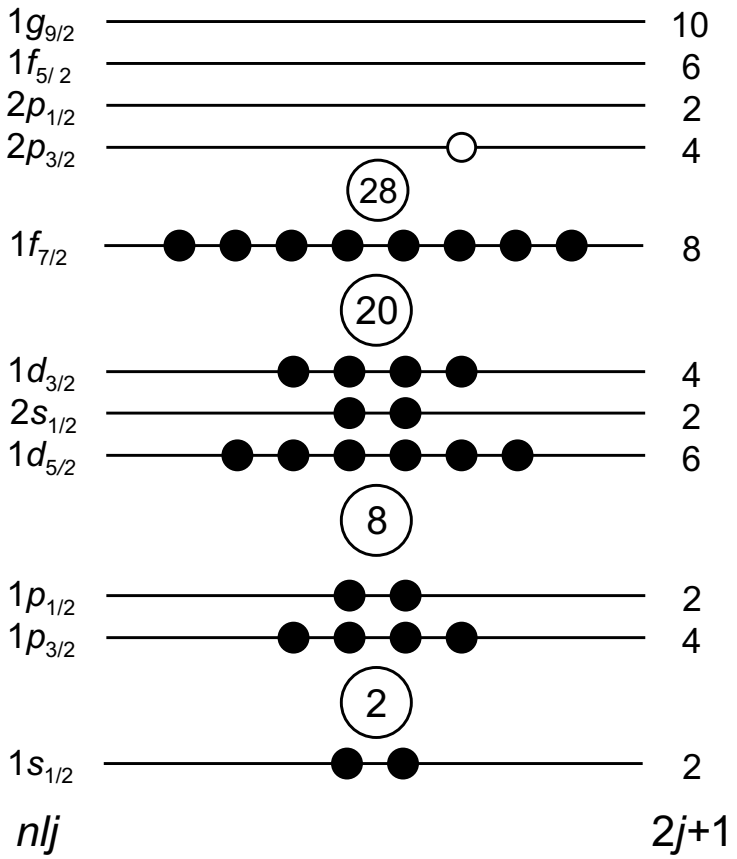

Figure 2.1: Schematic diagram of the location of ^{57}Ni nucleons in the spherical shell model. The single-particle energy spectrum is shown up to the $1g_{9/2}$ level. The levels are those calculated from a three-dimensional harmonic oscillator potential with spin-orbit interactions included. The angular momentum l is represented by the labels s, p, d, f, g, corresponding to $l = 0, 1, 2, 3, 4$. The number of occurrences of a particular l value is labeled by n, in ascending order according to energy. The projection of the total spin $\mathbf{j} = \mathbf{l}+\mathbf{s}$ of the shell is j. The circled numbers indicate the "magic numbers". The black filled circles indicate the occupancies of both protons and neutrons for the ground state of ^{56}Ni, while the open circle indicates the valence neutron in ^{57}Ni.

ground and lowest excited states of ^{57}Ni. The spectroscopic factors for the first three states of ^{57}Ni were recently measured in a low-energy transfer reaction performed by Rehm *et al.* [50]. In contrast with the indications of collectivity from the ^{56}Ni excitation strength measurements, Rehm and collaborators concluded that the first three states of ^{57}Ni are well-described as single-particle states. Spectroscopic factors of $S = 0.91(2p_{3/2})$ for the ground state, $S = 0.91(1f_{5/2})$ for the first excited state, and $S = 0.90(2p_{1/2})$ for the second excited state were deduced from a (d, p) transfer reaction at an energy of approximately 4.5 MeV/nucleon. DWBA calculations were used

in the transfer reaction measurement to determine the spectroscopic factors from the measured cross sections and proton angular distributions. The error on the spectroscopic factor measurements was estimated to be about 50%, in part due to a lack of good optical potential parameters for ^{56,57}Ni used as input to the DWBA calculation.

2.3 Experimental setup

In the traditional method for measurements of properties of stable nuclei, a target composed of the nuclei of interest was bombarded with a beam of another stable isotope. Different properties of the target nucleus were then measured depending on the nuclear process to be studied such as nuclear beta decay, Coulomb excitation, or proton scattering. This method, however, does not allow for the study of radioactive nuclei. In order to study such exotic nuclei, the method of inverse kinematics was applied. In this method the incident beam of nuclei, now radioactive, becomes the object of measurement. A stable target is still used, but now the target is the means of inducing the nuclear process of interest.

2.3.1 Secondary beam production

In order to study radioactive nuclei, they must be produced, transported to the experimental area, and measured before decay occurs. One method for producing radioactive beams is projectile fragmentation. This method is used at the National Superconducting Cyclotron Laboratory (NSCL) to produce nuclei ranging from hydrogen to uranium isotopes. A beam of stable nuclei, also called the "primary" beam, is produced in either a room-temperature or superconducting electron-cyclotron resonance (ECR) source and then accelerated in a superconducting cyclotron. Once the primary beam has reached the desired energy, it is extracted from the cyclotron and is incident upon a thick production target, usually ^{9}Be. In the present one-neutron knockout experiment, acceleration of a beam of stable ^{58}Ni to an energy of 105 MeV/nucleon

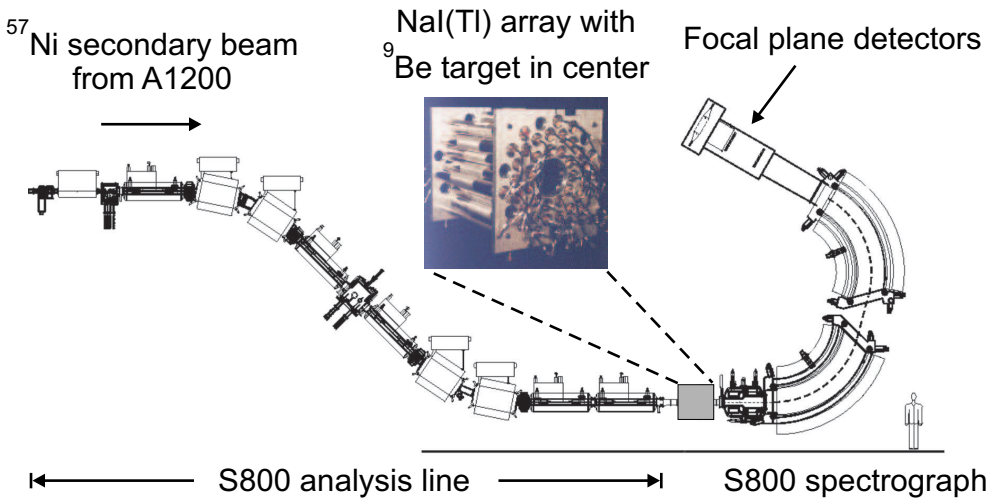

Figure 2.2: Schematic of the experimental setup for one-neutron knockout.

and an intensity of 2 pnA was carried out in the K1200 cyclotron. The ^{58}Ni beam was incident on a 249 mg/cm^2 ^{9}Be production target. While most of the nuclei in the primary beam pass through the fragmentation target unreacted, a number of the nuclei react with the target and produce fragments ranging from hydrogen to ions with masses greater than the primary beam. It is then necessary to select the nuclei of interest to be transported to the experimental area. The selection of the "secondary" beam of rare isotopes takes place in a fragment separator.

The A1200 fragment separator [51] was used in this experiment to select a secondary beam of ^{57}Ni with an energy of 73 MeV/nucleon, an intensity of approximately 30,000 particles per second and a momentum spread of 0.5%. The fragment separator is a series of dipole magnets used to separate the beam nuclei by mass and charge, quadrupole magnets for steering, a wedge-shaped degrader to purify the secondary beam, and slits to select the beam of interest. The secondary beam produced as a result of the fragmentation and selection process usually has a velocity of $0.3c$ to $0.5c$ and, especially for beams of heavier nuclei, is composed of a mix of nuclei in addition to the fragment of interest. These two facts are important experimental considerations in the design of detectors used in the experimental apparatus. The high beam velocity requires Doppler reconstruction for detected gamma rays, and the mixed beam

requires separation of the nuclei of interest from the contaminants.

In the present experiment, the secondary beam of ^{57}Ni was purified using the A1200 fragment separator and transported to the experimental area. A schematic of the experimental setup can be seen in Figure 2.2. The secondary beam was transported through the analysis line of the S800 spectrograph [52], which is similar to the A1200 fragment separator. A 56.1 mg/cm^2 ^{9}Be target was located at the center of an array of 38 NaI(Tl) detectors [53] at the entrance to the S800 spectrograph. The NaI(Tl) array detected gamma rays emitted from the de-excitation of ^{56}Ni fragments created in an excited state as a result of one-nucleon knockout from ^{57}Ni in the ^{9}Be target. The tertiary beam of fragments from the ^{57}Ni ions' interaction with the knockout target were subsequently transported through the two dipoles of the S800 spectrograph to the series of detectors located at the focal plane [54], where the ^{56}Ni nuclei were identified. The S800 spectrograph and its focal plane detectors will be described in Section 2.3.2, while the NaI(Tl) array will be discussed in Section 2.3.3.

2.3.2 S800 spectrograph

The S800 magnetic spectrograph [52] provides a high-resolution tool for identifying the ^{56}Ni fragments of interest and reconstructing the momentum distributions associated with the fragments. Impurities in the secondary beam are present after the beam emerges from the A1200 fragment separator. When the ^{57}Ni secondary beam reaches the secondary knockout target at the entrance to the S800 spectrograph, most of the ^{57}Ni nuclei pass through the target unreacted. Of the fraction of incident secondary beam particles that react with the target, another small fraction undergo the one-neutron knockout reaction of interest. Many other nuclear reactions produce a large range of nuclei. The tertiary beam then contains another large range of nuclei similar to that produced by the primary beam's interaction with the fragmentation target. It is necessary to detect the ^{56}Ni fragments from one-neutron knockout and separate them from the other nuclear species. This separation becomes more diffi-

cult as the mass of the one-neutron knockout fragments increases and the percentage difference in the masses between neighboring nuclei decreases. The ^{56}Ni fragments were identified in the focal plane [54] of the large acceptance S800 magnetic spectrograph, operated in dispersion-matched, energy-loss mode. In this mode, the spread in incident momentum of the secondary beam from the A1200 fragment separator is compensated by dispersing the beam on the ^{9}Be target and then using the spectrograph to focus the fragments at the focal plane. As the S800 has a large dispersion, the spread in momentum of the incident secondary beam must be limited to 0.5%. Characteristics of the spectrograph include angular acceptances of $\pm 5^{\circ}$ in the horizontal, non-dispersive direction, $\pm 3.5^{\circ}$ in the vertical, dispersive direction, a solid angle acceptance of 20 msr, a momentum acceptance of $\pm 2.5\%$, and a dispersion of 9.6 cm per percent. Details of the specific focal plane detectors follow in the next three sections.

Cathode readout drift counters

Position and angle information for the fragments exiting the spectrograph was provided by two position-sensitive cathode readout drift counters (CRDCs). The two CRDCs, separated by one meter, were filled to a pressure of 140 Torr with a mixture of 80% CF_4 and 20% C_4H_{10} gas. The CRDCs have an active area of 30 cm^2 in the vertical (y) direction, 59 cm^2 in the horizontal (x, dispersive) direction, and a depth of 1.5 cm. As the tertiary beam fragments pass through a CRDC, the charged fragments induce ionization of the gas, and a constant electric field causes the resulting electrons to drift to the anode wire. The drift time of the electrons provides the vertical position of the ion. A series of 224 cathode pads, separated by 2.54 mm, are located in front of and behind the anode wire. The collection of the electrons on the anode wire induces an image charge on the pads. Each of the 224 pads is read by the electronics, and the centroid of a Gaussian fit to the charge distribution for the pads is the horizontal position of the ion. A detector resolution better than 0.51 mm

FWHM was measured with a test beam of ^{22}Ne at 80 MeV/nucleon [54]. Calibration of the CRDCs was performed by placing a mask with holes and slits in front of each detector, and dispersing the beam to illuminate the mask pattern. The position of the holes and slits provided the calibration in y, while the known spacing between the cathode pads was used for the x calibration.

As the fragments travel through the spectrograph, the magnetic elements change the coordinates of the nuclei due to the action of the magnetic fields on the charged ions. The quantities of interest for the experimentalist are the energy and position of the ions as they leave the secondary target, just before they enter the spectrograph. A transfer matrix S is used to relate the final coordinates, measured by the CRDCs at the focal plane, to the initial coordinates just after the target

$$\begin{bmatrix} x_f \\ \theta_f \\ y_f \\ \phi_f \end{bmatrix} = S \begin{bmatrix} \theta_i \\ y_i \\ \phi_i \\ \delta_i \end{bmatrix}. \tag{2.7}$$

Here x_f,θ_f, and y_f,ϕ_f are the position and angle of the beam particle at the CRDC in the horizontal and vertical directions, respectively. The initial coordinates ϕ_i, θ_i, and y_i are the angles and vertical position of the beam particle at the target. The initial spot size of the beam in the dispersive direction x is assumed to be negligibly small. The initial fractional kinetic energy of the beam particle relative to a central, reference trajectory is $\delta_i = (E - E_o)/E_o$. Each magnetic element in the spectrograph has its own transfer matrix, and the total transformation is their product. The inversion of the matrix in S is complicated, and results in a matrix R which is not a true inverse of S, but allows for energy and angles of the ions as they enter the spectrograph to

be calculated as

$$\begin{bmatrix} \theta_i \\ y_i \\ \phi_i \\ \delta_i \end{bmatrix} = R \begin{bmatrix} x_f \\ \theta_f \\ y_f \\ \phi_f \end{bmatrix}. \tag{2.8}$$

This inversion procedure is carried out by the COSY INFINITY code which includes first order optics and all optical aberrations [55].

Ionization chamber

The next in the series of focal plane detectors is the ionization chamber, used to measure the energy loss of the ions. The ionization chamber is a standard Frisch gridded ion chamber, segmented into 16 one-inch anodes which are perpendicular to the ions' trajectory through the chamber. The 41 cm deep chamber is filled with 300 Torr of P10 gas, a mixture of 90% argon and 10% methane gases.

Scintillation detectors

The last set of detectors is a series of three plastic scintillators which are 5, 10, and 20 cm thick. The scintillators measure energy loss and total energy of the ions, and also provide timing information. The first scintillator detector is used as the exit window of the ionization chamber in order to reduce energy straggling that would be associated with an exit window. This detector also provides the timing information which, when combined with timing from another plastic scintillator detector located at the exit of the A1200 fragment separator, provides time of flight for the fragments. The scintillator detectors are read out at each end by a photomultiplier tube. A light guide is mounted on each end of the scintillator to enhance light collection in the photomultiplier tubes. The amount of light collected is a function of the atomic number, atomic mass, and total energy of the ions. The light collection time from the scintillator is on the order of nanoseconds, and a timing response of 160 ps FWHM has

been measured with a beam of 60 MeV/nucleon ^{16}O for the 10 cm thick detector [54].

2.3.3 NaI(Tl) array

Gamma rays produced in experiments with intermediate-energy beams ($\beta \approx 0.3$–0.5) are considerably Doppler shifted. Such velocities are typical of the beams produced via projectile fragmentation at the NSCL. While the energy of the photon in the laboratory frame (E_γ^{lab}) is measured, the quantity of interest is the energy of the photon in the rest frame of the projectile nucleus (E_γ^{pro}). The energy of the emitted photon in the rest frame of the projectile can be reconstructed from the energy of the photon observed if the laboratory angle of photon emission (θ^{lab}) and the velocity of the projectile in the laboratory frame (v^{lab}) are known:

$$E_\gamma^{pro} = \frac{E_\gamma^{lab}(1 - \beta\cos\theta^{lab})}{\sqrt{1-\beta^2}}, \quad \beta = \frac{v^{lab}}{c}. \tag{2.9}$$

Determination of the angle of the emitted photon with respect to the beam axis is also necessary to minimize the error on the extracted projectile-frame energy. All photon detectors have a finite opening angle which is combined with the uncertainty in the beam energy and the intrinsic resolution of the detector material in the equation for energy resolution ΔE_γ

$$\left(\frac{\Delta E_\gamma}{E_\gamma}\right)^2 = \left(\frac{\beta\sin\theta}{1-\beta\cos\theta}\right)^2 (\Delta\theta)^2 + \left(\frac{-\beta+\cos\theta}{(1-\beta^2)(1-\beta\cos\theta)}\right)^2 (\Delta\beta)^2 + \left(\frac{\Delta E_{\rm int}}{E_\gamma}\right)^2. \tag{2.10}$$

The uncertainty of the beam energy ($\Delta\beta$) comes from the energy loss of the beam particle due to its interaction with the target. The intrinsic energy resolution ($\Delta E_{\rm int}$) of the NaI(Tl) detectors is approximately 8% at 662 keV. The uncertainty in the photon emission angle ($\Delta\theta$) due to the opening angle of the gamma-ray detector can be minimized by using position-sensitive gamma-ray detectors.

In this experiment, an array of 38 NaI(Tl) inorganic scintillator detectors [53] was

used to detect gamma rays from the de-excitation of ^{56}Ni fragments. The array of detectors was placed parallel to the beam direction and arranged in three concentric rings around a 15 cm diameter beam pipe. Each scintillator is 17.1 cm long and 5.0 cm in diameter, with a photomultiplier tube coupled to each end. The parallel orientation of the scintillators coupled with the use of two phototubes for each scintillator allowed for a determination of the energy and position of each photon which interacted with the array. The inner ring contained 11 detectors at a distance of 10.8 cm from the center, the middle ring 17 detectors at a distance of 16.9 cm, and the outer ring 10 detectors at 21.8 cm. Only the inner ring of detectors was analyzed in this experiment, as the inclusion of data from the outer two rings resulted in only a marginal increase in the peak-to-background ratio of the measured gamma rays. The secondary target of ^{9}Be was placed in the beam pipe at the center of the array perpendicular to the beam axis. ^{9}Be is especially useful as a secondary target as it has no bound excited states which could contaminate the measured gamma-ray spectrum.

When an emitted photon deposits energy in a NaI(Tl) scintillator, the number of scintillation photons produced is proportional to the energy deposited. An exponential attenuation of the light is assumed as the photons travel through the scintillator, which results in the following equations for the measured light output ($E_{1,2}$) from the photomultiplier tubes 1 and 2:

$$E_1 \propto Ee^{-\mu((L/2)+x)} \quad \text{and} \quad E_2 \propto Ee^{-\mu((L/2)-x)}. \tag{2.11}$$

E is the deposited energy, μ is a parameter that describes the attenuation of the photons in the scintillator material, L is the length of the crystal, and the proportionality factor (not shown) includes the gain of the photomultiplier tubes and amplifiers. The energy E and position x of the incident photon can then be calculated from

$$E \propto \sqrt{E_1 E_2} \quad \text{and} \quad x \propto log\left(\frac{E_1}{E_2}\right). \tag{2.12}$$

Position and energy calibrations

The assumption of exponential attenuation used to reach Equation 2.11 is only valid when the photon deposits its energy near the center of the crystal. In order to correct for nonlinearities near the edges of the scintillators, a position calibration of each NaI(Tl) detector is performed for every experiment. A detailed discussion of the position calibration procedure can be found in [56]. A collimated 0.5 MBq ^{60}Co gamma-ray source was mounted in a cylindrical HeviMet (copper/tungsten alloy) collimator, constructed to fit inside the beam pipe. Two cylinders 7.62 cm long and 14.0 cm in diameter are joined together, leaving a 4.6 mm gap in between for the ^{60}Co source. The gamma rays from the de-excitation of ^{60}Co are thus emitted 360° in the plane of the 4.6 mm gap, allowing for simultaneous calibration of all 38 detectors. A long metal rod with an attached measuring tape was used to move the collimator in one-inch steps from one end of the array to the other. At each position, data were collected for five minutes. For each detector at each position of the source, the reconstructed position of the 1332 keV gamma ray from the decay of ^{60}Co was histogrammed and fit. The centroid of the fit was the reconstructed position. The plot of reconstructed position versus actual position was then fit with a third order polynomial, in order to describe the nonlinear behavior close to the edges of the detector. The positions at the edges of each detector which exhibited a turnover in the curve were eliminated in the subsequent gamma-ray analysis. The calibrated detectors have a position resolution of 2 cm, resulting in an angular resolution of better than 10° for the inner 11 detectors.

After the completion of the position calibration, a position-dependent energy calibration was performed. The raw reconstructed energy is not position-independent in the NaI(Tl) detectors, requiring that each detector be divided into 10 position slices using software cuts. For each slice in each detector, a plot of reconstructed energy versus actual energy was created and fit with a first-order polynomial. The 898 keV and 1836 keV gamma rays from a standard ^{88}Y source and the 583 keV and 2614 keV

gamma rays from a ^{228}Th source were used in this calibration. Two-dimensional plots of reconstructed energy versus reconstructed position were examined, and gamma-rays interacting in slices in position with poor energy calibrations were discarded in the data analysis.

Simulations

Although the position information provided by the NaI(Tl) array allows for Doppler correction of the emitted photon energy, the transformation from the laboratory system to the rest frame of the projectile nucleus does not result in the spectrum that would be observed from a source at rest. While the photopeak is correctly transformed to the particle's rest frame, Compton scattering, pair production, and backscattering of photons from the surrounding materials into the NaI(Tl) scintillator all produce features in the gamma-ray spectrum that are smeared after the Doppler reconstruction. A further complication is introduced by the energy-dependent detection efficiency of the NaI(Tl) array. For each gamma-ray energy observed in the experimental spectrum, a Monte Carlo simulation was performed to produce two million Lorentz-boosted gamma-ray events at the correct energy, isotropically emitted in the rest frame of the projectile. These events were then used by the GEANT code [57] to simulate the energy deposited in the detectors, taking into account losses due to interactions with the surrounding equipment, energy resolution, position resolution, and efficiency of the detectors. Experimental efficiencies measured with standard calibration sources agreed within 7.5% to simulations. The resulting histograms were Doppler-reconstructed ($\beta = 0.36$) and fit with analytical curves to eliminate statistical fluctuations. These curves were then fit to the experimental gamma-ray spectrum.

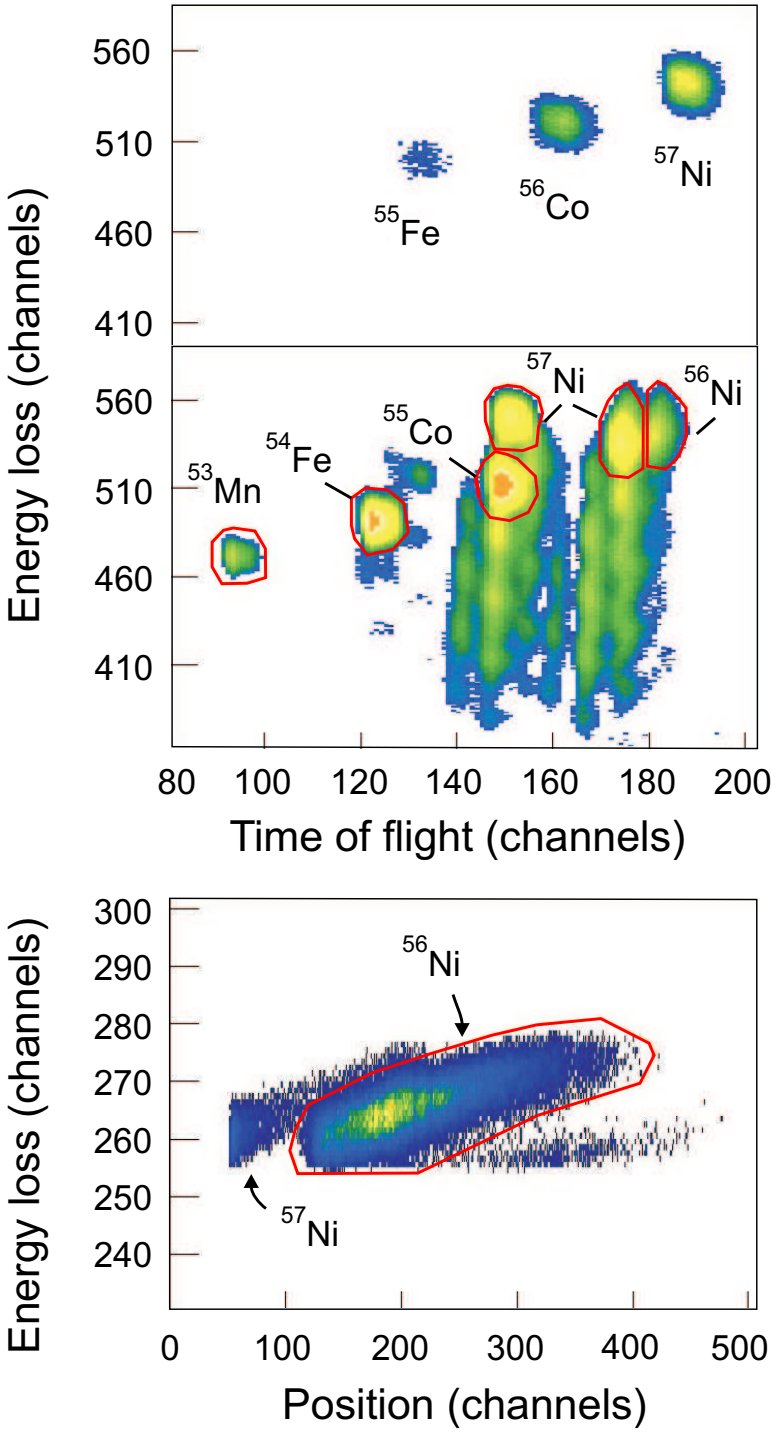

Figure 2.3: Particle identification spectra for ^{56}Ni fragments. The top panel shows the spectrum with the spectrograph magnetic fields set to the ^{57}Ni beam momentum. The middle panel shows the spectrum after the settings were scaled by $(A-1)/A$. A further cut on ^{56}Ni was required to cleanly separate the fragments of interest from the incident ^{57}Ni beam, shown in the bottom panel.

2.4 Experimental results

2.4.1 Particle identification

Due to the presence of contaminants from the reactions of the primary beam with the fragmentation target and the secondary beam with the knockout target (see Section 2.3.2), the first step in data analysis was the identification of the ^{56}Ni fragments at the S800 spectrograph focal plane. Identification of the ^{56}Ni fragments created from the one-neutron knockout of ^{57}Ni was performed with the S800 spectrograph focal plane detectors and a plastic scintillator detector (BLT) located at the exit of the A1200 fragment separator. The distance between the BLT and the first scintillator of the S800 focal plane was approximately 70 m. Measurement of the time between a beam particle's interaction in the BLT and the first S800 scintillator was the "time of flight" of the particle. The time of flight for each beam particle was used in conjunction with the particle's energy loss in the S800 ion chamber to make a first particle identification. To facilitate identification of the different particles at the S800 focal plane, the spectrograph magnetic fields were first set to the momentum of the ^{57}Ni secondary beam. This allowed for a clear identification of the ^{57}Ni beam and main contaminants ^{56}Co and ^{55}Fe. The particles were identified in an energy loss versus time of flight spectrum, shown in the top panel of Figure 2.3. Data was collected at this spectrograph setting for five minutes, both for particle identification and to determine the rate of incident ^{57}Ni particles for subsequent cross section calculations.

In order to identify the fragments of the tertiary beam, the magnetic fields of the spectrograph were scaled by $(A-1)/A$ to place the ^{56}Ni fragments at approximately the same energy loss and time of flight as the ^{57}Ni particles in the previous data run. After the change of spectrograph fields, one can identify the ^{56}Ni fragments of interest, slower ^{57}Ni beam particles, and various other fragments from one-nucleon knockout in the middle panel of Figure 2.3. The slight separation between the ^{56}Ni and ^{57}Ni particles shown in the upper right corner of the middle panel in Figure 2.3

was not initially apparent. A correction of the time of flight for the position and angle of the particles at the S800 focal plane was necessary to separate the two particles enough to place a first gate on ^{56}Ni. Because of the heavy masses of the ^{57}Ni and ^{56}Ni particles, it was difficult to separate them using only energy loss and time of flight. The first gate on ^{56}Ni was then applied to a plot of energy loss versus position in the two CRDCs. A second gate on these spectra allowed us to make a clean identification of the ^{56}Ni particles, as shown in the lower panel of Figure 2.3.

2.4.2 Analysis of the gamma-ray spectrum

After the ^{56}Ni residues from one-neutron knockout were unambiguously identified, the coincident gamma-ray spectrum was analyzed. The gates on the ^{56}Ni particles discussed in the previous section were applied to the energy-calibrated and Doppler-corrected gamma-ray spectra for each of the 11 NaI(Tl) detectors in the inner ring. A gamma-ray spectrum created from the sum of the 11 Doppler-corrected spectra from the individual NaI(Tl) detectors was then created. It was possible to analyze the summed spectrum from the 11 inner-ring detectors as angular distribution effects are integrated out due to the large angular coverage of the NaI(Tl) detectors. The simulated gamma-ray spectra were similarly summed and used to fit the experimental spectrum.

The Doppler-reconstructed ($\beta = 0.36$) gamma-ray spectrum in coincidence with ^{56}Ni fragments detected at the spectrograph focal plane is shown in Figure 2.4 as a function of the reconstructed center-of-mass energy. The analytical curves fit to the simulated summed spectra and subsequently scaled to fit the experimental spectrum can be seen as solid grey lines. The dashed line indicates the unavoidable coincident background, described in this experiment by a double exponential curve. A similar background has been seen in previous knockout experiments [23–27] where it has been attributed to neutrons, gamma rays and charged particle interactions with the experimental apparatus and scintillators. Exponential backgrounds with intensities

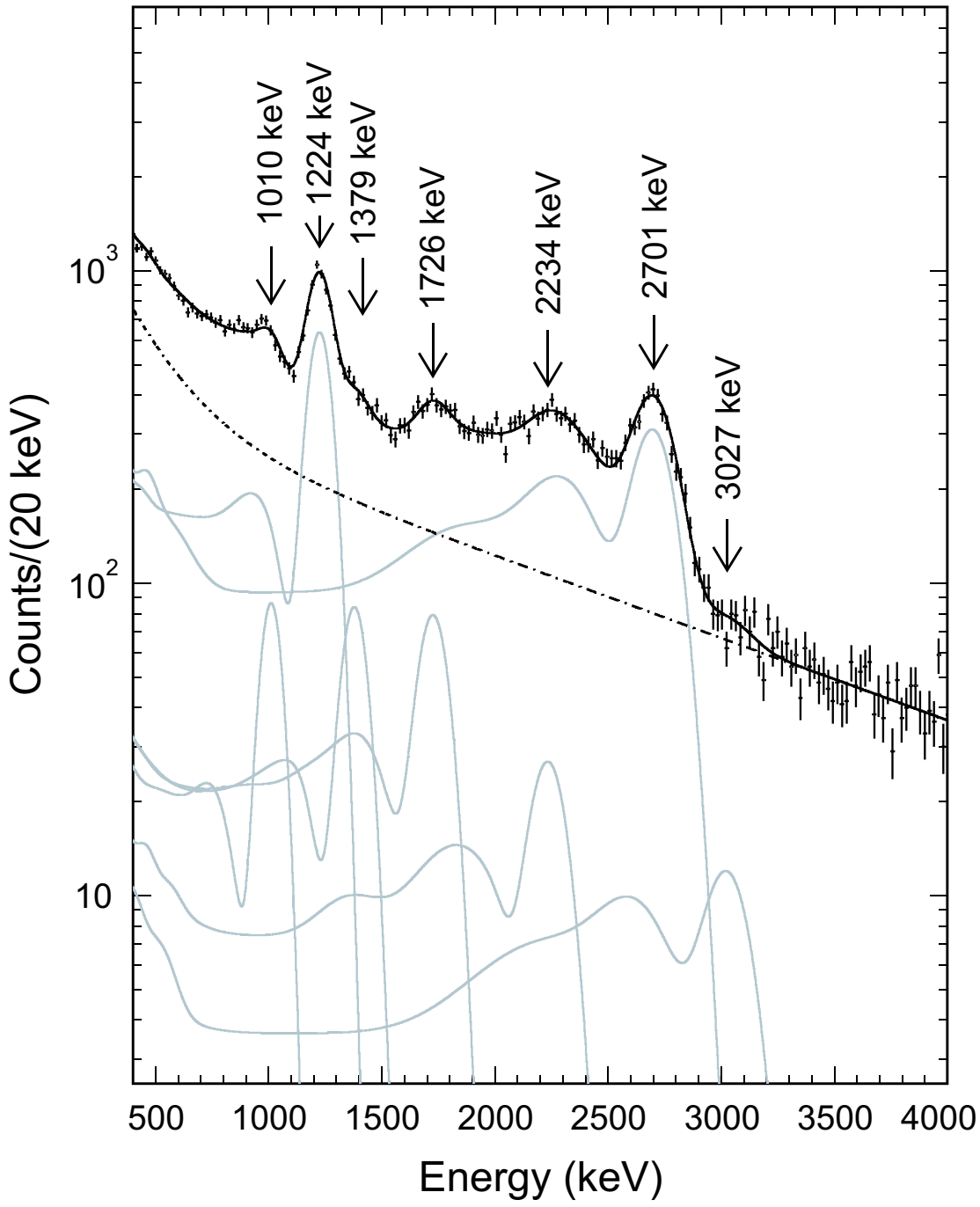

Figure 2.4: Doppler-corrected ($\beta = 0.36$) gamma-ray spectrum in coincidence with ^{56}Ni fragments detected at the spectrograph focal plane. The solid black line is the fit to the experimental spectrum containing the sum of the simulated response functions for seven gamma rays (solid grey lines) and a double-exponential background (dashed line).

of 9–10% per fragment detected in the S800 focal plane were quoted in earlier experiments on light nuclei (^{11,12}Be, ^{16,17,19}C) [23, 25, 26]. The background fit to the gamma-ray spectra in a later experiment on the heavier ^{34,35}Si and ^{37}S nuclei [27] was between 50% and 237% higher than in the experiments on lighter particles. The background determined for this experiment was again 67% to 85% higher than that quoted for the experiment on Si and S isotopes. There may be evidence for a possible trend in increasing gamma-ray background for increasing mass number or increasing separation energy for the knocked-out nucleons. This trend is hard to quantify with present data, as the heavier Si, S, and Ni nuclei have many gamma rays which impede a clean measurement of the background spectrum.

The initial fit to the experimental spectrum with the energy calibration performed as described in Section 2.3.3 included seven gamma rays plus the double-exponential background. The known 2700.6 keV and 1224.5 keV gamma rays [8, 58–62] from the de-excitation of the excited states at 2700.6 keV ($J^\pi = 2^+$) and 3925.1 keV ($J^\pi = 4^+$) were identified as the most prominent peaks in the gamma-ray spectrum. An excited state at 4935.5(6) keV was observed in a recent beta-decay experiment performed by Borcea *et al.* [62], who tentatively assigned the level to $J^\pi = 3^+$ based on comparisons with several theoretical calculations. Borcea and collaborators also measured 1010.4(4) keV and 2234.5(7) keV gamma rays from the de-excitation of this level to the 4^+ excited state. These two gamma rays were identified in the present experimental spectrum along with the 2700.6 and 1224.5 keV transitions within experimental errors. The more accurate transition energies measured by Borcea *et al.* for all four gamma rays were subsequently used to re-calibrate the gamma-ray spectrum. With the re-calibration of the spectrum, the three other gamma rays observed in the present experiment were assigned energies of 1379(10), 1726(10), and 3027(71) keV. Figure 2.4 shows the final fit (after re-calibration) of the simulated gamma rays and background to the experimental spectrum, as shown by the black solid line. The seven gamma rays plus the double-exponential background produce a good fit, with a chi

Table 2.1: Gamma rays observed in coincidence with ^{56}Ni particles detected at the S800 spectrograph focal plane. Partial cross sections ($\sigma_{\rm exp}$) for each gamma ray are taken from the branching ratio ($\rm I_\gamma$) and the inclusive cross section for one-neutron knockout, $\sigma_{\rm incl} = 45.6(30)$ mb.

E_γ(keV)	$\rm I_\gamma$(%)	$\sigma_{\rm exp}$(mb)
1010.4(4)	4.5(5)	2.0(3)
1224.5(2)	44.5(5)	20.3(13)
1379(10)	6.9(7)	3.1(4)
1726(10)	9.9(10)	4.5(5)
2234.5(7)	5.0(5)	2.3(3)
2700.6(3)	80.6(70)	36.7(40)
3027(71)	3.8(4)	1.7(2)

squared of 1.1 and a smooth residue distribution.

The absolute intensities for each observed gamma ray are listed in Table 2.1. The absolute intensities were determined via the following

$$\rm I_\gamma = \frac{(simulated\ N_\gamma) \times (scale\ factor)}{N_{beam}(^{56}Ni)}, \tag{2.13}$$

where the number of simulated gamma rays (N_γ) was two million in all cases, the scale factor was that used to fit each simulated gamma ray to the experimental spectrum, and the number of ^{56}Ni particles ($N_{\rm beam}(^{56}{\rm Ni})$) was the total detected at the S800 focal plane for all data runs. The intensities were corrected for a fraction of the NaI efficiency that was eliminated in the analysis. The ends and some sections in the center of the scintillators were eliminated in the analysis due to poor energy calibration, but were not eliminated in the GEANT simulations. With this correction the number of total gamma rays (simulated N_γ) $\times$ (scale factor)) was increased by 17.8%.

A simplified level scheme including all gamma-ray transitions observed in this experiment is shown in Figure 2.5. The placement of the 1726(10) and 3027(71) keV gamma rays in coincidence with the 1224.5 and 2700.6 keV gamma rays resulted in a level at 5661(72) keV. A 5668 keV level and associated 1744 keV de-excitation gamma ray were observed by Blomqvist *et al.* in 1985 [59]. While an angular momentum

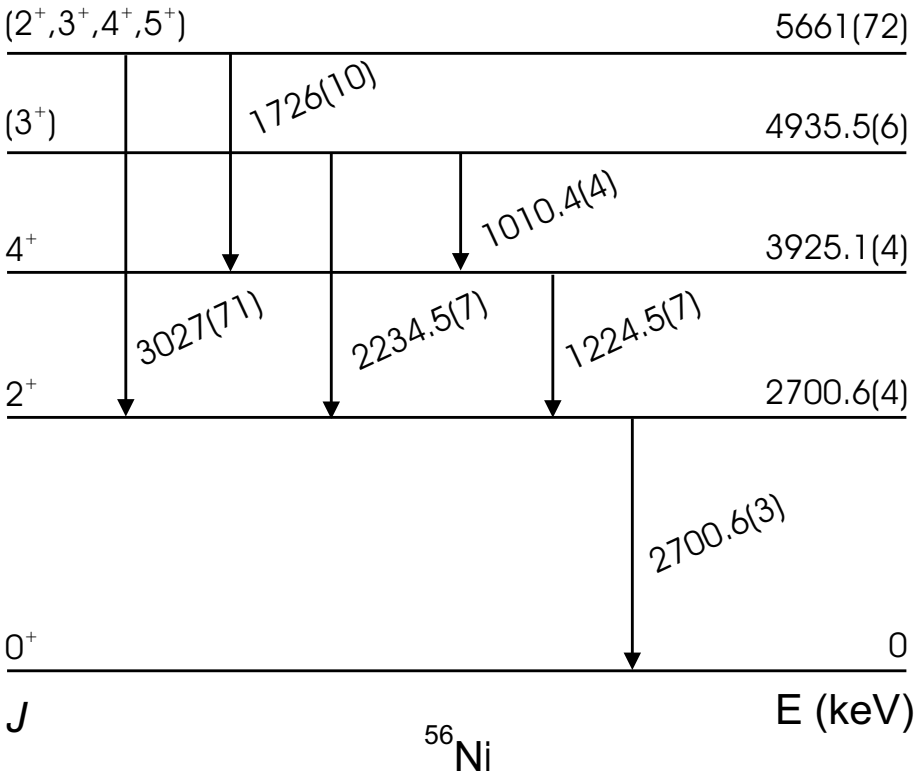

Figure 2.5: ^{56}Ni level scheme, showing gamma rays identified as a result of the present work. Energies, spins and parities for the 2701 and 3925 keV levels were taken from the Nuclear Data Sheets [7]. Energy, spin and parity for the 4935 keV level is taken from Borcea *et al.* [62]. Possible spin and parity assignments for the 5661 keV level are those allowed by angular momentum coupling.

assignment of $J^\pi = 6^+$ was proposed for the 5668 keV level, no errors on the level or gamma-ray energies were reported at the time. We place an error of 72 keV on the observed 5661 keV excited state, and reject the previous angular momentum assignment, as a $J^\pi = 6^+$ level could not be observed in this experiment due to angular momentum considerations. No placement in the proposed level scheme was possible for the gamma ray observed at 1379(10) keV.

The proton separation energy for ^{56}Ni ($S_\mathrm{p} = 7.165(11)$ MeV) is significantly higher than the energy of the highest excited state observed in this experiment, indicating that higher excited states could be populated in the knockout reaction. A shell-model calculation [48] predicted a total of 12 possible excited states from the one-neutron knockout of ^{57}Ni to ^{56}Ni. The energies of the predicted excited states are listed along

Table 2.2: Possible energy levels in ^{56}Ni from one-neutron knockout on ^{57}Ni. Listed are the energy E, spin and parity J^π, isospin T, and spectroscopic factor C^2S for each excited state. Calculations were performed in the many-body shell model with the FPD6 effective interaction [43, 48]. For ^{57}Ni, the $\nu(f_{7/2})$ and $\pi(f_{7/2})$ closed shells plus $\nu(p_{3/2})^1$ were assumed. For ^{56}Ni, calculations were performed with the $\nu(f_{7/2})$ and $\pi(f_{7/2})$ closed shells for the ground state, and for the excited state $\pi(f_{7/2})^8$ and $\nu(f_{7/2})^7$ with the $p_{3/2}$, $f_{5/2}$, and $p_{1/2}$ neutron shells active.

E(MeV)	J^π	T	C^2S
3.32	2^+	0	0.57
4.12	4^+	0	0.54
5.14	3^+	0	0.75
6.02	4^+	0	0.47
6.38	5^+	0	0.67
6.41	4^+	1	1.01
6.63	5^+	1	1.31
6.80	3^+	1	0.85
7.18	2^+	1	0.26
7.19	5^+	0	0.71
7.59	2^+	1	0.37
		total	7.51

with their associated spectroscopic factors in Table 2.2. While excited states up to an energy of 7900 keV were predicted, no higher-lying excited states could be identified experimentally above 5700 keV. Low statistics at high energies contributed to the difficulty in resolving any gamma rays above 3100 keV. In addition, the density of possible excited levels in ^{56}Ni above 3100 keV was too high for the resolution of the NaI(Tl) detectors used in the experiment. Therefore the branching ratios to the individual excited states of ^{56}Ni were not calculated due to the high possibility of indirect feeding from unobserved higher-lying excited states. While low statistics were not a problem at energies lower than 1000 keV, it was not possible to fit any gamma rays in this part of the spectrum due to the presence of the backscatter peaks from the seven fit gamma rays plus 511 keV annihilation gamma rays. The backscatter peaks were caused by gamma-rays which interact first by Compton scattering in one of the materials surrounding the detector and then are detected in the NaI(Tl) detector array. The inclusion in the total fit of any other gamma rays in addition to the seven

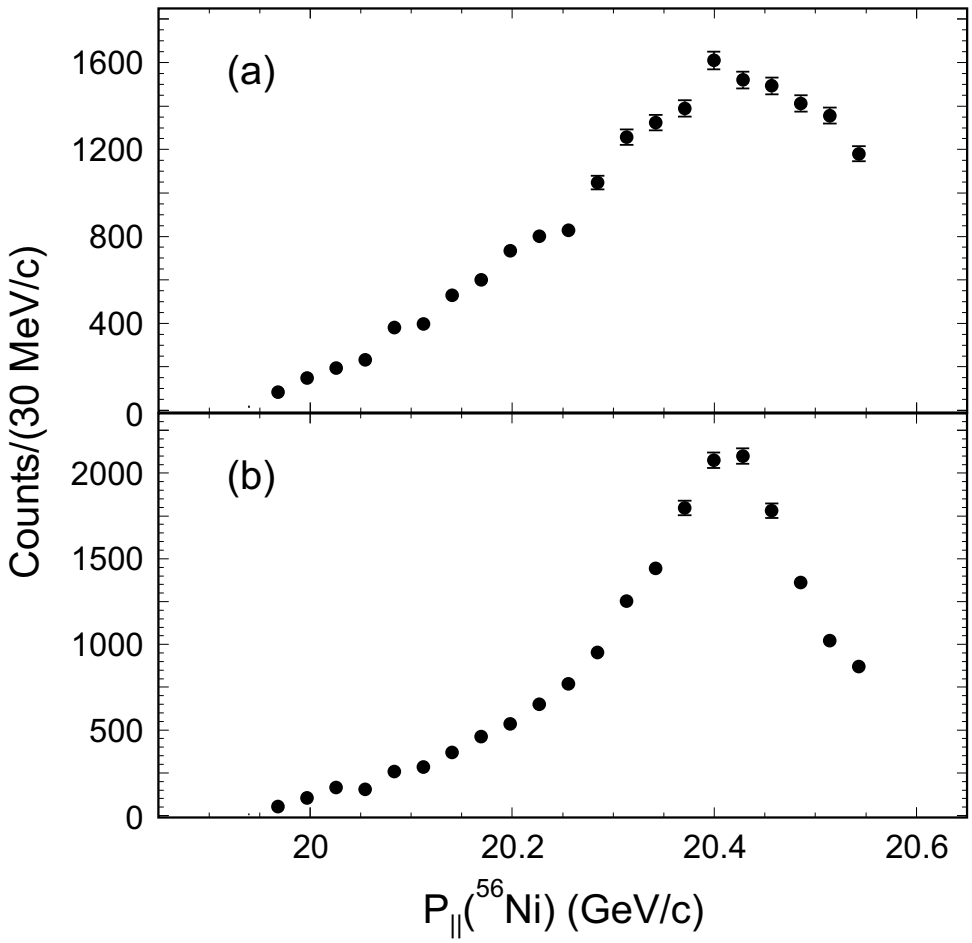

Figure 2.6: Parallel momentum distributions associated with ^{56}Ni fragments detected at the S800 focal plane. The momentum associated with fragments in coincidence with all gamma rays between 250 and 7000 keV is shown in panel (a), while that associated with all other detected ^{56}Ni fragments is shown in panel (b).

presented did not result in a better chi squared fit to the experimental spectrum.

2.4.3 Parallel momentum distributions

The next step in the analysis was to determine the angular momentum associated with one-neutron knockout to the different final states of the ^{56}Ni fragments. The parallel momentum distributions were determined using the reconstructed scattering angle and fractional kinetic energy of the fragments just after the target (see Section 2.3.2), the momentum (20.26 GeV/c), β (0.36), and mass of the fragments. In several previous analyses of knockout experiments, parallel momentum distributions associ-

ated with individual final states of the fragments were extracted [23,25–27]. Due to the complexity of the gamma ray spectrum associated with the ^{56}Ni fragments, however, it was not possible to isolate momentum distributions associated with individual final excited states. Instead, this analysis followed the method of Navin *et al.* [22] for the analysis of one-proton knockout from ^{28}P isotopes. Two parallel momentum distributions were generated, one in coincidence with all gamma rays within the fit range of 250 to 7000 keV (Figure 2.6(a)), and the second in anti-coincidence (Figure 2.6(b)). While one would expect the coincident momentum distribution to contain mainly momenta associated with knockout to the excited states of ^{56}Ni, there is also a significant contribution from particles in coincidence with background events in the gamma-ray spectrum. The anti-coincident momentum distribution mostly represents ^{56}Ni fragments created in their ground state, but also contains contributions from knockout to ^{56}Ni excited states. Due to the finite efficiency of the NaI(Tl) detector array, not all gamma rays emitted from the de-excitation of excited ^{56}Ni fragments were detected. Thus not all fragments detected at the S800 focal plane in anti-coincidence with gamma rays were associated with knockout to the ground state of ^{56}Ni. The momentum distributions to the ground and all excited states of the core fragments were reconstructed from the coincident and anti-coincident spectra. The inclusive parallel momentum distribution (S_{incl}) for all ^{56}Ni fragments detected at the S800 spectrograph focal plane can be written as a sum of the parallel momentum distributions for excited states ($S_{\rm exc}$) and the ground state ($S_{\rm g.s.}$)

$$S_{\rm incl}(p_{\|}) = S_{\rm g.s.}(p_{\|}) + S_{\rm exc}(p_{\|}). \tag{2.14}$$

In order to express the coincident and anti-coincident spectra in terms of $S_{\rm g.s.}$ and $S_{\rm exc}$, it was necessary to introduce two parameters ϵ and δ. The average efficiency ϵ for the NaI(Tl) array is expected to be approximately 50% for an average gamma-ray cascade of two, but was varied in the analysis to determine the best separation

between $S_{\text{g.s.}}$ and S_{exc}. The probability that a gamma ray not originating from the de-excitation of a knockout fragment would be detected in coincidence with that fragment at the S800 focal plane is δ. With the parameters ϵ and δ the coincident (C) and anti-coincident (A) momenta can be expressed as

$$C(p_{\parallel}) = \delta S_{\text{g.s.}}(p_{\parallel}) + (\epsilon + \delta - \epsilon\delta) S_{\text{exc}}(p_{\parallel}) \tag{2.15}$$

$$A(p_{\parallel}) = (1-\delta) S_{\text{g.s.}}(p_{\parallel}) + (1-\delta)(1-\epsilon) S_{\text{exc}}(p_{\parallel}) \tag{2.16}$$

and solved for S_{exc} and $S_{\text{g.s.}}$ to yield

$$S_{\text{exc}}(p_{\parallel}) = \frac{1}{\epsilon}\left(C(p_{\parallel}) - \frac{\delta}{1-\delta} A(p_{\parallel})\right) \tag{2.17}$$

$$S_{\text{g.s.}}(p_{\parallel}) = \left(1 + \frac{\delta}{\epsilon(1-\delta)}\right)\left(A(p_{\parallel}) - \frac{(1-\delta)(1-\epsilon)}{\epsilon+\delta-\epsilon\delta} C(p_{\parallel})\right) \tag{2.18}$$

For this experiment, a value of $\delta = 0.1$ was chosen, in agreement with previous experiments which determined a gamma-ray background of 10% per fragment. The background appears to be higher in this experiment than the 10% assumed in experiments on lighter nuclei. However, with this choice of δ, a consistent separation of the ground state and excited state events was obtained with a choice of $\epsilon = 0.55$. Thus the higher background used in the fit to the gamma-ray spectrum in this experiment may be a result of multiple gamma rays that could not be resolved due to the high level density and low statistics at high energies. A 3.5% systematic error on the number of counts was included in the calculation of experimental cross sections due to the choice of the two parameters. The resulting momentum distributions are shown in Figure 2.7. The errors shown include both statistical errors and the systematic error on the choice of ϵ and δ.

The shell model predicts that one-neutron removal to the ground state would be associated with an $l = 1$ distribution, due to the removal of the $2p_{3/2}$ valence

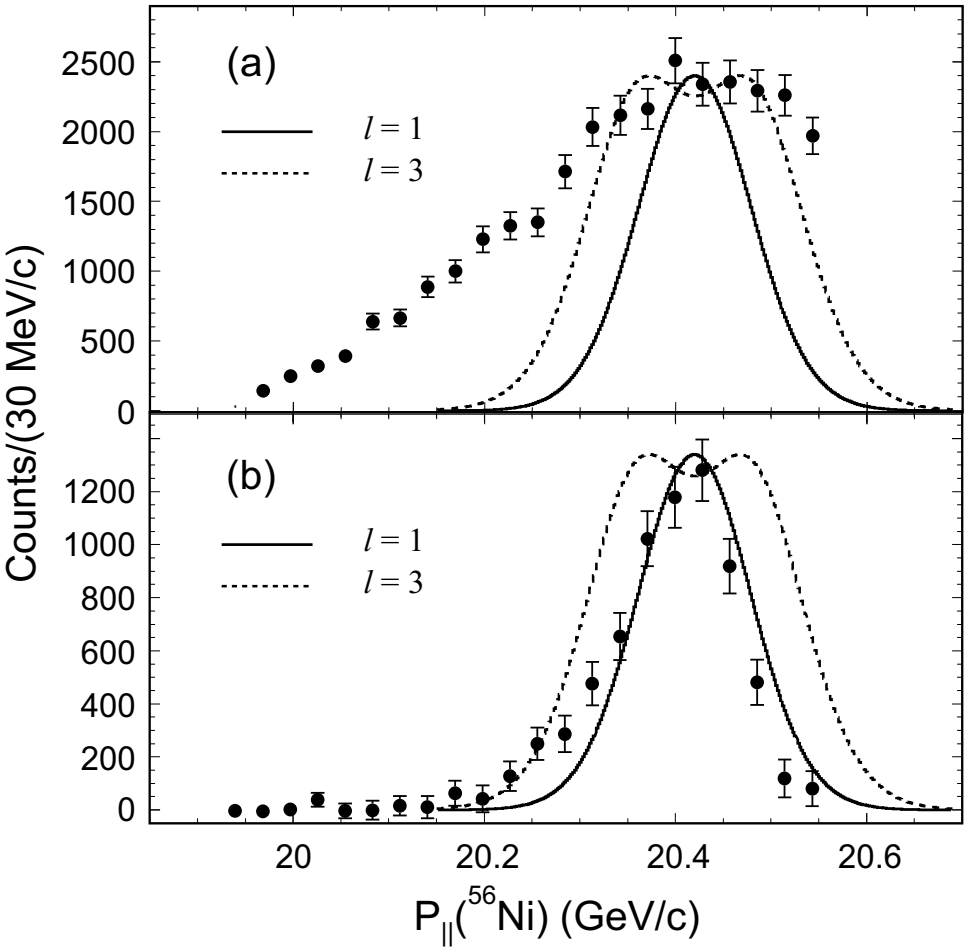

Figure 2.7: Parallel momentum distributions constructed assuming an average efficiency for the NaI(Tl) array of $\epsilon = 0.55$. The probability that a gamma ray not originating from the de-excitation of a knockout fragment would be detected in coincidence with that fragment was assumed to be $\delta = 0.1$. The distribution associated with knockout to all excited states of ^{56}Ni is shown in panel (a), and that to the ground state in panel (b). Momenta in excess of 20.55 GeV/c for ^{56}Ni were not measured.

neutron. Similarly, one-neutron removal to the excited states of ^{56}Ni observed in this experiment would be presumed to correspond to an $l = 3$ momentum distribution, due to the angular momentum of a neutron removed from the $1f_{7/2}$ shell. Theoretical momentum distributions associated with $l = 1$ and $l = 3$ were calculated in the black-disk eikonal model, following the procedure outlined by Hansen [29] and discussed in Section 2.1.2. The calculated angular momentum spectra were scaled to the height and centroid of the experimental data, but the theoretical width was not adjusted. As can be seen in Figure 2.7(b), the ground state distribution is well described by

an $l = 1$ theoretical curve centered at 20.42 GeV/c, in agreement with shell model expectations. The distribution associated with knockout to the excited states of the ^{56}Ni fragments, seen in Fig. 2.7(a), is significantly wider than that associated with knockout to the ground state but is not in good agreement with the theoretical curve for $l = 3$. The width of the distribution makes impossible an assignment of angular momentum less than $l = 3$, however.

Two additional features of the excited state momentum distribution are apparent. First, there was a loss of acceptance at high momenta ($p_{\|} > 20.55$ GeV/c). The large acceptances of the spectrograph should have resulted in a near 100% efficiency for detection of events corresponding to both the ground state and excited state momentum distributions of the ^{56}Ni fragments. However, with the spectrograph operating in dispersion-matched mode, centering of the ^{56}Ni fragments in the S800 focal plane resulted in placement of the high-intensity ^{57}Ni incident beam also within the limits of the focal plane detectors. In order to prevent signals from the incident beam overwhelming the data acquisition system, it was necessary to block the ^{57}Ni particles at the focal plane. This blocked much of the ^{57}Ni contamination from the data acquisition system, but also resulted in the loss of part of the high-momentum tail in both the ground state and excited state momentum distributions. This effect is most apparent in the wider excited state distribution. Secondly, a low-momentum tail extending to approximately 19.95 GeV/c can be seen in the excited state momentum distribution. Momentum excesses at low momenta such as that seen around 20.25 GeV/c in the ground state distribution, but at much lower intensities, have been reported in several previous one-nucleon knockout experiments on ^{11}Be, ^{15}C, and ^{34}Si [23, 27, 63]. Tostevin [64] has shown that the tail in the momentum distribution from the knockout of ^{11}Be can be reproduced using a fully quantum mechanical calculation performed with the CDCC (coupled-channels) method. The tail is significantly larger in the case of the excited-state distribution in this experiment, possibly due to the population of a large number of excited states with different momentum

centroids as a result of the neutron knockout process. This question could be resolved with a gate on individual excited states in the gamma-ray spectrum which was not possible in this experiment. A future nucleon-knockout experiment on nuclei in this mass region with the now available SeGA array of germanium detectors [65] would help to determine if the different momentum centroids of such excited states could produce such a tail. A correction on the number of particles detected in the excited state distribution due to the acceptance loss at high momenta and the low-momentum tail were included in the following determination of cross sections and spectroscopic factors.

2.4.4 Cross sections and spectroscopic factors

The inclusive cross section $\sigma_{\rm incl}$ was calculated from the ratio of ^{56}Ni fragments detected at the spectrograph focal plane to the number of incident ^{57}Ni nuclei, normalized to the number of incident beam particles and multiplied by the target number density

$$\sigma_{\rm incl} = \frac{N_{\rm beam}(^{56}{\rm Ni})/N_{\rm beam}(^{56}{\rm Ni\ total}) \times \mathcal{E}_{\rm DAQ}(^{56}{\rm Ni})}{N_{\rm beam}(^{57}{\rm Ni})/N_{\rm beam}(^{57}{\rm Ni\ total}) \times \mathcal{E}_{\rm DAQ}(^{57}{\rm Ni})} \times \frac{A_t \times 10^{27}}{N_A \times t}. \qquad (2.19)$$

The number of incident ^{57}Ni nuclei ($N_{\rm beam}(^{57}{\rm Ni})$) was determined from the initial data run with the spectrograph magnetic fields set to the momentum of the incident beam. The number of ^{56}Ni for each run ($N_{\rm beam}(^{56}{\rm Ni})$) is determined by the number of counts satisfying all particle identification gates discussed in Section 2.4.1. The number of incident beam particles for each run ($N_{\rm beam}({\rm total})$) is measured by a silicon PIN detector at the exit of the A1200 fragment separator. A_t is the number of atoms in the ^{9}Be target, N_A is Avagadro's number, and t is the thickness of the ^{9}Be target in g/cm^2. The inclusive cross section was calculated run by run and fluctuations in the production rate for ^{56}Ni fragments ($N_{\rm beam}(^{56}{\rm Ni})/N_{\rm beam}(^{56}{\rm Ni\ total})$) were observed. To minimize the error on $\sigma_{\rm incl}$, the average for the three runs closest to the initial ^{57}Ni

Table 2.3: Cross sections and spectroscopic factors for the various final states of ^{56}Ni populated in the ^{9}Be(^{57}Ni,^{56}Ni)X reaction at 73 MeV/nucleon. Theoretical single-particle cross sections ($\sigma_{\rm str}, \sigma_{\rm diff}, \sigma_{\rm sp}$) were calculated in the eikonal model. R_s is defined as the ratio of experimental ($\sigma_{\rm exp}$) to theoretical ($\sigma_{\rm th}$) cross sections.

	ground state	excited states	inclusive
I^π	0^+	2^+–5^+	
l	1	3	
$\sigma_{\rm str}$(mb)	9.66	6.63	
$\sigma_{\rm diff}$(mb)	3.39	1.80	
$\sigma_{\rm sp}$(mb)	13.05	8.43	
$\sigma_{\rm th}$(mb)	13.05	63.23	76.28
$\sigma_{\rm exp}$(mb)	7.7(15)	37.9(26)	45.6(30)
$C^2S_{\rm th}$	1.0	7.5	
$C^2S_{\rm exp}$	0.56(11)	4.3(3)	
R_s	0.56(11)	0.57(4)	0.57(4)

run was used to determine the initial value of $\sigma_{\rm incl}$ = 41.4(12) mb. The error due to the fluctuating rate of ^{56}Ni production was thus reduced to less than one percent.

The partial cross sections to all excited states and the ground state of ^{56}Ni were determined using the same method that generated the parallel momentum distributions. The total number of counts in the raw gamma-coincident (19,030) and anti-coincident (18,845) spectra were entered into Equations 2.17 and 2.18. This allowed for a determination of the branches to the ground state and all excited states — 30,793 counts for $S_{\rm exc}$ corresponding to a branch of 81.3(35)% and 7,082 counts for $S_{\rm g.s.}$ corresponding to a branch of 18.7(35)%. The branches were multiplied by the initial inclusive cross section to determine the cross section to the ground and all excited states. Before the cross sections were finalized, however, a correction for the loss of high-momentum acceptance had to be taken into account. The cross section to all excited states using this method was too low, due to the loss of acceptance at high momenta previously discussed. The correction to the cross section for this loss could take two forms — a large tail at high momenta equal to that at low momenta which would add 5,500 counts to the number of detected ^{56}Ni particles, or a shape above 20.55 GeV/c following the theoretical l = 3 distribution shown in Figure 2.7

which would add 2,300 counts. An average of the corrections for the two cases was added to the excited state cross section, along with the associated error. With this correction applied to the excited state cross section, the cross sections listed in Tables 2.1 and 2.3 were calculated. The final inclusive cross section of 45.6(30) mb was determined by adding the partial cross sections to the ground (7.7(15) mb) and excited (37.9(26) mb) states of the ^{56}Ni fragments.

Theoretical single-particle cross sections were calculated in the eikonal model, as discussed in Section 2.1.2. The calculated stripping and diffraction components for the single-particle cross sections to the ground state and excited states of the fragments are listed in Table 2.3, along with the total theoretical cross sections. With both theoretical and experimental partial cross sections determined, the experimental spectroscopic factors to the ground and all excited states of the ^{56}Ni fragments were calculated according to Equation 2.1. The deduced spectroscopic factors were $C^2S = 0.56(11)$ for the ground state, and $C^2S = 4.3(3)$ for all excited states.

2.5 Discussion

The shell model is expected to most accurately predict the properties of nuclei at or near closed shells. As ^{57}Ni is a semi-magic nucleus with only one neutron outside a doubly-magic core, the shell model should predict well its single-particle occupancies. The observed level scheme (Figure 2.5) shows good agreement with the first four excited states calculated from the shell model in Table 2.2. The shell model also correctly predicts the angular momentum of the knocked-out neutron in its ground state, shown by the good fit of the $l = 1$ distribution to the ground state momentum distribution in Figure 2.7. Although the angular momentum of the knocked-out neutron in its excited state could not be well determined, an angular momentum of at least $l = 3$ can be assigned. The measured partial and inclusive cross sections, however, do not show good agreement with theory (see Table 2.3). The measured cross section to the

Table 2.4: Cross sections and quenching factors for one-nucleon knockout experiments. Separation energies S_p and S_n, beam energies $E_{\rm B}$, experimental ($\sigma_{\rm exp}$) and theoretical ($\sigma_{\rm th}$) inclusive cross sections, and the quenching factor $R_{\rm s} = \sigma_{\rm exp}/\sigma_{\rm th}$ are tabulated. All separation energies are from the Nuclear Data Sheets, except for ^{19}C[j].

One-proton knockout					
	S_p(keV)	$E_{\rm B}$(MeV/nucleon)	$\sigma_{\rm exp}$(mb)	$\sigma_{\rm th}$(mb)	R_s
^{8}B[a]	137.5(12)	76	125(11)	151.3	0.83(7)
^{8}B[b]	137.5(12)	142	109(1)[c]	109(1)	0.86(1)
		285	89(2)[c]	100.6	0.88(2)
		936	94(9)[d]	105.6	0.89(9)
		1440	96(3)[e]	108.8	0.88(3)
				average	0.88(4)
^{26}P[f]	140(20)	65	72(13)	62	1.16(21)
^{27}P[f]	897(35)	65	74(11)	82	0.90(13)
^{9}C[a]	1296.3(25)	78	51.5(42)	65.7	0.78(6)
^{28}P[f]	2066(4)	65	70(11)	54	1.30(.20)
^{16}O[b]	12127.41(1)	2100	54.2(29)[g]	80.2	0.68(4)
^{12}C[b]	15957.0(4)	1050	48.6(24)[h]	96.1	0.51(3)
		2100	53.8(27)[h]	96.1	0.56(3)
				average	0.53(2)
One-neutron knockout					
	S_n(keV)	$E_{\rm B}$(MeV/nucleon)	$\sigma_{\rm exp}$(mb)	$\sigma_{\rm th}$(mb)	R_s
^{11}Be[i]	504(6)	60	259(39)	224	1.16(17)
^{19}C[j]	650(150)	60	264(80)	172	1.53(46)
^{17}C[j]	728(17)	60	115(14)	100	1.15(14)
^{35}Si[k]	2470(40)	73	106(19)	98	1.08(19)
^{16}C[j]	4250(4)	60	77(9)	77	1.00(12)
^{37}S[k]	4303.58(9)	69	99(12)	85	1.16(14)
^{34}Si[k]	7536(21)	73	123(14)	113	1.09(12)
^{57}Ni	10247(11)	73	45.6(3)	75.8	0.60(4)
^{16}O[b]	15663.7(5)	2100	42.9(23)[h]	76.9	0.56(3)
^{12}C[b]	18721.8(10)	1050	44.7(28)[h]	93.4	0.48(3)
		2100	46.5(23)[h]	93.3	0.50(3)
				average	0.49(2)

[a] Ref. [66]
[b] $\sigma_{\rm th}$ and R_s from Ref. [39]
[c] Ref. [69], statistical errors only
[d] Ref. [70]
[e] Weighted average of Ref. [71, 72]
[f] Cross sections from Ref. [22]
[g] Ref. [67]
[h] Ref. [68]
[i] Cross sections from Ref. [23]
[j] Cross sections and S_n from Ref. [26]
[k] Cross sections from Ref. [27]

ground state is 56(11)% of the theoretical ground-state cross section. The measured cross section to all excited states is 57(4)% of the sum-rule theoretical cross section, and the measured inclusive cross section is 57(4)% of the theoretical inclusive cross section. The reductions in observed cross sections translate to reductions in observed spectroscopic factors as compared to those calculated with the shell model.

Several studies have recently been performed to explore this reduction in spectroscopic strength, also observed in other nucleon-knockout experiments [39] as well as inelastic scattering experiments [30]. Inelastic electron scattering experiments have been considered the standard for absolute determination of spectroscopic factors. Kramer *et al.* [30] showed that spectroscopic factors deduced as a result of a series of $(e, e'p)$ experiments on stable nuclei from ^{12}C to ^{208}Pb exhausted only about 60% of the single-particle shell model prediction. In the same review, data from a range of $(d,^3\mathrm{He})$ transfer reaction experiments was reanalyzed. Spectroscopic factors deduced from $(d,^3\mathrm{He})$ experiments had agreed with shell model predictions, but corrections to the range of the transfer reaction and the wave function used brought the spectroscopic factors for transfer reactions in agreement with those from electron scattering.

Electron scattering data is only available for stable nuclei as facilities do not yet exist to perform such experiments on radioactive nuclei. It is also not possible to probe neutron occupancies with electron scattering experiments. In contrast, the technique of one-nucleon knockout can be used to probe both proton and neutron occupancies of radioactive as well as stable nuclei. It then becomes of interest to compare the spectroscopic factors deduced via one-proton knockout reactions to those from electron scattering, and compare the results with spectroscopic factors deduced from one-neutron knockout. Brown *et al.* [39] compared theoretical cross sections calculated in the eikonal model with experimental cross sections from a series of one-nucleon knockout experiments performed at GSI and LBL [67–72] on both stable and radioactive nuclei. In order to facilitate comparison between experiments, a reduction (also called quenching) factor R_s was defined as the ratio between the experimental

and theoretical cross sections ($R_s = \sigma_{\rm exp}/\sigma_{\rm th}$). One-proton knockout on the stable nuclei ^{12}C and ^{16}O resulted in R_s values of 0.53(2) and 0.68(4), in agreement with the reduction factors deduced from the electron scattering experiments. One-neutron knockout from the same two stable nuclei yielded R_s values of 0.49(2) and 0.56(3), suggesting that one-neutron knockout experiments measure the same quantity as one-proton knockout, and thus can also be used to measure absolute spectroscopic factors. Brown *et al.* also compared theoretical cross sections with experimental data for one-proton knockout of the radioactive nucleus ^{8}B. An average reduction factor of 0.88(4) was deduced from four experiments [69–72] at different beam energies. It was suggested that the smaller proton separation energy for the valence proton of ^{8}B compared to that for the stable nuclei may be responsible for the better agreement with shell model predictions.

A third study of the reduction in experimental spectroscopic factors was recently performed by Enders *et al.* [66]. In this case, the two radioactive *p*-shell nuclei ^{8}B and ^{9}C were studied via one-proton knockout. This study differed from that of Brown *et al.* in that the secondary beam energies used were significantly lower, 76 and 78 MeV/nucleon for ^{8}B and ^{9}C, respectively. The results provide further evidence that the reduction in spectroscopic factors relative to the shell model decreases as one moves farther from stability. R_s values of 0.83(7) and 0.78(6) were determined for ^{8}B and ^{9}C. It is suggested that the short-range part of the nucleon-nucleon interaction may explain some or all of the observed reduction in spectroscopic factors. The repulsive short-range part of the interaction becomes important at distances less than 0.4 fm, and leads to high-momentum components of the nucleon wave function [73]. Such components would be difficult to measure experimentally, and would be observed as a reduction in the single-particle occupancies relative to those calculated in the shell model.

The R_s factors for one-nucleon knockout for a range of nuclei are listed in Table 2.4. In this analysis, only R_s values for inclusive one-proton and one-neutron knockout

cross sections were examined. In Figure 2.8, the R_s values are plotted as a function of proton and neutron separation energy. All data from single-nucleon knockout experiments in references [22, 23, 26, 27, 39, 66] are included, excluding the anomalous value for the one-proton knockout on ^{25}Al (see Ref. [22]). The results for one-proton knockout are shown in Figure 2.8(a). A trend toward decreasing R_s with increasing proton separation energy can be suggested, although the R_s values for ^{26}P and ^{28}P are high even when one includes the large error on both values. The results from one-neutron knockout are shown in Figure 2.8(b). Again, there may be decrease in R_s with increasing separation energy. The contribution from the present work is indicated in Figure 2.8(b) by a star. The reduction in single-particle occupancy observed in the case of radioactive ^{57}Ni is in much closer agreement with the reductions for the single-neutron knockout from the two stable nuclei ^{12}C and ^{16}O than with those for the radioactive nuclei. One could argue that aside from ^{12}C, ^{16}O, and ^{57}Ni, all other reduction factors are consistent with 1.0 (no quenching) within experimental errors. It is difficult to draw conclusions for R_s trends as a function of separation energy with few data points on radioactive nuclei. It will also be necessary to perform one-proton knockout on nuclei in the separation energy range between 2.1 and 12 MeV, to gather more evidence for a trend in R_s. Further studies are needed, especially on heavier stable and radioactive magic or semi-magic nuclei.

The quenching observed in electron scattering experiments for stable nuclei from ^{12}C to ^{208}Pb appears to extend to well-bound radioactive nuclei such as ^{57}Ni. Thus the observation of approximately 50% reduction in the spectroscopic factors for the ground state of ^{57}Ni are likely due to the difficulty of observing the full spectroscopic factors, and not due to mixing of ^{56}Ni core excitations in the ^{57}Ni ground state wave function. The current experiment agrees with the previous measurement of spectroscopic factors for the low-lying states of ^{57}Ni [50] in concluding that ^{57}Ni can be described well by the single-particle model.

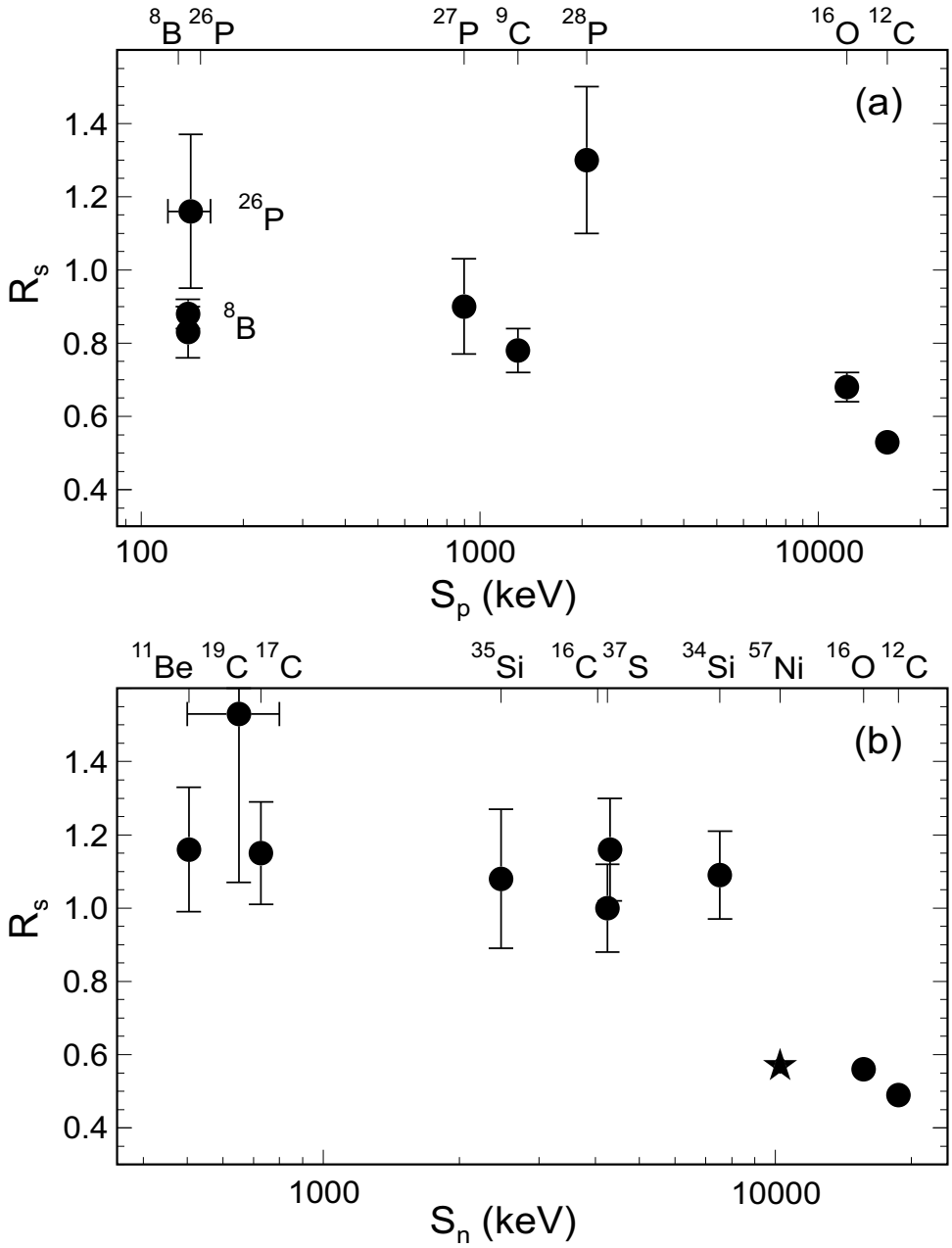

Figure 2.8: Quenching R_s versus proton (S_p) and neutron (S_n) separation energy for one-proton (a) and one-neutron (b) knockout experiments. R_s is defined as the ratio between experimental and theoretical inclusive cross sections. The data point indicated by a star is from this work. See Table 2.4 for references.

Chapter 3

Coulomb Excitation of Neutron-Deficient Nickel Isotopes

3.1 Intermediate-energy Coulomb excitation

3.1.1 Description of experimental method

The well-established experimental method of Coulomb excitation has yielded a wealth of nuclear structure information for stable nuclei [74, 75]. One nucleus, traditionally located in a target, is excited in the Coulomb field of another, traditionally a projectile with an energy well below the Coulomb barrier. This low energy assures that only Coulomb excitation takes place with no contribution from nuclear excitations due to the strong force. The gamma rays (or other particles such as conversion electrons) detected as the target nucleus de-excites allows for a measurement of the energy spacing between the bound nuclear states. The measured cross section for Coulomb excitation is directly proportional to the nuclear matrix elements $B(\mathrm{E}\lambda)$ and $B(\mathrm{M}\lambda)$ connecting the two levels. Thus one Coulomb excitation measurement allows for simultaneous measurement of two fundamental quantities in nuclear structure, the energy of an excited bound state and the nuclear matrix element connecting it to the ground state.

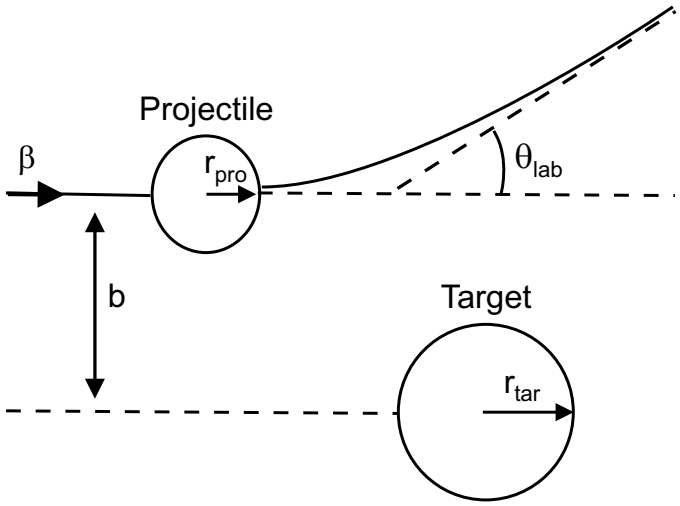

Figure 3.1: Diagram of scattering trajectories for an infinitely heavy target nucleus. The scattering angle θ is chosen to assure that b is equal to the sum of the target and projectile radii plus at least 2 fm.

In order to study radioactive nuclei, the method of intermediate-energy Coulomb excitation is used [76–80]. As radioactive nuclei cannot be prepared into targets, a stable, high-Z target is used to excite the projectile nucleus of interest. Both the target and projectile nuclei can be excited as a result of their interaction, but the photons emitted by the moving projectile can be easily distinguished from those emitted by the stationary target due to Doppler broadening. At the NSCL, the nuclei of interest are produced in fragmentation reactions and have an energy of 30–100 MeV/nucleon (see Section 2.3.1). As the energies are well above the Coulomb barrier, the dominance of Coulomb interactions over nuclear interactions is assured by choosing extremely forward scattering angles. As shown in Figure 3.1, the choice of laboratory scattering angle θ_{lab} fixes the range of impact parameters. The impact parameter b is related to the scattering angle in the center-of-mass frame θ_{cm} via [81]

$$b = \frac{a}{\gamma} \cot\left(\frac{\theta_{cm}}{2}\right), \tag{3.1}$$

where

$$a = \frac{Z_{pro} Z_{tar} e^2}{m_o c^2 \beta^2}. \tag{3.2}$$

Z_{pro} and Z_{tar} are the charge of the projectile and target nuclei, m_o is the reduced mass of the projectile-target system ($m_o = (m_{pro}m_{tar})/(m_{pro} + m_{tar})$), and β and γ are the relativistic factors for the velocity of the projectile (v) in the laboratory frame defined as

$$\gamma = \frac{1}{\sqrt{1-\beta^2}} \quad \text{and} \quad \beta = \frac{v}{c}. \tag{3.3}$$

The scattering angle in the center-of-mass frame is related to the laboratory scattering angle

$$\tan\theta_{lab} = \frac{\sin\theta_{cm}}{\gamma_{cm}(\cos\theta_{cm} + (\beta_{cm}/\beta))}, \tag{3.4}$$

where β_{cm} is the velocity of the center-of-mass frame with respect to the laboratory frame[1]. Choice of small θ_{lab} assures peripheral collisions of the two nuclei. Experimentally, a maximum scattering angle θ_{lab}^{max} corresponding to a minimum impact parameter b_{min} equal to at least 2 fm plus the sum of the target and projectile radii is chosen. With the radii of the projectile and target nuclei approximated as $r = 1.25$ fm $A^{1/3}$ [82], a minimum impact parameter of $b_{min} = 14$ fm and thus a maximum scattering angle of $\theta_{lab}^{max} = 2.8°$ is chosen for scattering of ^{56}Ni projectiles at $\beta = 0.4$ on a ^{197}Au target.

The semiclassical theory for relativistic Coulomb excitation was derived by Alder and Winther [76]. Nuclei are assumed to follow straight-line trajectories with excitation probabilities calculated in time-dependent perturbation theory. As the maximum scattering angle in the laboratory chosen to assure the dominance of Coulomb excitation is only a few degrees, the straight-line assumption is valid at high energies. At intermediate energies, however, the recoil of the target nucleus modifies the straight-line trajectory of the projectile. The lowest order correction for deviations from the

[1]For the Coulomb excitation experiments discussed here with $A_{pro} \approx (1/4)A_{tar}$, three frames of reference must be defined— the laboratory frame, the frame of the incident projectile, and the frame of the projectile-target center of mass. Where no subscript is attached, β and γ refer to the velocity of the incident projectile in the laboratory frame.

straight-line trajectory, included for a more complete solution, is [76]

$$b \rightarrow b + \frac{\pi a}{2\gamma}. \tag{3.5}$$

3.1.2 Excitation cross section and reduced transition probability

The theory of relativistic Coulomb excitation has been described in-depth previously [76, 77, 81, 83]. A summary of results pertinent to the analysis of the Coulomb excitation experiments discussed here is presented. The equations that follow refer to the excitation of the projectile nucleus by the Coulomb field of the target, as is the case for the present experiments. To obtain the equations for excitation of the target nucleus, replace the charges Z_{tar} by Z_{pro} and the reduced transition probabilities B_{pro} with B_{tar}.

The cross section for Coulomb excitation (CE) can be written in terms of the cross section for Rutherford scattering

$$\left(\frac{d\sigma}{d\Omega}\right)_{CE} = \left(\frac{d\sigma}{d\Omega}\right)_{Ruth} P_{i\rightarrow f}, \tag{3.6}$$

where $P_{i\rightarrow f}$ is the probability of excitation from the initial nuclear state $|\mathrm{i}\rangle$ with energy E_i to the final state $|\mathrm{f}\rangle$ with energy E_f, defined as

$$P_{i\rightarrow f} = \left|a_{i\rightarrow f}\right|^2. \tag{3.7}$$

In the experiments discussed here, the initial state of the nucleus is always the ground state. The excitation amplitude $a_{i\rightarrow f}$ is expressed in terms of the electromagnetic interaction potential $V(\mathbf{r}(t))$. This time-dependent potential can be treated as a per-

turbation on the nuclear wave function. Thus the excitation amplitude has the form

$$a_{i\to f} = \frac{1}{i\hbar}\int_{-\infty}^{\infty} \mathrm{e}^{(i(E_f - E_i)t)/\hbar}\,\langle \mathrm{f}|V(\mathbf{r}(t))|\mathrm{i}\rangle\, dt, \tag{3.8}$$

assuming that the electromagnetic field excites the target weakly. The amplitude for excitation $a_{i\to f}$ can also be expressed as

$$a_{i\to f} = i\sum_{\lambda} \chi^{(\lambda)}_{i\to f}\, f_\lambda(\xi), \tag{3.9}$$

where χ measures the strength of the interaction and $f_\lambda(\xi)$ measures the degree of adiabacity. For both electric and magnetic transitions,

$$\chi^{\pi\lambda}_{i\to f}(b) \approx \frac{Z_{tar} e\langle \mathrm{f}|\mathcal{M}(\pi\lambda\mu)|\mathrm{i}\rangle}{\hbar\, c\, b^\lambda}. \tag{3.10}$$

The adiabacity parameter ξ can be thought of as the ratio between the collision time and the internal motion of the nucleus to be excited. The collision time must be much shorter than the time of the nucleus' internal motion in order for an excitation to occur. With the high velocities of the projectiles in intermediate-energy Coulomb excitation, collision times are very short. The adiabacity parameter for relativistic Coulomb excitation has the form

$$\xi = \frac{E_f - E_i}{\hbar}\frac{b}{\gamma\beta c}, \tag{3.11}$$

with the impact parameter b modified as shown in Equation 3.5.

To calculate the excitation cross section, the excitation probability is integrated over impact parameters from b_{min} to infinity

$$\sigma_{i\to f} = 2\pi\int_{b_{min}}^{\infty} P_{i\to f}\, b\, db. \tag{3.12}$$

The function $f_\lambda(\xi)$ in Equation 3.9 is approximated as a step function, introducing

an adiabatic cutoff when $\xi = 1$. With the adiabatic cutoff approximation, the cross section can be estimated

$$\sigma_{i\to f} \approx 2\pi \int_{b_{min}}^{b_{max}} |\chi|^2 \, b \, db, \tag{3.13}$$

where the upper limit b_{max} is the impact parameter corresponding to $\xi = 1$. Inserting χ, the excitation cross section can be approximated as

$$\sigma_{\pi\lambda} \approx \left(\frac{Z_{tar}e^2}{\hbar c}\right) \frac{B_{pro}(\pi\lambda, 0 \to \lambda)}{e^2} \, \pi \, b_{min}^{2(1-\lambda)} \begin{cases} (\lambda-1)^{-1} & for \lambda \geq 2 \\ 2 \, \ln(b_{max}/b_{min}) & for \lambda = 1 \end{cases} \tag{3.14}$$

for transition parity π and multipolarity λ. The reduced transition probability for the projectile ($B_{pro}(\pi\lambda, I_i \to I_f)$) is related to the reduced matrix element

$$B_{pro}(\pi\lambda, I_i \to I_f) = \frac{1}{2I_i + 1} \left|\langle I_f \| \mathcal{M}(\pi\lambda) \| I_i \rangle\right|^2, \tag{3.15}$$

where $\mathcal{M}(\pi\lambda)$ is the multipole operator for electromagnetic transitions. The exact expression for the excitation cross section, summed over π and λ, is equal to [76]

$$\sigma_{i\to f} = \left(\frac{Z_{tar}e^2}{\hbar c}\right)^2 \sum_{\pi\lambda\mu} \left(\frac{E_f - E_i}{\hbar c}\right)^{2(\lambda-1)} \frac{B_{pro}(\pi\lambda, I_i \to I_f)}{e^2} \left|G_{\pi\lambda\mu}(\beta^{-1})\right|^2 g_\mu(\xi(b_{min})). \tag{3.16}$$

The Winther and Alder functions $g_\mu(\xi)$ is

$$g_\mu(\xi(b_{min})) = \pi\xi^2 \left[|K_{\mu+1}(\xi)|^2 - |K_\mu(\xi)|^2 - \frac{2\mu}{\xi} K_{\mu+1}(\xi) K_\mu(\xi)\right], \tag{3.17}$$

where $K(\xi)$ are the modified Bessel functions and μ is the angular momentum transfer along the beam direction

$$\mu = M_i - M_f. \tag{3.18}$$

For electric excitations and $\mu \geq 0$, $\pi = \mathrm{E}$ and

$$G_{\mathrm{E}\lambda\mu}(\beta^{-1}) = i^{\lambda+\mu}\frac{\sqrt{16\pi}}{\lambda(2\lambda+1)!!}\left(\frac{(\lambda-\mu)!}{(\lambda+\mu)!}\right)^{1/2}\left(\beta^{-2}-1\right)^{-1/2} \times\left(\frac{(\lambda+1)(\lambda+\mu)}{2\lambda+1}P^{\mu}_{\lambda-1}(\beta^{-1}) - \frac{\lambda(\lambda-\mu+1)}{2\lambda+1}P^{\mu}_{\lambda+1}(\beta^{-1})\right). \tag{3.19}$$

For magnetic excitations and $\mu \geq 0$, $\pi = \mathrm{M}$ and

$$G_{\mathrm{M}\lambda\mu}(\beta^{-1}) = i^{\lambda+\mu+1}\frac{\sqrt{16\pi}}{\lambda(2\lambda+1)!!}\left(\frac{(\lambda-\mu)!}{(\lambda+\mu)!}\right)^{1/2}\left(\beta^{-2}-1\right)^{-1/2}\mu\,P^{\mu}_{\lambda}(\beta^{-1}). \tag{3.20}$$

$P^{\mu}_{\lambda}(\beta^{-1})$ is the associated Legendre function, evaluated for values of $\beta^{-1} > 1$. For $\mu < 0$,

$$\begin{aligned} G_{\mathrm{E}\lambda-\mu}(\beta^{-1}) &= (-1)^{\mu}G_{\mathrm{E}\lambda\mu}(\beta^{-1}) \\ G_{\mathrm{M}\lambda-\mu}(\beta^{-1}) &= -(-1)^{\mu}G_{\mathrm{M}\lambda\mu}(\beta^{-1}). \end{aligned} \tag{3.21}$$

3.1.3 Gamma-ray angular distributions

The Coulomb excitation process does not populate the magnetic substates of the excited state evenly and thus the angular distribution of emitted photons is anisotropic [74, 83]. The angular distribution of emitted gamma rays then becomes important for the calculation of detector efficiency, as discussed in Appendix B. The theory of angular distributions for intermediate-energy Coulomb excitation is derived in References [74, 76, 83], and only final results are presented here.

The angular distribution $W(\theta)$ is

$$W(\theta) = \sum_{\substack{k \text{ even},\,\mu \\ L,L'}} |G_{\lambda\mu}(\beta^{-1})|^2 g_{\mu}(\xi)(-)^{\mu}\begin{pmatrix} \lambda & \lambda & k \\ \mu & -\mu & 0 \end{pmatrix} \tag{3.22}$$

$$\times\begin{Bmatrix} I_f & I_f & k \\ \lambda & \lambda & I_i \end{Bmatrix} F_k(L,L',I_{ff},I_f)\sqrt{2k+1}\,P_k(\cos\theta)\,\delta_L\delta_{L'}. \tag{3.23}$$

The Winther and Alder functions $g_{\mu}(\xi)$ are given by Equation 3.17, $G_{\lambda\mu}(\beta^{-1})$ by

Equations 3.20 and 3.20, and the $P_k(\cos\theta)$ are Legendre polynomials. The $\delta_L\delta_{L'}$ are related to the mixing ratio, and are discussed in detail by Alder *et al.* [74]. The gamma-gamma correlation function $F_k(L, L', I_{ff}, I_f)$ is [74]

$$F_k(L, L', I_{ff}, I_f) = (-)^{I_{ff}+I_f-1}\sqrt{(2L+1)(2L'+1)(2k+1)(2I_f+1)} \quad (3.24)$$

$$\times \begin{pmatrix} L & L' & k \\ 1 & -1 & 0 \end{pmatrix} \begin{Bmatrix} L & L' & k \\ I_f & I_f & I_{ff} \end{Bmatrix}. \quad (3.25)$$

The angular distribution is usually expressed as

$$W(\theta) = \sum_{k\text{even}} a_k P_k(\cos\theta), \quad (3.26)$$

where the coefficients a_k were calculated [84] in MATHEMATICA.

3.1.4 Experimental cross section and transition rates

Experimental cross section

The experimental cross section for Coulomb excitation is

$$\sigma = \frac{N_\gamma}{\epsilon_{tot} \times N_{beam} \times N_{target}}, \quad (3.27)$$

where N_γ is the number of detected de-excitation photons, ϵ_{tot} is the total detector efficiency, N_{beam} is the number of incident secondary beam nuclei, and N_{target} is the number of target nuclei per unit area. The total efficiency (ϵ_{tot}) includes contributions from the detector efficiency, solid angle covered by the detector array, angular distributions of emitted gamma rays due to the reaction mechanism and Lorentz boost,

and absorption of gamma rays in the target material, and is given by

$$\epsilon_{tot} = \epsilon(E_\gamma)_{lab}^{iso,boosted} \times \delta_{\text{GEANT}} \times \frac{\sum_{\theta_{pro}} N_{\theta_{pro}} W(\theta_{pro}) \sin\theta_{pro}}{\frac{1}{4\pi}\sum_{\theta_{pro}} N_{\theta_{pro}} \sin\theta_{pro}}. \tag{3.28}$$

The Lorentz-boosted laboratory-frame efficiency at the Doppler-shifted gamma-ray energy of interest is $\epsilon(E_\gamma)_{lab}^{iso,boosted}$, δ_{GEANT} is a scaling factor applied to adjust the simulated efficiency to the measured efficiency, and $W(\theta_{pro})$ is the non-Lorentz-boosted angular distribution at a given projectile-frame angle. The angular distribution $W(\theta_{pro})$ is weighted with the number of gamma rays detected in the SeGA array at each angle N_θ. Details of the efficiency calculation can be found in Appendix B. The target density per unit area is calculated as

$$N_{target} = \frac{N_A \times \rho}{A}, \tag{3.29}$$

where N_A is Avagadro's number ($N_A = 6.022 \times 10^{23}$ particles/mol), ρ is the target density in g/cm^2, and A is the atomic mass of the target nuclei in g/mol.

Selection rules

The transition between an initial nuclear state I_i^π and a final state I_f^π is usually dominated by the lowest multipolarity λ allowed by angular momentum and parity selection rules [82]. A transition between nuclear states vanishes unless $\mathbf{I_f} = \boldsymbol{\lambda} + \mathbf{I_i}$. Thus the angular momentum selection rule for electromagnetic excitation is

$$|I_f - I_i| \leq \lambda \leq I_f + I_i. \tag{3.30}$$

The parity selection rules are

$$\pi_i\pi_f = (-1)^{\lambda} \quad \text{for} \quad \mathrm{E}\lambda$$
$$\pi_i\pi_f = (-1)^{\lambda+1} \quad \text{for} \quad \mathrm{M}\lambda. \tag{3.31}$$

Electromagnetic transition rates

The transition rate $\mathcal{W}$, or the number of decays per unit time, can be related to the reduced transition probability [82]

$$\mathcal{W}(\pi\lambda; I_2 \to I_1) = \frac{8\pi(\lambda+1)}{\hbar\lambda[(2\lambda+1)!!]^2}\left(\frac{E_\gamma}{\hbar c}\right)^{2\lambda+1} B(\pi\lambda; I_2 \to I_1), \tag{3.32}$$

where $B(\mathrm{E}\lambda)$ has units $e^2\mathrm{fm}^{2\lambda}$ and $B(\mathrm{M}\lambda)$ has units $\mu_N^{2\lambda-2}$. When relating the transition rate to the reduced transition probability in Equation 3.32, I_2 is the excited state of the nucleus and I_1 is the ground state. Thus $B(\lambda; I_2 \to I_1)$ represents the reduced transition probability for de-excitation of the nucleus, henceforth written $B(\pi\lambda\downarrow)$. The corresponding reduced transition probability for excitation will be written $B(\pi\lambda\uparrow)$. The relation between the two reduced transition probabilities is

$$B(\pi\lambda; I_1 \to I_2) = \frac{2I_2+1}{2I_1+1} B(\pi\lambda; I_2 \to I_1), \tag{3.33}$$

or

$$B(\pi\lambda\uparrow) = \frac{2I_f+1}{2I_i+1} B(\pi\lambda\downarrow), \tag{3.34}$$

where I_f is the excited bound state of the Coulomb-excited nucleus, and I_i is the ground state.

The half-life $T_{1/2}$ and width Γ of an excited bound state of a nucleus can be determined from the transition rate

$$T_{1/2} = \frac{\ln 2}{\mathcal{W}} \quad \text{and} \quad \Gamma = \hbar\mathcal{W}. \tag{3.35}$$

Competition between electric and magnetic excitations

If the selection rules 3.30 and 3.31 allow transitions of more than one multipolarity for a given nuclear excitation, the excitation cross sections add [78]

$$\sigma = \sum_{\pi\lambda} \sigma_{\pi\lambda}. \tag{3.36}$$

For a given λ, using Equation 3.32 and the selection rules for electromagnetic transitions [82],

$$\mathcal{W}(\mathrm{E}\lambda) \gg \mathcal{W}(\mathrm{E}\lambda+1) \quad \text{and} \quad \mathcal{W}(\mathrm{M}\lambda) \gg \mathcal{W}(\mathrm{M}\lambda+1). \tag{3.37}$$

The transition with lower multipolarity for a given parity (E or M) will dominate. While magnetic transitions are weaker than electric transitions for a given λ, if both the Mλ and E$(\lambda+1)$ transitions are allowed, they may become competitive in the transition rate. Thus the mixing ratio for the Mλ and E$(\lambda+1)$ components must be determined [82]

$$\delta^2 = \frac{\mathcal{W}(E(\lambda+1))}{\mathcal{W}(M\lambda)}. \tag{3.38}$$

3.2 Experimental setup

The series of Coulomb excitation experiments on the Ni isotopes was performed at the Coupled Cyclotron Facility of the NSCL. This upgrade, completed in 2001, allowed the two superconducting cyclotrons (K500 and K1200) at the NSCL to be used in tandem. Thus stable nuclei could be accelerated to higher energies and intensities than before, allowing for the production and study of nuclear species with shorter half-lives. This represents an improvement on the facility as described in Section 2.3 for one-nucleon knockout of ^{57}Ni, as nuclei farther from the valley of stability (such as ^{54}Ni) could be produced in sufficient quantities for study. Due to the short lifetimes of the nuclei under study, measurements were again performed in inverse kinematics

Table 3.1: Secondary beam characteristics for Coulomb excitation experiments. The primary beam was ^{58}Ni at 140 MeV/nucleon.

Secondary Beam	^{9}Be Production Target (mg/cm^2)	Energy (MeV/nucleon)	Intensity (s^{-1})	Data Acquisition Time (hours)
^{58}Ni	790	77.8	8000	4.0
^{56}Ni	423	85.8	3300	21.4
^{55}Ni	423	84.8	680	58.9
^{54}Ni	376	70.3	65	91.7

as described in Section 2.3.

3.2.1 Secondary beam production

A primary beam of ^{58}Ni was used to produce beams of ^{54,55,56}Ni for Coulomb excitation. The primary beam of ^{58}Ni was extracted from a room-temperature ECR source and transported to the K500 cyclotron, where it underwent initial acceleration. Once the stable beam was at maximum acceleration in the K500 cyclotron, it was transported to the K1200 cyclotron and accelerated to an energy of 140 MeV/nucleon. The primary beam was then incident on a thick ^{9}Be production target to produce secondary beams of the different Ni isotopes and other fragmentation products. The A1900 fragment separator [85], which represents an upgrade of the A1200 fragment separator previously discussed in Section 2.3.1, was used to select the secondary beams at the energies of interest and transport them to the experimental area. The different secondary beams with their production targets, energies, intensities, and data acquisition times are listed in Table 3.1. In order to provide better identification of the different nuclei in each secondary beam, a 445.5 mg/cm^2 Al wedge was used in the fragment separator for purification of the ^{58}Ni, ^{56}Ni and ^{55}Ni secondary beams. Due to the lower intensity of the ^{54}Ni secondary beam, a thinner 238.4 mg/cm^2 Al wedge was used.

The experimental setup for the Coulomb excitation experiments (Figure 3.2) was very similar to that used for the one-nucleon knockout experiment described in Chap-

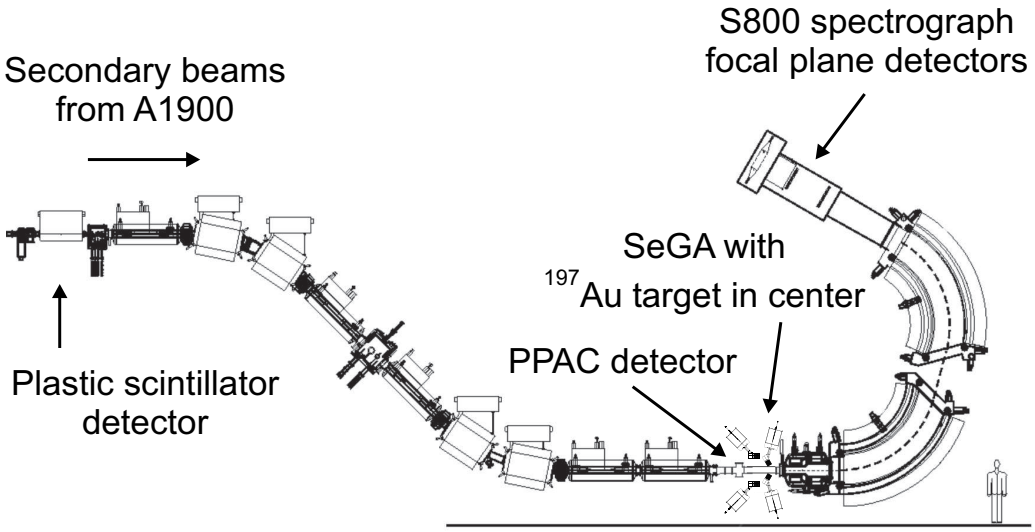

Figure 3.2: Schematic of the experimental setup for the Coulomb excitation of neutron-deficient Ni isotopes at the NSCL.

ter 2. The S800 spectrograph was used to identify the particles of interest after interaction with the Coulomb excitation target, and a gamma-ray detector array surrounded the target. The NaI(Tl) detector array used in the one-neutron knockout experiment was replaced in this experiment by an array of eighteen thirty-two-fold high-purity segmented germanium detectors (SeGA) [65]. The secondary Coulomb excitation targets (184.1 mg/cm^2 or 257.7 mg/cm^2 ^{197}Au) were placed at the center of the SeGA array. The S800 spectrograph is briefly discussed in Section 3.2.2, while the SeGA array is described in more detail in Section 3.2.3.

3.2.2 S800 spectrograph and particle identification

The S800 spectrograph was used to identify the inelastically scattered secondary beam particles of interest after their interaction with the Coulomb excitation target. Characteristics of the spectrograph and details of the focal plane detectors were previously discussed in Section 2.3.2. The spectrograph was operated in dispersion-matched mode, limiting the spread in incident momentum from the A1900 fragment separator to $\pm 0.5\%$.

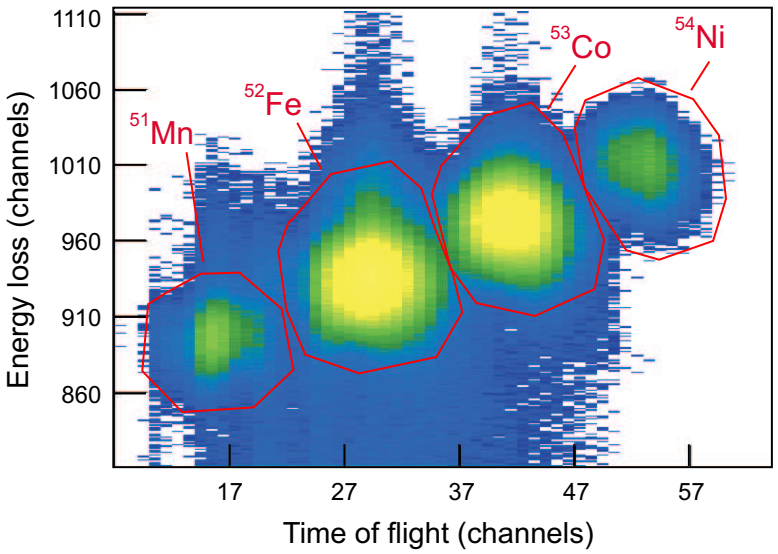

Figure 3.3: Representative particle identification spectrum for ^{54}Ni and ^{52}Fe at the S800 spectrograph focal plane. The A1900 fragment separator and S800 spectrograph settings were optimized for ^{54}Ni. Shown is the cumulative data for all runs totaling approximately 92 hours. Energy loss was measured in the ion chamber of the S800 focal plane, and time of flight was measured from a scintillator at the exit of the A1900 fragment separator to the first scintillator of the S800 focal plane.

Identification of the fragments of interest was carried out with the focal plane detectors of the S800 spectrograph [54], two plastic scintillator detectors located at the exit of the A1900 fragment separator and the entrance to the S800 analysis line, and a parallel-plate avalanche counter (PPAC) located just before SeGA. The secondary beams transported through the A1900 fragment separator were not pure beams of the nucleus of interest, but "cocktail beams" that contained several nuclei (see Figure 3.3 for an example). Thus it was necessary to place a primary gate on the nucleus of interest before the Coulomb excitation target, followed by a secondary gate on the inelastically scattered nucleus after interaction with the target. The time difference between a particle's interaction with the two scintillators in the beam line allowed for the primary identification of the nucleus of interest before interaction with the Coulomb excitation target. After the beam's interaction with the target, a range of fragmentation products were produced along with the inelastically scattered secondary beam. Secondary gates on the inelastically-scattered beam after Coulomb

excitation were placed on a plot of energy loss in the S800 focal plane ion chamber versus time of flight. This time of flight was measured between the plastic scintillator detector located at the exit of the A1900 fragment separator and the first scintillator of the S800 focal plane. The plot of energy loss in the ion chamber versus time-of-flight provided a better separation between the nuclei in the cocktail beam before the interaction with the ^{197}Au target, and was used in addition to the primary gate on the incident beam from the scintillator time difference. An example of an energy loss versus time of flight spectrum for the cocktail beam associated with the ^{54}Ni secondary beam is shown in Figure 3.3. A third gate was placed on the position of the incoming secondary beam particles in the PPAC detector located before the Coulomb excitation target. As the beam was dispersion-matched, the beam was spread over the length of the PPAC detector in the dispersive direction. A software gate was placed on the PPAC spectrum to only exclude the edges of the active area of the PPAC in both the dispersive and non-dispersive directions, to eliminate overflows from particles' interactions at the very edge of the detector area.

3.2.3 The MSU Segmented Germanium Detector Array

Due to the high energies (70–85 MeV/nucleon) of the incoming secondary beams, an array of position-sensitive gamma-ray detectors was necessary to determine the angle of the emitted gamma ray and thus the energy of the gamma ray in the rest frame of the particle of interest. For the Coulomb excitation experiments, the new array of eighteen thirty-two-fold high-purity segmented germanium detectors (SeGA) [65] was used to detect the gamma rays emitted from de-excitation of the nuclei of interest (see Equation 2.9). The intrinsic energy resolution of the SeGA detectors is approximately 2.5–2.8 keV (0.2%) at 1332 keV, representing a significant improvement in intrinsic resolution over the NaI(Tl) detector array discussed in Section 2.3.3. In experiments with the NaI(Tl) detector array, the intrinsic resolution of the NaI(Tl) detectors (ΔE_{int}) was the dominating factor in the total energy resolution (Equation 2.10).

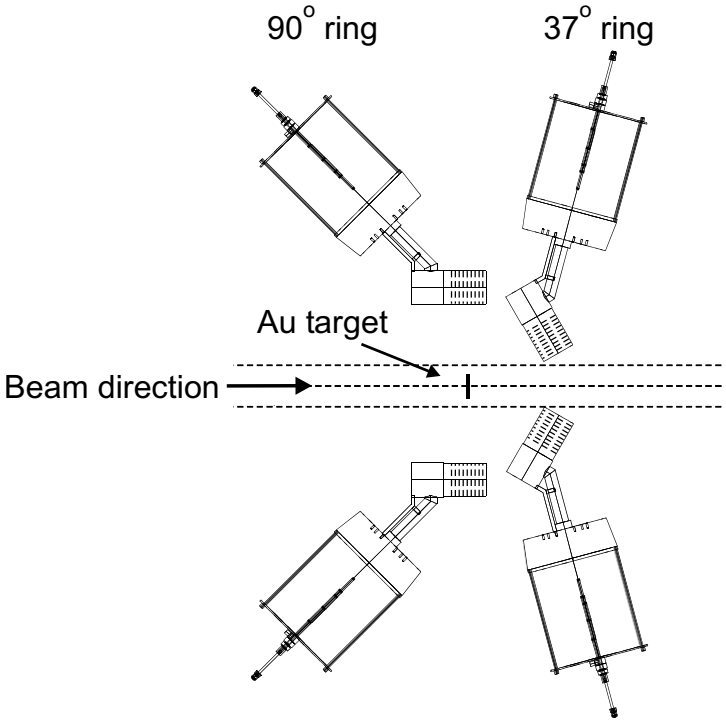

Figure 3.4: Detail of SeGA in the configuration used for the Coulomb excitation experiments performed with the S800 spectrograph. The two 37° and 90° rings of SeGA are named according to the angle of the center of the germanium crystals with respect to the beam direction. The 37° ring can hold up to seven detectors when placed at the entrance to the spectrograph, and the 90° ring can hold up to ten detectors.

With the significantly lowered contribution from the intrinsic resolution of the germanium detectors, it is necessary to lower the contributions from the opening angle of the detectors ($\Delta\theta$) and the uncertainty in the beam energy ($\Delta\beta$) to achieve the best possible experimental energy resolution. To lower the contribution to the energy resolution from ($\Delta\beta$), thinner Coulomb excitation targets must be used with SeGA as compared to those used for Coulomb excitation experiments with the NaI(Tl) array. The segmentation of the SeGA detectors provides a significant improvement in the measurement of the opening angle of the detector array, allowing for a determination of the interaction position of a gamma ray to within 1 cm.

For the present experiment, SeGA was placed at the entrance of the S800 spectrograph. In this configuration, a total of 17 segmented germanium detectors could

be mounted in the array. The detectors were arranged in two rings as shown in Figure 3.4. The rings are denoted as the 37° and 90° rings because the centers of the germanium crystals in each ring are at either 37° or 90° in theta with respect to the beam direction. In the configuration at the entrance to the S800 spectrograph, the 37° ring may contain up to seven detectors. The detector frame can hold up to eight, but one detector cannot be mounted due to the presence of a gate valve. The 90° ring may contain up to 10 detectors. In this experiment, due to problems with several detectors, there were different numbers of detectors for the different secondary beams. For the ^{58,56,55}Ni secondary beams a total of 15 detectors were operational, seven in the 37° ring and eight in the 90° ring. For the ^{54}Ni secondary beam a total of 13 detectors were operational, six in the 37° ring and seven in the 90° ring. All detectors were at a distance of 20 cm from the center of the ^{197}Au target.

Position determination

In order to determine the interaction position of a photon, and thus the emission angle from the target, the position of each segment of each SeGA detector with respect to the target must be known. This requires two measurements: the position of each segment with respect to the detector, and position of each detector with respect to the target. Measurements of the positions of the centers of each segment with respect to the detector cryostat were performed with an automated system [86] which determined the segment positions to an accuracy of less than 0.5 mm (0.28°). The position of each detector with respect to the target is measured for each experimental configuration. For the present experiment, the position of each detector within the detector frame was first measured, followed by the position of each frame location with respect to the target. The three position measurements — segments with respect to detector, detector with respect to frame, and frame with respect to target — were then combined to allow for a determination of the interaction position of a gamma ray to within 1 cm.

The interaction position determination just described assumes that the full energy of the gamma ray is deposited in one interaction with the detector material. This is not the case experimentally, as the gamma ray may undergo Compton scattering or pair production before depositing its full energy. This may cause the full energy of the gamma ray to be shared between multiple segments, and some energy may be lost if the gamma ray scatters out of the crystal. It is then necessary to determine which of the multiple gamma ray events corresponds to the first interaction position of the photon in the crystal from which the angle of the emitted gamma ray can be determined. The following algorithm was used to determine the first interaction position when more than one gamma ray was detected in one SeGA detector for one event trigger. An event trigger was either a down-scaled particle detected at the S800 focal plane or a particle detected at the focal plane in coincidence with a gamma ray detected in SeGA. The segment multiplicity is defined as the number of segments in one SeGA detector registering energies greater than 10 keV for one event trigger. If the segment multiplicity was two, several conditions were used to determine the first interaction position. In software, each SeGA detector was divided into halves. If the two segment events took place in different halves of the detector, the interaction in the half closest to the target was assumed to be the first interaction position. If both segment events took place in the same half of the detector, the highest-energy event was assumed to be the first interaction position if the sum of both events' energies was above 500 keV. If the sum of both events' energies was below 500 keV, the lower-energy event was used to determine the first interaction position. If the segment multiplicity was three or greater, the highest-energy segment event was assumed to be the first interaction position.

Energy and efficiency calibrations

In order to accurately determine the energy of an unknown gamma ray emitted from the de-excitation of a nucleus, the gamma-ray detectors must be calibrated with

standard sources of known gamma-ray energies. The gamma-ray energy calibration of the SeGA detector was carried out with ^{152}Eu and ^{56}Co gamma-ray sources, chosen for their many strong gamma rays covering energies between 122 and 3541 keV. Data werecollected with each source placed at the target position for one hour, and then for each detector each gamma-ray peak was fit with a Gaussian peak shape plus a quadratic background. Spectra for the central contact were analyzed for each detector versus spectra for the individual segments. Experimental information from the detector segments was used only to assign the interaction position. A plot of fit centroid versus actual gamma-ray energy was created for each detector and fit with a second-order polynomial. Calibrated ^{152}Eu and ^{56}Co gamma-ray spectra were then created and examined to check the energy calibrations.

The detector material does not cover the entire space surrounding the Coulomb excitation target, thus not all gamma rays emitted by the projectile and target are detected. To determine the energy of a gamma ray emitted as a result of Coulomb excitation, the number of gamma rays detected is sufficient. As we are also interested in the Coulomb excitation cross section, we must determine the number of gamma rays emitted. Thus we must measure the efficiency, or fraction of the detected gamma rays to the total number of gamma rays emitted, for the detector array. Division of the number of gamma rays detected by the efficiency results in the number of gamma rays emitted.

Unlike the energy calibration, which was performed for each individual detector, the efficiency calibration was performed for each ring of SeGA. The total efficiency of a detector array includes contributions from the efficiency of the detector material, solid angle covered by the detector array, angular distributions of emitted gamma rays due to the reaction mechanism and Lorentz boost, and absorption of gamma rays in the target material. The efficiency for each ring of SeGA detectors must be determined separately due to the difference in angular distributions and target absorption factors. The efficiency calibration was performed with three standard calibration sources,

^{152}Eu, ^{56}Co, and a mixed source containing ^{139}Ce, ^{113}Sn, and ^{137}Cs. While many more gamma rays were detected from the calibration sources, 18 gamma rays were used for the efficiency calibration, covering energies from 165 to 3451 keV. Each source was placed at the target position in the center of SeGA. Data were acquired for two hours for the ^{152}Eu and mixed sources, and one hour for the ^{56}Co source. A summed gamma-ray energy spectrum was created for each of the SeGA rings. For each ring of detectors, each of the 18 gamma-ray photopeaks was then fit to determine the number of counts in the photopeak for each energy. Unlike the Gaussian peak shape used for the energy calibration, the fits to the photopeaks for the efficiency calibration used a Gaussian plus a skewed Gaussian. There was an significant change in the photopeak shape with increasing energy, with a low-energy tail becoming more apparent with increasing photopeak energy (see Figure 3.5). While this didn't affect the energy calibration, an efficiency calibration requires a more accurate determination of the area under the photopeak. A skewed Gaussian was thus added to the photopeak shape to determine the area more accurately. The method used to fit the source photopeaks for the efficiency calibration is discussed in Appendix A. Using the known activity for each standard source and thus the total number of gamma rays emitted, a curve of efficiency versus energy was created for both SeGA rings. This measured efficiency was then compared against the simulated efficiency to determine the scaling factor necessary to adjust the simulated efficiency to the measured value.

The total efficiency was then calculated from the simulated efficiency, scaling factor, calculated angular distributions, and target absorption. Details of the efficiency calculation are discussed in Appendix B. Total efficiencies for the five nuclei studied are listed in Table 3.2.

Simulations

In order to extract the information of interest — energy of the emitted gamma ray and number of de-excitation gamma rays — a good fit to the experimental gamma-ray

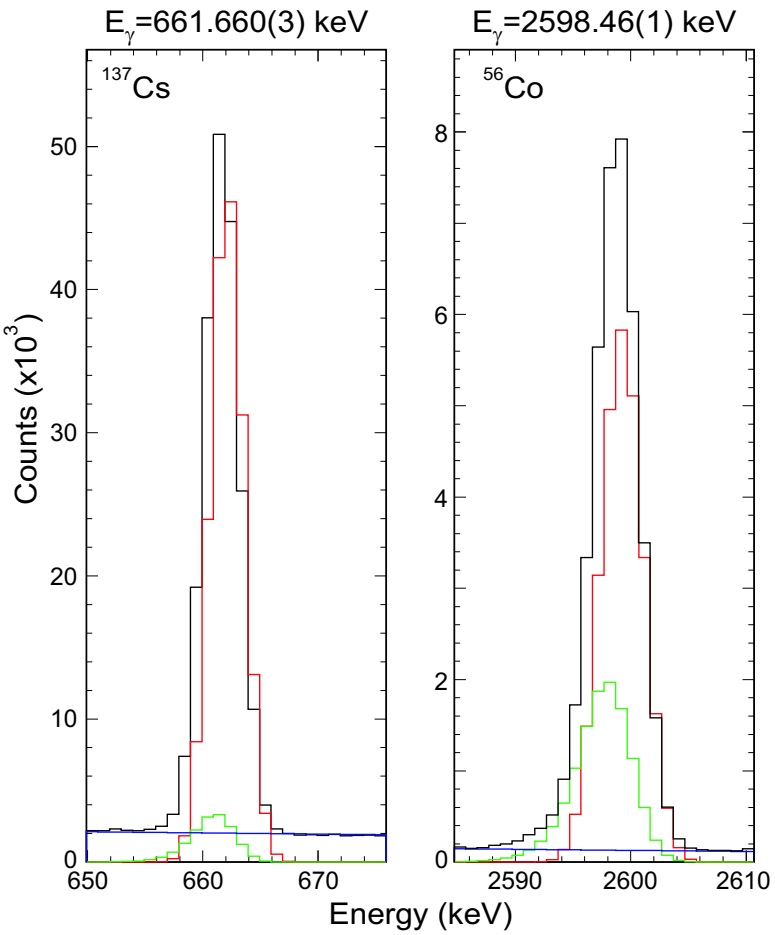

Figure 3.5: Efficiency calibration spectra for the 661.6 keV peak of ^{137}Cs and the 2598.5 keV peak of ^{56}Co. The data are plotted in black, with the Gaussian fit component (red), skewed Gaussian (green) and quadratic background (blue) overlayed. There is an increase in the contribution from the skewed Gaussian in the photopeak as the peak energy increases.

spectrum is necessary. As described in Section 2.3.3, while the photopeak of a gamma ray is correctly transformed to the projectile frame as a result of Doppler reconstruction, other features of the gamma-ray spectrum are smeared after the correction. Thus GEANT simulations were performed for each observed gamma-ray energy and used to fit the experimental spectrum. A Monte Carlo simulation was performed for ten million incident gamma rays at a given energy, isotropically emitted in the projectile frame and Lorentz boosted with the correct beam velocity. The events were then used by the GEANT code to simulate the energy deposited in the detectors. The simulated efficiency using the GEANT code was adjusted in the final analysis to match

Table 3.2: Total SeGA efficiencies (ϵ_{tot}) for the photopeaks of the five nuclei studied. The gamma-ray energies listed are those measured as a result of the present intermediate-energy Coulomb experiment. The sum total efficiency ϵ_{tot}(sum) is equal to $\epsilon_{tot}(37°) + \epsilon_{tot}(90°)$.

Nucleus	E_γ (keV)	$\epsilon_{tot}(37°)$ (%)	$\epsilon_{tot}(90°)$ (%)	ϵ_{tot}(sum) (%)
^{52}Fe	849.0(5)	1.62(12)	1.15(4)	2.77(17)
^{54}Ni	1396(5)	1.18(9)	0.84(7)	2.02(16)
^{55}Ni	2879(10)	0.84(11)	0.51(6)	1.35(16)
^{56}Ni	2695(7)	0.91(12)	0.58(6)	1.49(18)
^{58}Ni	1453(2)	1.45(12)	0.95(7)	2.40(18)

the measured efficiency (see Appendix B). The simulated histograms were fit with analytical curves to determine the area under the simulated photopeak, and thus the simulated efficiency. The analytical curves were then fit to the experimental spectrum. An example of the energy spectra created by GEANT for ten million incident gamma rays at 1454.28 keV is shown in Figure 3.6.

3.3 The test case ^{52}Fe

The $N = Z = 26$ nucleus ^{52}Fe was present in the ^{54}Ni cocktail beam at a greater intensity than the ^{54}Ni beam of interest. The energy of the first excited state of ^{52}Fe ($J^\pi = 2^+$) is well known to be 849.44(10) keV [87]. As over 91 hours of data acquisition time were devoted to ^{54}Ni, a large number of gamma rays in coincidence with ^{52}Fe were detected, providing a good test case for the method used to assign gamma-ray energies. The half-life of the $J^\pi = 2^+$ excited state is not well known, however, with only an adopted lower limit of 0.7 ps [88], and an unknown transition probability $B(E2\uparrow)$. Thus ^{52}Fe was used as a test for our method of gamma-ray analysis, while the more extensively studied ^{58}Ni nucleus was used to test the extraction of $B(E2\uparrow)$ reduced transition probabilities.

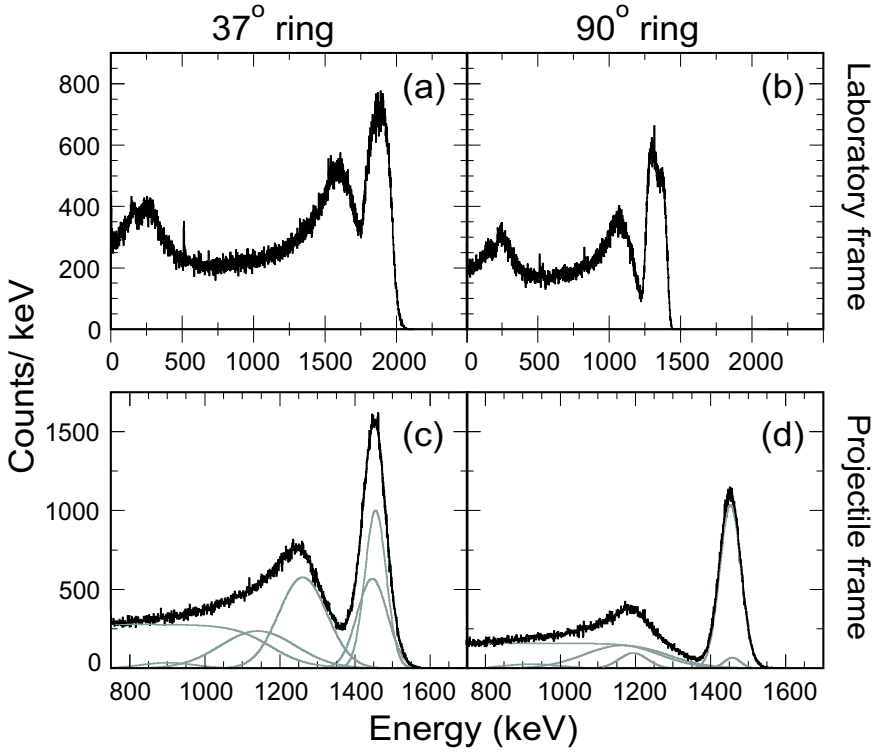

Figure 3.6: Simulated gamma-ray spectra for the 1454.28(10) keV ($2^+ \rightarrow 0^+$) de-excitation gamma ray of ^{58}Ni. 10 million isotropically-emitted gamma rays ($\beta = 0.36$) were simulated and detected by the GEANT program [57] in the two rings of SeGA. The laboratory-frame spectra are shown in (a) and (b), while the projectile-frame spectra with fit components (grey) overlayed are shown in (c) and (d). The plotted sum of the fit components is directly on top of the data points.

3.3.1 Analysis of the gamma-ray spectrum

With the unambiguous identification of ^{52}Fe nuclei in the S800 focal plane (Figure 3.3), the coincident gamma-ray spectra shown in Figure 3.7 were generated. A strong photopeak at approximately 850 keV is apparent in the projectile-frame spectra shown in the left panels of Figure 3.7. This gamma ray corresponds to the de-excitation from the $J^\pi = 2^+$ first excited state to the $J^\pi = 0^+$ ground state of ^{52}Fe. In the laboratory-frame spectra, the 850 keV gamma rays become noticeably broader as a result of the Doppler shift to different energies in the 37° (≈1072 keV) and 90° (≈807 keV) rings of SeGA. As the target and projectile nuclei can both be excited as a result of their interaction, the 547.5 keV gamma ray from the de-excitation from the

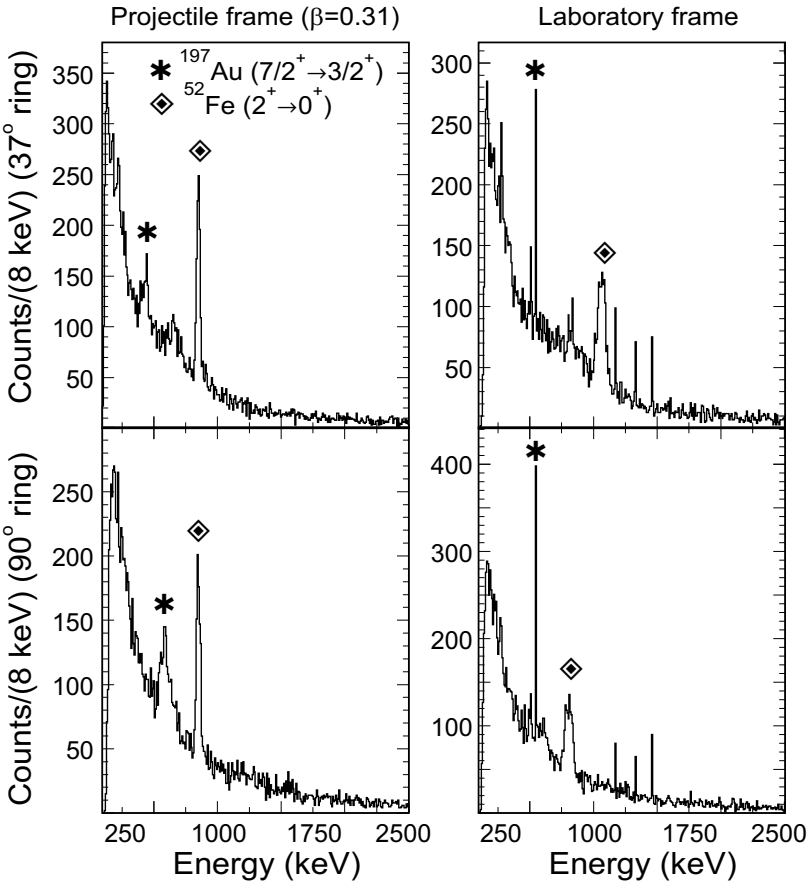

Figure 3.7: Gamma-ray spectra in coincidence with ^{52}Fe particles at the S800 focal plane. The transitions corresponding to de-excitation of the ^{197}Au target and ^{52}Fe projectiles are indicated.

$J^\pi = 7/2^+$ excited state to the $J^\pi = 3/2^+$ ground state of the ^{197}Au target nuclei [89] can be seen as a narrow line in the laboratory-frame spectra. In the projectile-frame spectra, the 547 keV gamma ray broadens and shifts to approximately 433 keV in the 37° and approximately 575 keV in the 90° ring. Due to the loss of projectile velocity in the target ($\Delta\beta \simeq 0.05$), the 849 keV gamma ray associated with ^{52}Fe is not as narrow in the projectile frame as the 547 keV gamma ray associated with ^{197}Au is in the laboratory frame. One can also see three distinct gamma rays between 1000 and 1500 keV in the laboratory-frame spectra. These are background gamma rays at 1173 and 1332 keV from the decay of ^{60}Co and 1408 keV from the decay of ^{40}K. The source of the ^{60}Co gamma rays was a gate valve located just downstream from the SeGA detectors, causing more contamination in the closer 37° ring. The ^{40}K contamination

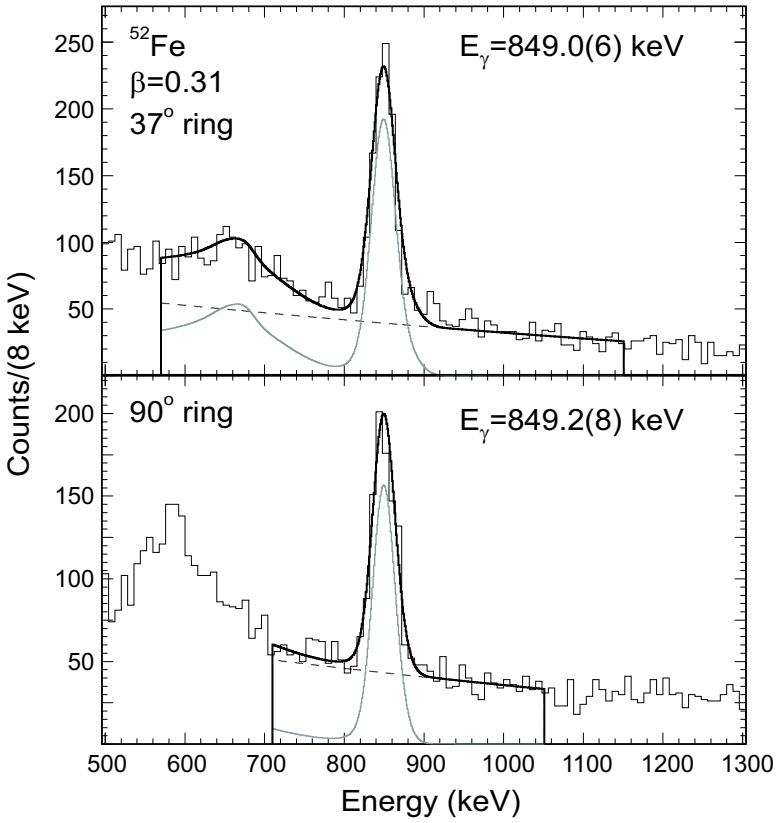

Figure 3.8: Doppler-corrected gamma-ray spectra in coincidence with ^{52}Fe, with fits overlayed. The solid black lines are the total fits to each spectrum, which contain the sum of the simulated response functions (grey lines) and quadratic backgrounds (dashed lines). The gamma-ray energies determined as a result of the fits are 849.0(6) and 849.2(8) keV for the 37° and 90° rings, for a weighted average of 849.1(5) keV.

originated in the walls of the experimental area, affecting both rings equally.

After the projectile-frame spectra were generated, they were fit using the procedure outlined in Section 3.2.3. Simulated projectile-frame spectra were fit with appropriate lineshapes, sums of the individual fit components used to fit the spectra as shown in Figure 3.6. The simulated lineshapes were subsequently scaled to fit to the experimental spectra on top of a quadratic background. For ^{52}Fe, the fitting procedure was performed separately for the two SeGA rings. During the fitting process, the centroid of the lineshape and amount of scaling were varied but the width of the simulated lineshape was fixed. Together with the centroid and area of the simulated photopeak determined from the fit to the simulated spectrum, the shift and scaling of the simulation to the data allowed for a determination of the measured centroid and

Table 3.3: Beam parameters for Coulomb excitation cross section calculations. The maximum laboratory scattering angle θ_{lab}^{max} and minimum impact parameter b_{min} were calculated for at least $d = b_{min} - (r_{tar} + r_{pro}) > 2$ fm, but not exceeding the S800 acceptance of $\pm 3.5°$. The number of beam particles tabulated were measured with no scattering angle restriction.

Secondary beam	Total beam particles	^{197}Au target (mg/cm^2)	θ_{lab}^{max} (degrees)	b_{min} (fm)	d (fm)
^{52}Fe	324752400	257.7	3.5	16.7	4.7
^{54}Ni	21360600	257.7	3.5	16.2	4.2
^{55}Ni	144208800	257.7	3.1	14.1	2.3
^{56}Ni	256621500	184.1	2.9	14.3	2.4
^{58}Ni	115877700	184.1	3.2	13.9	2.0

area of the photopeak. Figure 3.8 shows the fit components and total fit overlayed on the projectile-frame spectra in coincidence with ^{52}Fe nuclei. The weighted average of the centroids for the two rings was 849.1(5) keV, in good agreement with the accepted value of $E_\gamma = 849.43(10)$ keV [87] for the de-excitation of the first excited state of ^{52}Fe.

3.3.2 Excitation cross section and $B(E2; 0^+ \rightarrow 2^+)$

The excitation cross section was determined using Equation 3.27. The number of gamma rays detected (N_γ) was equal to the sum of the area of the two photopeaks from the fits shown in Figure 3.8. The total efficiency (ϵ_{tot}) was the sum of the efficiencies for the two rings, as listed in the last column of Table 3.2. The number of beam particles (N_{beam}) and target thickness ρ are listed in Table 3.3. The total measured cross section (σ_{total}) with these parameters was 243(22) mb. The error on σ_{total} includes contributions from the statistical error on N_γ and N_{beam}, error on the measurement of the ^{197}Au target thickness ρ, and the error on ϵ_{tot}. The error on N_{beam} was less than 1% for all nuclei studied, and the error on ρ was less than 0.5% for both Au targets. The statistical error on the number of detected gamma rays ranged from 2.4% for the large photopeak in coincidence with ^{52}Fe nuclei to 12.5% for the low statistics of ^{54}Ni. The error on the total efficiency was between 6% and

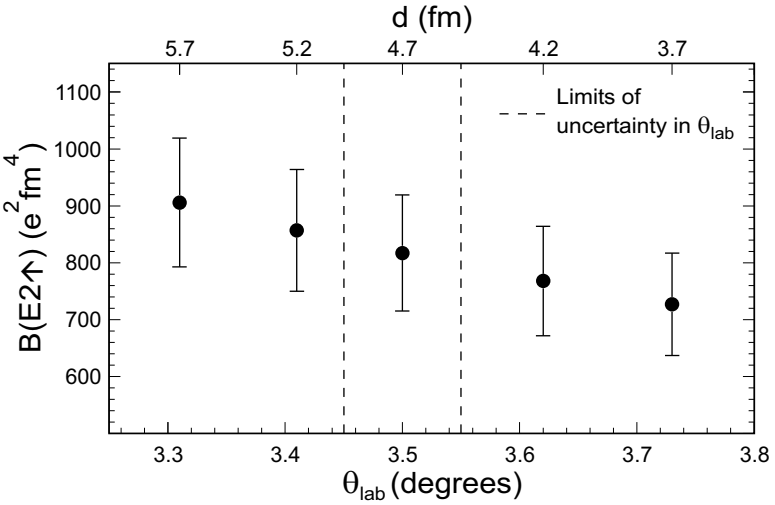

Figure 3.9: $B(E2\uparrow)$ versus laboratory scattering angles for ^{52}Fe. All $B(E2\uparrow)$ were calculated for $\sigma_{\rm CE} = 172(21)$ mb. The corresponding distance between touching spheres (d=b$_{min}$-(r$_{tar}$+r$_{pro}$)) is shown across the top of the figure. The range of uncertainty on the chosen θ_{lab}^{max} of 3.5° is indicated by the dashed lines.

12%, depending on the energy of the de-excitation gamma ray. The calibration sources used to determine the measured efficiency had greater statistics at energies less than 1500 keV, leading to a smaller error on the total efficiency at lower energies. The lower gamma-ray energies measured for ^{52}Fe and ^{54,58}Ni had the lowest error on ϵ_{tot} while the larger errors on ϵ_{tot} affected the results for ^{55,56}Ni.

As discussed in Section 3.1.1, the cross section for Coulomb excitation must include only collisions where the minimum impact parameter b_{min} is greater than 2 fm plus the sum of the projectile and target nuclei. The total cross section $\sigma_{\rm total}$ just determined for the excitation of ^{52}Fe nuclei had no scattering angle restriction, and is thus not the Coulomb excitation cross section that can be used to determine reduced transition probability. The gamma ray spectrum used to determine $\sigma_{\rm total}$ was created for all ^{52}Fe nuclei satisfying the particle identification gates discussed in Section 3.2.2, with no additional restriction on the laboratory scattering angle. Listed in Table 3.3 are the maximum scattering angles θ_{lab}^{max} for all nuclei studied. The S800 spectrograph has acceptances of ±3.5° in the dispersive direction and ±5° in the non-dispersive direction. The θ_{lab}^{max} were calculated for an impact parameter of at least 2 fm plus

the sum of the nuclear radii, not exceeding the maximum acceptance of the S800 spectrograph in the dispersive direction. To calculate the Coulomb excitation cross section $\sigma_{\rm CE}$ for ^{52}Fe, a cut at $\theta_{lab} = 3.5^\circ$ was placed on the laboratory scattering angle. This corresponds to a b_{min} of 16.7 fm, or a distance of 4.7 fm above the sum of the nuclear radii. The laboratory scattering angle is reconstructed from the position of the nuclei measured in the CRDCs of the S800 focal plane as described in Section 2.3.2. The restriction on scattering angle affects both the number of gamma rays and beam particles detected. With a maximum scattering angle of 3.5°, the $\sigma_{\rm CE}$ for ^{52}Fe was measured to be 172(21) mb. The error on $\sigma_{\rm CE}$ includes an additional error of approximately 3% due to the uncertainty in θ_{lab}. The error on the reconstructed laboratory-frame scattering angle is 2 mrad FWHM ($\pm 0.05^\circ$) [54]. An additional error corresponding to the percentage difference in $\sigma_{\rm CE}$ for $\theta_{lab}^{max} - 0.05^\circ$ and $\theta_{lab}^{max} + 0.05^\circ$ was added to the total errors on the measured $\sigma_{\rm CE}$, $B(E2\uparrow)$, and $T_{1/2}$. Measured ^{52}Fe $B(E2\uparrow)$ values for a range of scattering angles around 3.5° is shown in Figure 3.9. The $\sigma_{\rm CE}$ for $\theta_{lab}^{max} = 3.5^\circ$ was used to calculate the $B(E2\uparrow)$. As the ground state spin and parity for ^{52}Fe is 0^+ and the excited state populated in the experiment has a spin and parity of 2^+, according to the angular momentum and parity selection rules for electromagnetic transitions (Equations 3.30 and 3.31) the only transition allowed between the levels is of electric parity and angular momentum $\lambda = 2$. Thus the measured excitation cross section corresponds to a $B(E2; 0^+ \rightarrow 2^+)$ reduced transition probability of 817(102) e^{2}fm^4, and a $T_{1/2}$ for the 2^+ excited state of 7.8(10) ps. These results, along with the measured cross sections, $B(E2\uparrow)$ values and half-lives for all nuclei are listed in Table 3.4.

While a θ_{lab}^{max} of 3.5° was chosen to assure at least 2 fm between the two nuclear radii, it is possible that nuclear excitations may still contribute to the cross section. A calculation for the interaction of ^{52}Fe on ^{197}Au with the Coulomb interaction only, and another with both Coulomb and nuclear interactions allowed was performed [90] using the ECIS88 coupled-channels code [91]. The calculation was performed using

Table 3.4: Gamma-ray energies, cross sections, B(E2↑) values and half-lives from Coulomb excitation measurements. Two possibilities for the unknown J^π of the ^{55}Ni excited state are tabulated assuming pure $E2$ excitation with error adjusted for $M1$ mixing.

Nucleus	$J^\pi_{g.s.}$	J^π_{exc}	E_γ (keV)	σ (mb)	B(E2↑) (e^2fm^4)	$T_{1/2}$
^{52}Fe	0^+	2^+	849.1(5)	172(21)	817(102)	7.8(10) ps
^{54}Ni	0^+	2^+	1396(5)	134(36)	626(169)	0.8(2) ps
^{55}Ni	$7/2^-$	$11/2^-$	2879(10)	57(16)	251(69)	57(16) fs
		$9/2^-$		58(16)	$257(^{-95}_{+73})$	$55(^{-20}_{+16})$ fs
^{56}Ni	0^+	2^+	2695(7)	107(26)	494(119)	40(10) fs
^{58}Ni	0^+	2^+	1453(2)	175(36)	707(145)	612(126) fs

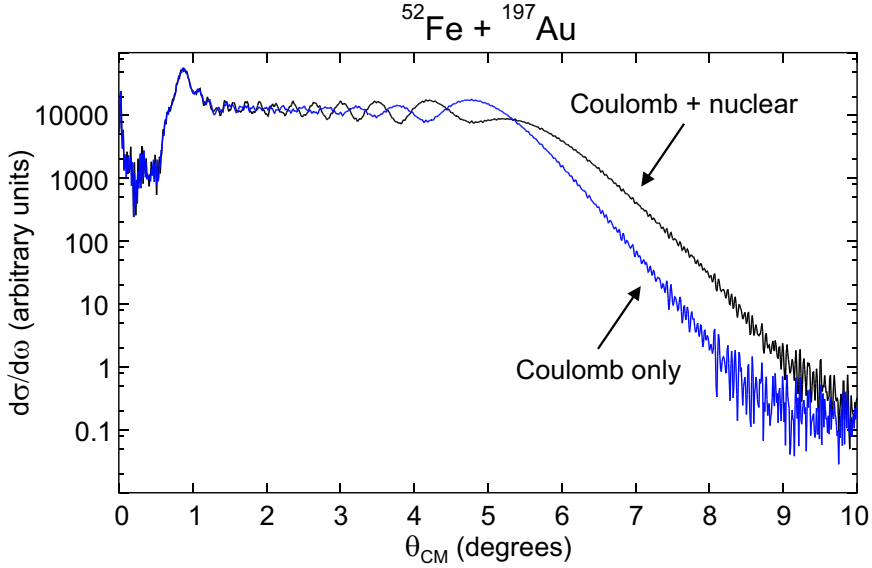

Figure 3.10: ECIS calculation for ^{52}Fe at 56.9 MeV/nucleon. Shown are the excitation cross sections as a function of center-of-mass scattering angle for Coulomb excitation only and Coulomb plus nuclear excitation. Parameters from ^{40}Ar scattering on ^{208}Pb at 41 MeV/nucleon were used in the calculation [92]. The difference between the two curves sets an upper limit of 6% on the nuclear contribution to the cross section.

parameters from ^{40}Ar scattering on ^{208}Pb [92]. The angular distributions for the excitation cross sections calculated by the ECIS program are shown in Figure 3.10. The difference between the two curves sets an upper limit of 6% on the nuclear contribution to the excitation cross section.

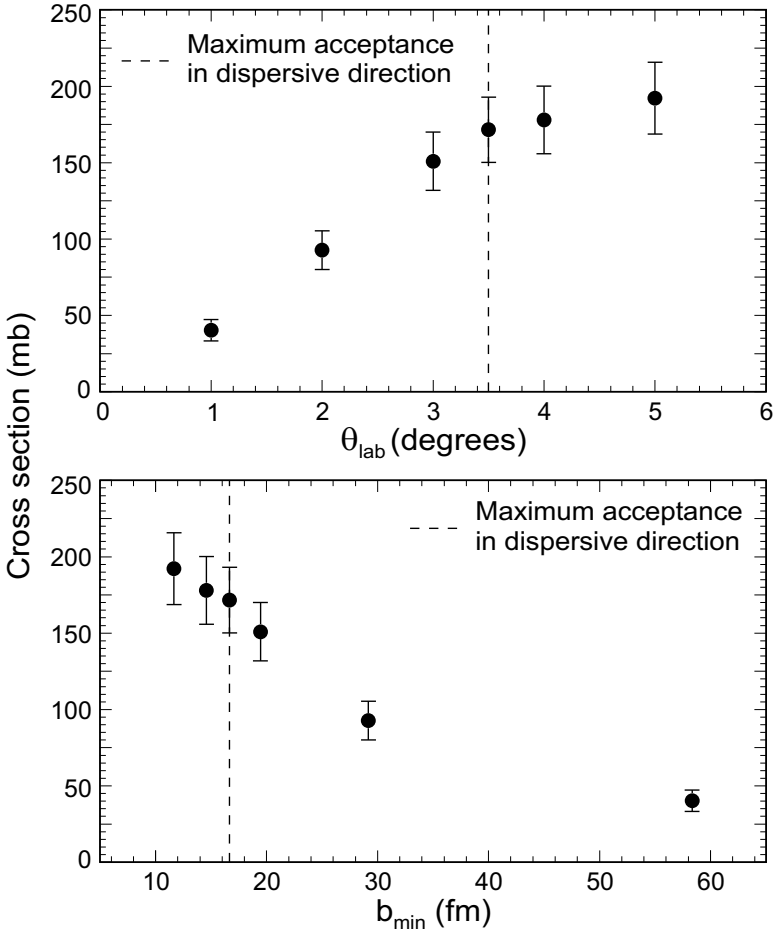

Figure 3.11: Measured cross section versus laboratory scattering angle (top) and minimum impact parameter (bottom) for ^{52}Fe nuclei. For each software cut on laboratory scattering angle, the corresponding gamma-ray spectra and particle spectra were analyzed to yield cross sections. The cross sections measured for 4° and 5° may be low due to the loss of acceptance at 3.5° in the dispersive direction.

3.3.3 CRDC scaling method

While a cut on the appropriate scattering angle to ensure the dominance of Coulomb excitation in the measured cross section was possible for ^{52}Fe, it was not possible for several of the secondary beams studied in this series of experiments. The scattering angle reconstruction depends on the measurement of position at the S800 focal plane in the CRDC detectors. Due to the high beam rate for beams of $A \approx 56$ in this experiment, the efficiency for the CRDC detectors varied from less than 50% for the degraded primary beam of ^{58}Ni to over 90% for the nuclei in the ^{54}Ni cocktail

beam. For the ^{54,55,56}Ni nuclei with few coincident gamma rays, a cut on scattering angle created difficulty in fitting the gamma-ray spectrum and thus determining an excitation cross section. For ^{52}Fe and ^{58}Ni secondary beams, the number of detected gamma rays was sufficient to determine $\sigma_{\rm CE}$ directly with a cut on scattering angle. Thus a method of scaling the measured cross section using the dependence of the ^{52}Fe cross section on laboratory scattering angle was developed to determine the Coulomb excitation cross section for the nuclei for which no scattering angle restriction was possible. This "CRDC scaling method" is discussed below.

Cumulative cuts on θ_{lab}^{max} in steps of 1 degree from 1 to 5 degrees were created for the ^{52}Fe particles. The θ_{lab}^{max} gates were then applied to the particle identification and gamma-ray spectra. N_{beam} and N_γ were determined at each θ_{lab}^{max}, and cross sections were calculated. The cross section for each θ_{lab}^{max} (and associated b_{min}) is shown in Figure 3.11. The cross section with no scattering angle restriction was $\sigma_{\rm total} = 243(22)$ mb. The last cut on θ_{lab}^{max} was 5°, as this is the limit of the S800 acceptance in the non-dispersive direction. The limit of the S800 acceptance in the dispersive direction is 3.5°, thus the cross sections measured between 3.5° and 5° may be unreliable. As shown in Table 3.3, the maximum scattering angles for all nuclei studied were between 2.9° and 3.5°. A second-order polynomial was fit to the points between 2° and 3.5° to allow for interpolation. The cross section measured for $\theta_{lab}^{max} = 1°$ was not used for interpolation due to its low number of coincident gamma rays and thus large percentage error. Using the second-order polynomial, the ^{52}Fe cross section was calculated for each maximum scattering angle $\sigma(\theta_{lab}^{max})$ listed in Table 3.3. A cross section scaling factor S_θ for each θ_{lab}^{max} was determined as $S_\theta = \sigma(\theta_{lab}^{max})/\sigma_{\rm total}$ using the total cross section for ^{52}Fe. Once cross sections with no scattering angle restriction were determined for ^{54,55,56}Ni, multiplication by the appropriate S_θ gave the Coulomb excitation cross section $\sigma_{\rm CE}$. As the accuracy of $\sigma_{\rm CE}$ determined using this "CRDC scaling" method depends on the accuracy to which the ^{52}Fe cross section is measured, an additional percentage error was added to the $\sigma_{\rm CE}$, $B(E2\uparrow)$, and half-

lives measured for ^{54,55,56}Ni. The percentage error on the ^{52}Fe σ_{total} of approximately 3%, which excludes the uncertainties on the SeGA efficiency and θ_{lab}, was included for all nuclei measured using the CRDC scaling method.

3.4 The $B(E2\uparrow)$ test case ^{58}Ni

The degraded primary beam of ^{58}Ni was measured as a test for our method of extracting reduced transition probabilities and half-lives of the excited states. The energy of the first excited ($J^\pi = 2^+$) state of ^{58}Ni is 1454.0(1) keV, with a de-excitation gamma ray of E_γ = 1454.28(10) keV [93]. The adopted $T_{1/2}$ for ^{58}Ni is 667(28) fs, an unweighted average [93] of 740(40) fs from inelastic electron scattering $B(E2\uparrow)$ measurements, 609(15) fs from Coulomb excitation $B(E2\uparrow)$ measurements, 680(60) fs from inelastic photon scattering, and $638(^{-70}_{+98})$ fs from inelastic proton scattering. The adopted $B(E2\uparrow)$ for ^{58}Ni is 695(20) e^{2}fm^4 from an average of several experimental methods [3]. The adopted $B(E2\uparrow)$ from Coulomb excitation measurements only is 708(18) e^{2}fm^4, with a corresponding $T_{1/2}$ of 609(15) fs [93].

3.4.1 Analysis of the gamma-ray spectrum

The gamma rays in coincidence with all ^{58}Ni particles satisfying the particle identification gates are shown in Figure 3.12. The ^{58}Ni-coincident spectra shown are the sum of both rings of SeGA detectors. A photopeak with an energy of approximately 1450 keV can be seen in the projectile-frame spectrum, while in the laboratory-frame spectrum the Doppler broadening renders the 1450 keV photopeak impossible to distinguish from the background. This 1450 keV gamma ray is emitted from the $(2^+ \rightarrow 0^+)$ de-excitation of ^{58}Ni. As was the case for ^{52}Fe, a gamma ray corresponding to the de-excitation of the ^{197}Au target nuclei is apparent in the laboratory frame, and Doppler shifts to two different energies in the summed projectile-frame spectrum. The ^{60}Co and ^{40}K contamination gamma rays are again apparent in the laboratory-

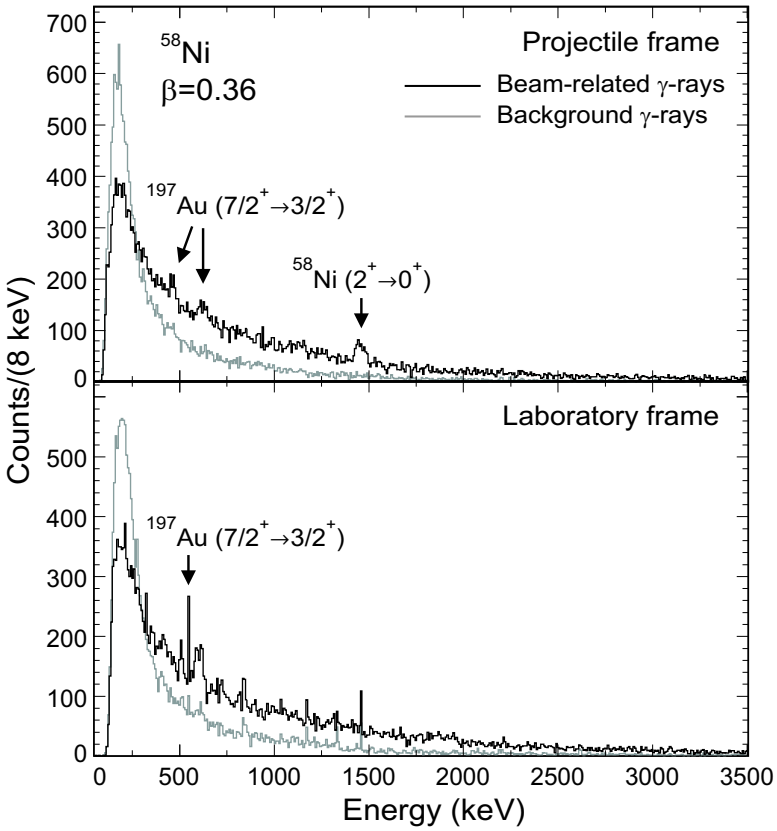

Figure 3.12: Gamma rays in coincidence with ^{58}Ni particles detected at the S800 spectrograph focal plane. Spectra shown are the sum of both SeGA rings. The spectra in black were created with a software gate on the beam-related peak in the time spectrum, while the spectra in grey were created with a software cut of equal time above the beam-related peak.

frame gamma-ray spectrum. The gamma rays from the decay of ^{60}Co and ^{40}K did not interfere with the calculation of N_γ for ^{52}Fe, as the energies of the Doppler-shifted contamination gamma rays were not close to the 849 keV gamma-ray energy from projectile de-excitation. For the ^{58}Ni case, however, the 1332 keV gamma ray from the decay of ^{60}Co was Doppler shifted to 1428 keV in the 90° ring projectile-frame spectrum. The resolution of the 1454 keV gamma rays was such that background contamination at 1428 keV could affect the area under the de-excitation photopeak and thus the experimental cross section. One solution to eliminate the background contamination was to use only the detectors of the 37° ring for data analysis. A larger number of detected photopeak gamma rays provided for a more accurate cross section measurement, however, so it was decided to subtract the stationary gamma-ray

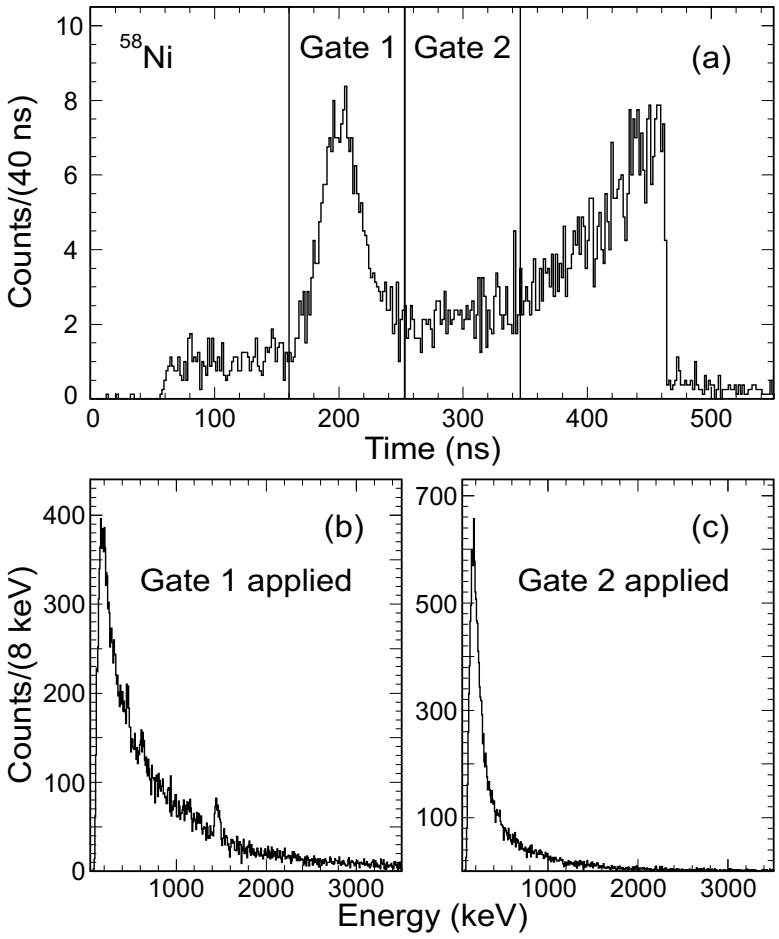

Figure 3.13: A typical ^{58}Ni-coincident time spectrum for one SeGA detector is shown in (a). A peak corresponding to beam-related gamma rays is apparent at approximately 200 ns. Panel (b) is the projectile-frame gamma-ray spectrum with Gate 1 applied, and (c) is the gamma-ray spectrum with Gate 2 applied.

background from the beam-related gamma rays to eliminate the ^{60}Co contamination. The background-subtracted gamma-ray spectra was then analyzed to determine the number of gamma rays in the 1450 keV photopeak.

The background subtraction was performed by placing two software gates on the time spectra for the SeGA detectors. An example of a time spectrum gated on ^{58}Ni for one SeGA detector is shown in Figure 3.13(a). A peak at approximately 200 ns is visible, which corresponds to the gamma rays emitted from the secondary beam's interaction with the ^{197}Au target. These beam-related gamma rays include the gamma rays from the de-excitation of the projectile and the target, as well as beam-related background gamma rays from the fragmentation of the projectile, beam interaction with

experimental apparatus, etc. The counts in the time spectrum below 160 ns and above 260 ns correspond to "stationary" background gamma rays such as those emitted from ^{60}Co and ^{40}K decay. A gate (Gate 1) was placed around the beam-related peak in all operational detectors for all secondary beams. All particle-coincident gamma-ray spectra include a time gate on the beam-related peak in all SeGA detectors as well as the particle identification gates on the particles of interest. While the time gate around the beam-related time peak eliminates much of the stationary background from the coincident gamma-ray spectra, some stationary background gamma rays are still present. To eliminate the remaining stationary background gamma rays in the ^{58}Ni gamma-ray spectra, a second time gate was created (Gate 2) for an equal length of time above the beam-related time gate. The gamma-ray spectrum in coincidence with Gates 1 and 2 are shown in Figures 3.13(b) and (c), respectively. The de-excitation gamma rays from ^{58}Ni and ^{197}Au are present in the spectrum with Gate 1 applied, but absent from the spectrum with Gate 2 applied. By analyzing the gamma-ray spectrum created by subtracting the stationary background gamma-ray spectrum from the beam-related gamma-ray spectrum, it was possible to determine the number of gamma rays in the ^{58}Ni de-excitation photopeak with no contamination from the stationary ^{60}Co background gamma rays. In Figure 3.12, the gamma-ray spectra with the stationary background time cut applied are shown in grey, while the gamma-ray spectra with the beam-related time cut applied are shown in black. The background-subtracted gamma-ray spectra are shown in Figure 3.14.

The background-subtracted projectile-frame spectra for the 37° and 90° rings of SeGA were fit using the same procedure as for ^{52}Fe, as enough coincident gamma rays were detected to analyze the rings separately. The simulated peak shapes were shifted and scaled to fit the data including a quadratic background. The quadratic background is necessary because of the presence of the beam-related background due to interactions of the beam particles with experimental apparatus and de-excitation of contaminant nuclei, which was not subtracted out in the procedure just described.

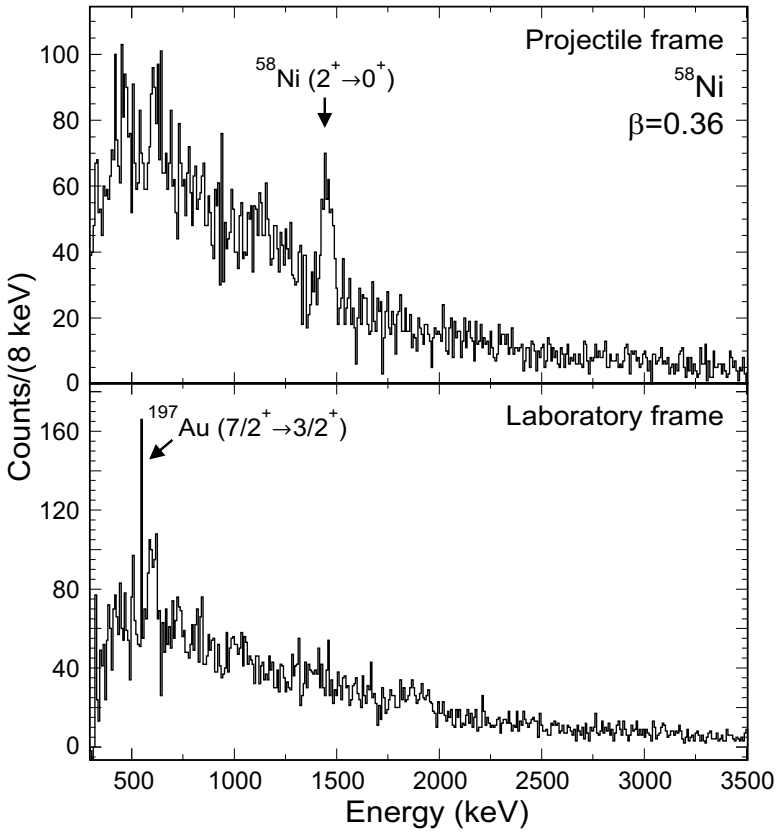

Figure 3.14: Gamma-ray spectra resulting from the subtraction of the stationary-background gamma-ray spectrum from the beam-related gamma-ray spectrum. Spectra were in coincidence with all ^{58}Ni particles detected at the S800 focal plane. The ^{58}Ni de-excitation gamma-ray peak is apparent in the top (projectile frame) panel, while the de-excitation gamma ray from ^{197}Au is apparent in the bottom (laboratory frame) panel.

The gamma-ray spectra for the 37° and 90° rings with fits overlayed are shown in Figure 3.15. As a result of the fits, an energy of the ^{58}Ni ($2^+ \rightarrow 0^+$) de-excitation gamma ray of 1453(2) keV was determined, in agreement with the accepted value of 1454.28(10) keV.

3.4.2 Excitation cross section and $B(E2; 0^+ \rightarrow 2^+)$

The gamma-ray spectra in Figure 3.15 do not have any restriction on laboratory scattering angle. With N_γ as determined from Figure 3.15 and N_{beam} and ρ as listed in Table 3.3, a total cross section σ_{total} of 273(35) mb was measured. The number of detected gamma rays was sufficient to make a cut at $\theta_{lab}^{max} = 3.2°$, resulting in a

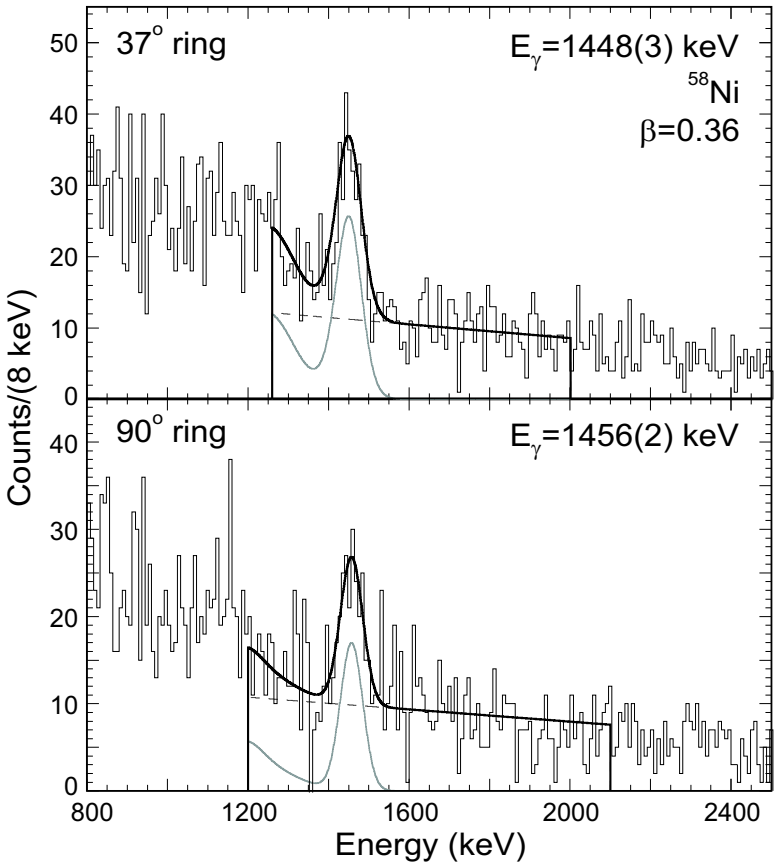

Figure 3.15: Fits of the simulated gamma rays to the projectile-frame gamma-ray spectra in coincidence with ^{58}Ni particles. The solid black lines are the total fits to each spectrum, which contain the sum of the simulated response functions (grey lines) and quadratic backgrounds (dashed lines). The gamma-ray energies determined as a result of the fits are 1448(3) and 1456(2) keV for the 37° and 90° rings, for a weighted average of 1453(2) keV.

Coulomb excitation cross section σ_{CE} of 175(36) mb. This Coulomb excitation cross section corresponds to a $B(E2\uparrow)$ of 707(145) e^{2}fm^4 and a $T_{1/2}$ of 612(126) fs. The measured $B(E2\uparrow)$ and $T_{1/2}$ are in agreement with the adopted values of 695(20) e^{2}fm^4 and 667(28) fs. More importantly, the measured $B(E2\uparrow)$ is in good agreement with the average of all measurements from Coulomb excitation of 708(18) e^{2}fm^4.

As a check of the CRDC scaling method presented in Section 3.3.3, σ_{CE} for ^{58}Ni was calculated using this method. A CRDC scaling factor of $S_\theta = 0.66$ was determined for $\theta_{lab}^{max} = 3.2°$ and multiplied by the total cross section of 273(35) mb. This resulted in a σ_{CE} of 180(34) mb, corresponding to a $B(E2\uparrow)$ of 728(137) e^{2}fm^4. The excitation

cross section and $B(E2\uparrow)$ determined using the CRDC scaling method are in good agreement with those determined with the 3.2° cut on the scattering angle. The error on the $B(E2\uparrow)$ measured using the CRDC cut is larger than that measured with the CRDC scaling method due to the low intensity of the gamma rays in the photopeak with the CRDC cut applied. With the good agreement between the measured σ_{CE} in the two methods, the CRDC scaling method was used to determine the cross sections and $B(E2\uparrow)$ values for the other Ni isotopes.

3.5 The structure of ^{56}Ni

The energy of the first excited state ($J^\pi = 2^+$, $E_\gamma = 2700.6(7)$ keV) of ^{56}Ni is well known [7], as discussed in Section 2.4.2. Several previous measurements exist for the reduced transition probability to the 2^+ first excited state. The Doppler-shift attenuation method (DSAM) was used to measure a $B(E2\uparrow)$ of 385(160) e^2fm^4 [8]. More recently, 600(120) e^2fm^4 was measured via inelastic proton scattering (p,p') [10], and 580(70) e^2fm^4 was measured in an intermediate-energy Coulomb excitation experiment [11]. A shell-model calculation predicted a $B(E2\uparrow)$ of approximately 400 e^2fm^4 [9], which agreed well with the previously-measured value of 385(160) e^2fm^4 from the Doppler-shift attenuation method. The subsequent (p,p') and Coulomb excitation measurements of larger transition probabilities [10, 11] were surprising, and indicated a possible change in the behavior of the radioactive doubly-magic ^{56}Ni nucleus as compared to stable doubly-magic nuclei. Theoretical interest in the region subsequently increased, with multiple theoretical predictions for the $B(E2; 0^+ \rightarrow 2^+)$ transition probabilities [94–96].

3.5.1 Analysis of the gamma-ray spectrum

The gamma-ray spectra in coincidence with all ^{56}Ni particles identified at the S800 focal plane are shown in Figure 3.16. Spectra with both the beam-related time cut and

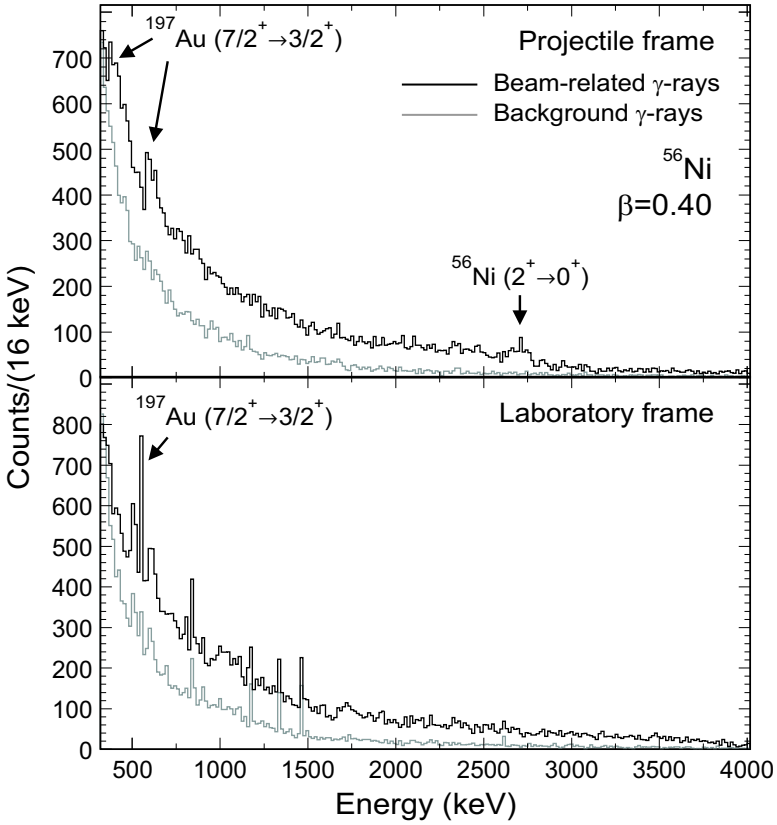

Figure 3.16: Gamma rays in coincidence with ^{56}Ni particles detected at the S800 spectrograph focal plane. Spectra shown are the sum of all SeGA detectors. The gamma rays from the de-excitation of the 2^+ excited state of ^{56}Ni and the $7/2^+$ excited state of ^{197}Au are indicated. The spectra in black were created with a software gate on the beam-related peak in the time spectrum, while the spectra in grey were created with a software cut of equal time on the stationary background gamma rays.

stationary background time cuts are displayed, although no background subtraction was necessary for the ^{56}Ni gamma-ray analysis as the ^{56}Ni de-excitation gamma ray was not contaminated. A gamma ray at approximately 2700 keV corresponding to the de-excitation of the 2^+ excited state of ^{56}Ni is apparent in the projectile-frame spectrum with the beam-related time cut. Although the contamination gamma rays from ^{60}Co and ^{40}K are apparent in the laboratory-frame gamma-ray spectra, the high-energy ^{56}Ni de-excitation gamma ray was not affected.

The method used to fit the projectile-frame gamma-ray spectrum differed from that used for ^{52}Fe and ^{58}Ni due to the lower statistics and higher energy for the ^{56}Ni de-excitation gamma ray. Due to the lower statistics for the 2700 keV gamma ray,

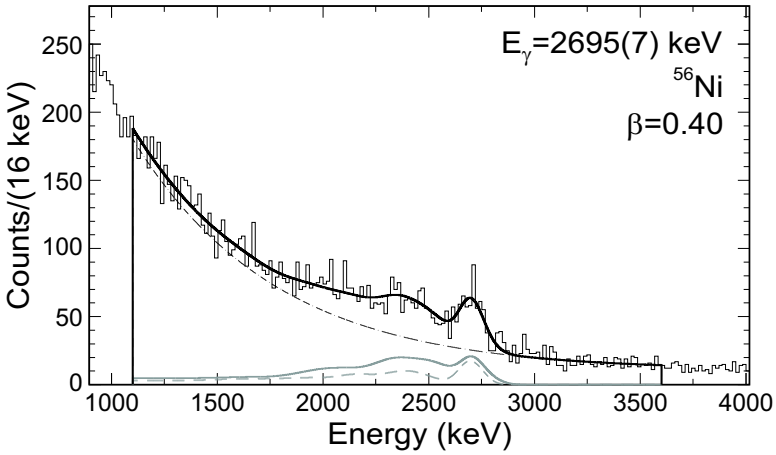

Figure 3.17: The projectile-frame gamma-ray spectrum in coincidence with ^{56}Ni particles with fits overlayed. The spectrum is the sum of both SeGA rings. The solid black line is the total fit containing the sum of the simulated response functions for the individual rings. The solid (dashed) grey lines indicate the contributions from the 37° (90°) rings. The double-exponential background is indicated by the dot-dashed line.

the sum spectrum was fit with the lineshapes from the simulated 37° and 90° rings simultaneously. A double-exponential background was used to model the gamma-ray background at higher energies. One exponential described the background below the 2700 keV photopeak, while a second described the gamma-ray background at energies above 2700 keV. The subsequent fit to the ^{56}Ni-coincident projectile-frame spectrum is shown in Figure 3.17. The centroids of the fits for the 37° and 90° rings of SeGA were 2697(13) and 2694(9) keV, respectively. The weighted average of 2695(7) keV is in agreement with the adopted value of 2701 keV [7].

3.5.2 Excitation cross section and $B(E2; 0^+ \rightarrow 2^+)$

The method of CRDC scaling was used to determine the Coulomb excitation cross section and $B(E2\uparrow)$ for ^{56}Ni. The number of detected gamma rays was determined from the fit shown in Figure 3.17, and resulted in a $\sigma_{\rm total}$ of 178(31) mb with N_{beam} and ρ from Table 3.3. A scaling factor of $S_\theta = 0.60$ was calculated for a θ_{lab}^{max} of 2.9°, and multiplied by the total cross section for a result of $\sigma_{\rm CE} = 107(26)$ mb. With this Coulomb excitation cross section $\sigma_{\rm CE}$, a measured $B(E2\uparrow)$ of 494(119) e^{2}fm^4 and

corresponding $T_{1/2}$ of 40(10) fs were determined.

3.6 The structure of ^{55}Ni

The nucleus ^{55}Ni has not been as extensively studied as ^{52}Fe and ^{56,58}Ni. A spin and parity of $7/2^-$ for the ground state was determined from the measured β-decay strength to ^{55}Co [97, 98]. Particle spectroscopy of the nucleus has identified 20 low-lying levels (including one at 2888(7) keV), but could not assign spins and parities [99]. A more recent experiment using GAMMASPHERE identified four gamma rays from the de-excitation of ^{55}Ni, including one with an energy of 2882 keV which led to the tentative assignment of an excited state at the same energy [100]. A spin and parity of $11/2^-$ for the 2882 keV excited state was tentatively assigned from the angular distribution of the gamma rays. Symmetry of the observed 2882 keV level with that of the $11/2^-$ level in the ground-state band of the mirror nucleus ^{55}Co strengthens the argument for the $11/2^-$ spin assignment [100, 101]. No transition strengths have been measured for ^{55}Ni.

3.6.1 Analysis of the gamma-ray spectrum

The gamma-ray spectra in coincidence with all ^{55}Ni particles satisfying the particle identification gates are shown in Figure 3.18. A gamma ray at approximately 2800 keV is visible in the projectile-frame spectra. Due to the high energy and low intensity of the gamma rays in the photopeak, the gamma-ray spectrum was fit using the same method as for ^{56}Ni. The simulated peak shapes for the two rings were simultaneously fit to the summed projectile-frame spectrum on top of a double-exponential background. The result of the fitting process is shown in Figure 3.19. Gamma-ray energies of 2882(11) and 2868(22) keV were measured for the 37° and 90° rings of SeGA, respectively. The weighted average of 2879(10) keV agrees with the 2882 keV gamma ray measured in the high-spin GAMMASPHERE experiment [100].

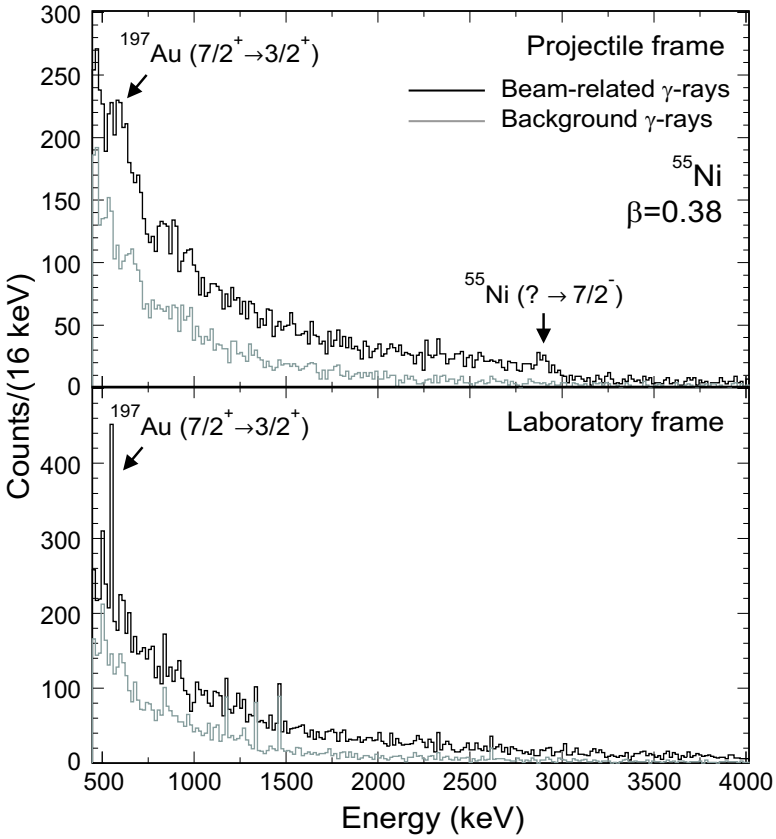

Figure 3.18: Gamma rays in coincidence with ^{55}Ni particles detected at the S800 spectrograph focal plane. The gamma rays from the de-excitation of an excited state of ^{55}Ni are apparent in the top panel at approximately 2800 keV. The spectra in black were created with a software gate on the beam-related peak in the time spectrum, while the spectra in grey were created with a software cut of equal time on the stationary background. Only the ^{197}Au de-excitation gamma rays detected in the 90° ring of SeGA can be seen in the top panel, as the gamma rays are Doppler shifted to approximately 410 keV in the 37° ring.

3.6.2 Excitation cross section and $B(E2; 7/2^- \rightarrow 11/2^-)$

As the spin and parity of the excited state de-populated by the 2879(10) keV gamma ray is unknown, the analysis of the excitation cross section and transition probability differs from that performed for the even-even nuclei previously discussed. It is probable that the excited state at 2879(10) keV populated in the experiment has spin and parity of $11/2^-$, due to the angular momentum measurements and similarity to the mirror nucleus previously stated. If the 2879(10) keV gamma ray measured in this experiment is the result of a $11/2^- \rightarrow 7/2^-$ transition, only an $E2$-type transition is

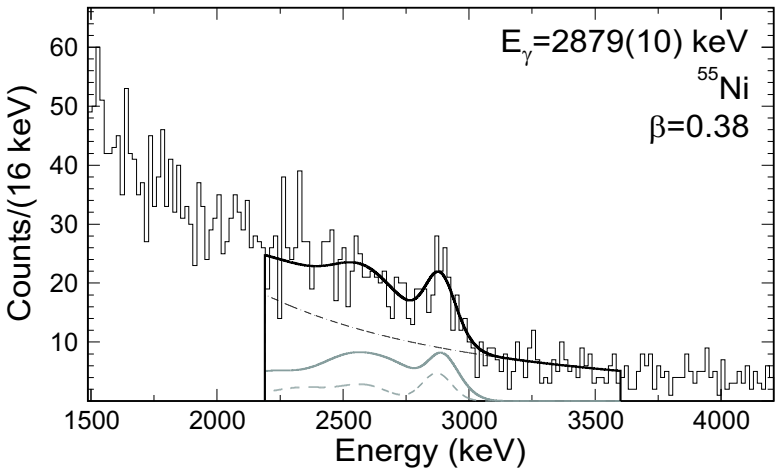

Figure 3.19: The gamma-ray spectrum in coincidence with ^{55}Ni particles for the sum of all SeGA detectors. The solid black line is the total fit which contains the sum of the simulated response functions for the 37° (solid grey line) and 90° (dashed grey line) rings. The double-exponential background is indicated by the dot-dashed line.

probable due to the angular momentum and parity selection rules for electromagnetic transitions. Thus the calculation of excitation cross section and reduced transition probability proceeds as for the previous even-even nuclei. A total cross section of 89(19) mb was calculated using N_γ determined from the fit in Figure 3.19 and the N_{beam} and ρ listed in Table 3.3. Using the CRDC scaling method with a $S_\theta = 0.64$ for $\theta_{lab}^{max} = 3.1°$ results in a σ_{CE} of 57(16) mb. The $B(E2; 7/2^- \rightarrow 11/2^-)$ calculated from this excitation cross section is 251(69) e^{2}fm^4, with a corresponding $T_{1/2}$ of 57(16) fs.

3.6.3 Excitation cross section and $B(E2; 7/2^- \rightarrow 9/2^-)$

If the 2879(10) keV gamma ray measured in this experiment is the result of a $9/2^- \rightarrow 7/2^-$ transition, both $M1$ and $E2$ transitions are most probable. The mixing of the two types of transitions can occur both in the excitation and de-excitation processes. The calculation of $B(\pi\lambda; 7/2^- \rightarrow 9/2^-)$ is dependent on the amount of each type of transition contributing to the excitation to the $9/2^-$ state. In the excitation process, the $E2$ multipolarity transition is expected to dominate. An upper limit of 4.9 mb excitation cross section for pure $M1$ was calculated using the recommended upper limits on $M1$ transition rates [102]. As the measured cross section after CRDC scaling

was approximately 60 mb, at least 92% of the excitation cross section is of type $E2$. The error on the measured $B(E2; 7/2^- \rightarrow 9/2^-)$ was adjusted to account for up to 8% contribution from $M1$ excitation.

For the de-excitation process, the $M1$ transition is expected to dominate due to the shorter lifetime, and thus higher transition rate, for $M1$ de-excitation. The amount of each type of transition is important for the calculation of angular distributions, and thus the calculation of measured total cross section. Using the recommended upper limits on $E2$ and $M1$ transition rates [102], a maximum contribution of 29% from $E2$ de-excitation transitions was calculated. Total cross sections calculated with mixings of 29%, 0%, and 100% $E2$ de-excitation differed by less than 1%. An error of 1% was added to the calculated cross sections and transition probabilities for the $7/2^- \rightarrow 9/2^-$ transition to account for the possibility of error in the $M1$, $E2$ mixing.

The average of the three total cross sections with 29%, 0%, and 100% $E2$ de-excitation was assumed for the total excitation cross section for the $7/2^- \rightarrow 9/2^-$ transition. The CRDC scaling method was used to determine a σ_{CE} of 58(16) mb with $S_\theta = 0.64$ for $\theta_{lab}^{max} = 3.1°$. The reduced transition probability $B(E2; 7/2^- \rightarrow 9/2^-)$ was equal to $257(^{-95}_{+73})$ e^{2}fm^4, with a corresponding $T_{1/2}$ of $55(^{-20}_{+16})$ fs. This represents less than a 2% difference in σ_{CE} and a 2.4% difference in $B(E2\uparrow)$ from the $7/2^- \rightarrow 11/2^-$ transition.

3.7 The structure of ^{54}Ni

While the half-life of the 0^+ ground state of ^{54}Ni has been measured via β-decay [103], no excited states or gamma rays have been measured for this nucleus. The gamma-ray spectra in coincidence with all ^{54}Ni particles satisfying the particle identification gates are shown in Figure 3.20. A gamma ray at approximately 1400 keV is apparent in the projectile-frame spectrum. Symmetry with the mirror nucleus ^{54}Fe, which has an excited level of $J^\pi = 2^+$ at 1408 keV, indicates that the observed gamma ray is

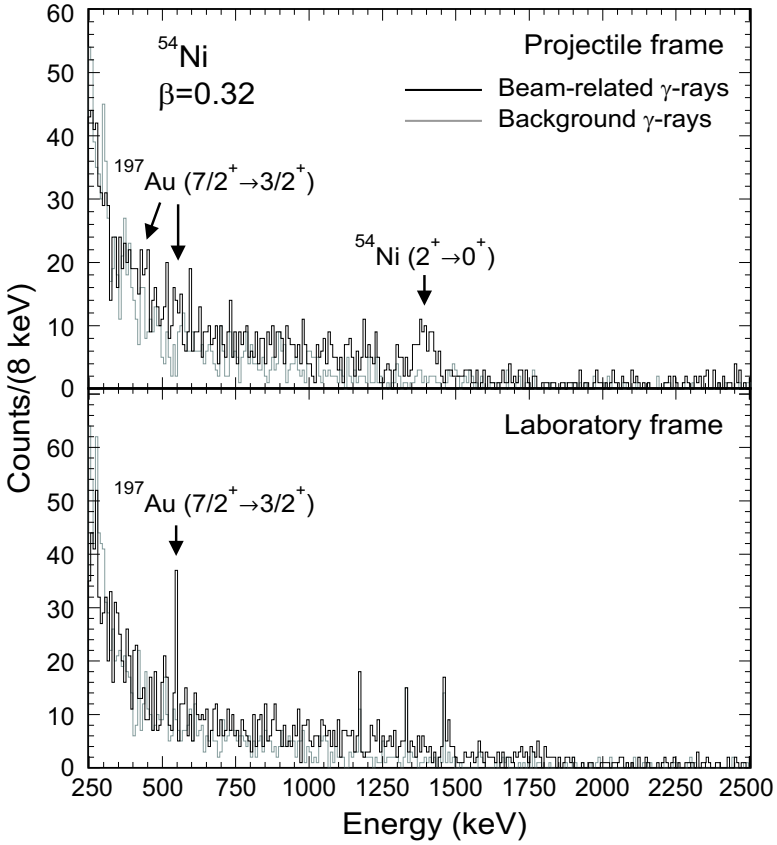

Figure 3.20: Gamma rays in coincidence with ^{54}Ni particles detected at the S800 spectrograph focal plane. The spectra in black were created with a software gate on the beam-related peak in the time spectrum, while the spectra in grey were created with a software cut of equal time on the stationary background. A ^{54}Ni de-excitation gamma ray at approximately 1400 keV is apparent in the top (projectile-frame) panel. The de-excitation gamma rays from the ^{197}Au target nuclei are indicated.

likely to de-excite a state with spin and parity 2^+. Due to the similarity in gamma-ray energy between the gamma ray observed for ^{54}Ni and that for ^{58}Ni, there was again contamination in the 90° ring of SeGA due to the 1332 keV gamma ray emitted from the decay of ^{60}Co. Thus the background-subtraction technique employed for ^{58}Ni was used for ^{54}Ni, with the the background-subtracted spectrum for the sum of all SeGA detectors used for the fit due to low statistics. The background-subtracted projectile-frame spectrum with fits overlayed is shown in Figure 3.21. Due to the low statistics for ^{54}Ni, the background subtraction process resulted in some bins with negative counts. Ten counts were added to all channels in the histogram shown in Figure 3.21 to avoid problems in the fit process due to negative bins in the data histogram. The fits to the

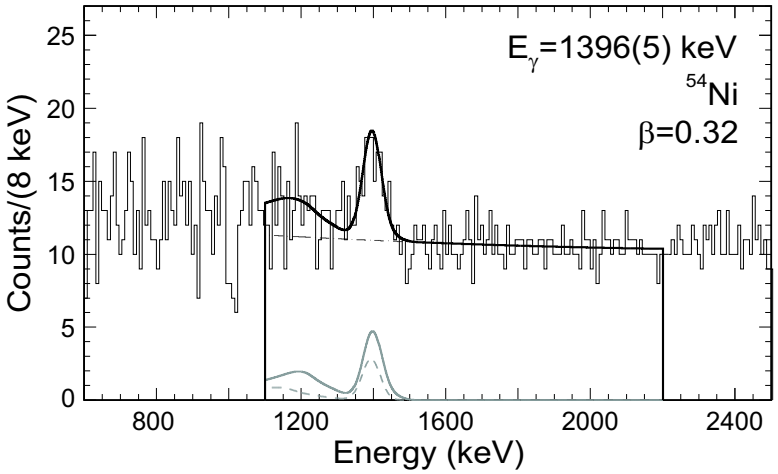

Figure 3.21: The projectile-frame gamma-ray spectrum in coincidence with ^{54}Ni particles. The spectrum is the sum of both SeGA rings, with ten counts added to avoid difficulties associated with negative channels. The solid black line is the total fit, containing the sum of the simulated response functions for the 37° (solid grey line) and 90° (dashed grey line) rings. The quadratic background is indicated by the dot-dashed line.

gamma-ray spectrum resulted in gamma-ray energies of 1397(6) and 1393(7) keV for the 37° and 90° rings, for a weighted average of 1396(5) keV.

A total cross section of 189(40) mb was measured with N_γ determined using the fits from Figure 3.21 and N_{beam} and ρ from Table 3.3. Although the CRDC efficiency was approximately 90% for the secondary beam of ^{54}Ni, the low statistics for the detected gamma rays made it advantageous to use the CRDC scaling method to determine the Coulomb excitation cross section. With an S_θ of 0.74 calculated for $\theta_{lab}^{max} = 4.1°$, an excitation cross section of 134(36) mb was determined. If a spin and parity for the excited state of $J^\pi = 2^+$ is assumed, only $E2$ excitation is possible and a $B(E2; 0^+ \rightarrow 2^+)$ of 626(169) e^{2}fm^4 results. The corresponding half-life for the 1396(5) keV excited state is 0.8(2) ps. This represents the first measurement of gamma rays and transition strengths for the ^{54}Ni nucleus.

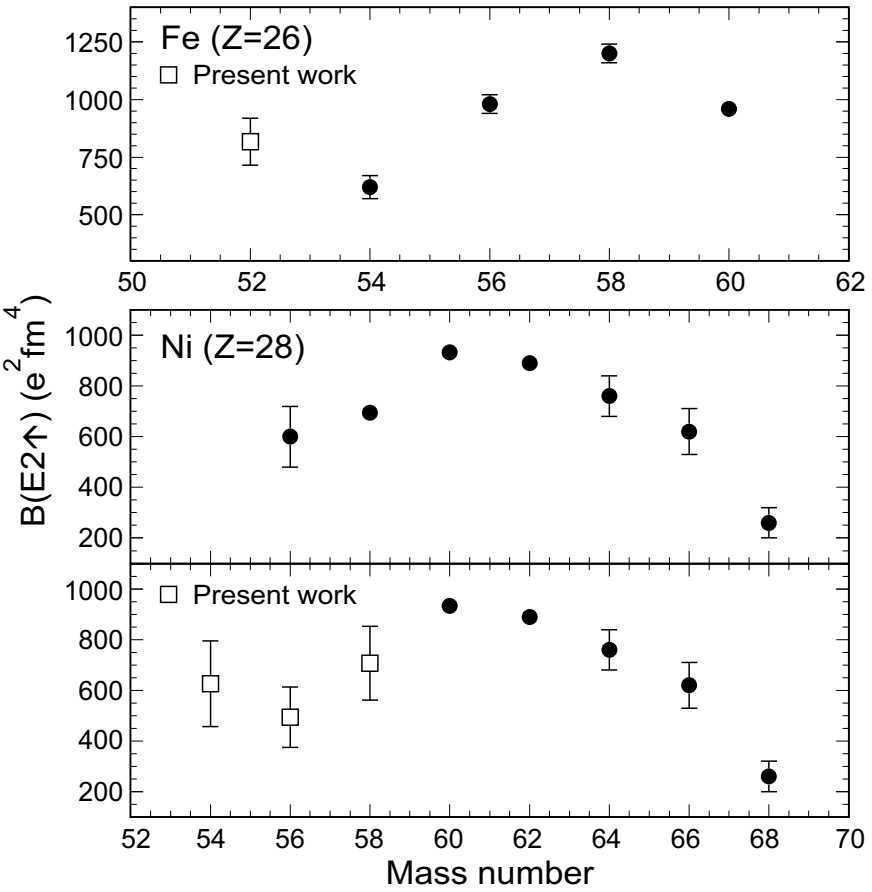

Figure 3.22: Systematic behavior of reduced transition probability $B(E2\uparrow)$ for the even-even Fe and Ni isotopes. The top panel shows the systematics for Fe isotopes with adopted values (filled circles) from [3] and the present measurement for ^{52}Fe (open square). The middle panel shows the adopted $B(E2\uparrow)$ values for the previously-measured Ni isotopes [3]. The lower panel shows the systematics for the known Ni isotopes from $A = 60$ to $A = 68$ [3], with the measured $B(E2\uparrow)$ values from the present work included for ^{54,56,58}Ni.

3.8 Discussion

One of the accepted signatures of magic nuclei is a small $B(E2\uparrow)$ reduced transition probability to the first excited (usually $J^\pi = 2^+$) state. The transition probabilities for doubly-magic nuclei are expected to be especially small. The $B(E2\uparrow)$ systematics for the even-even isotopes of Fe [3] are shown in the top panel of Figure 3.22 with the data point for ^{52}Fe from the present work added. The isotope ^{54}Fe, with 26 protons and 28 neutrons, has the lowest $B(E2\uparrow)$ of the series of isotopes. As 28 neutrons completes a closed shell, this result is expected. The measurement of $B(E2\uparrow) = 817(102)$ e^{2}fm^4

Table 3.5: Theoretical and experimental $B(E2\uparrow)$ reduced transition probabilities. Theoretical values were calculated by Honma and Brown [104] with the MSHELL code [105] and GXPF1 interaction [96]. $B(E2\uparrow)$ values were calculated as described in [106] with A_p and A_n the proton and neutron strength amplitudes. The values in the (A) column were calculated with effective charges $e_p = 1.5e$ and $e_n = 0.5e$, and the values in the (B) column were calculated with effective charges $e_p = 1.3e$ and $e_n = 0.7e$. The truncation was seven for ^{52,54}Fe and ^{54,55}Ni and six for ^{56,57,58}Ni. Adopted values were taken from [3] for all but ^{57}Ni which was taken from [44].

Nucleus	J_i^π	J_f^π	A_p	A_n	$B(E2\uparrow)$ (e^2fm^4) Theory (A)	Theory (B)	Present result	Adopted value
^{52}Fe	0^+	2^+	15.35	15.35	942	942	817(102)	
^{54}Fe	0^+	2^+	14.63	7.13	651	576		620(50)
^{54}Ni	0^+	2^+	7.13	14.63	324	381	626(169)	
^{55}Ni	$7/2^-$	$11/2^-$	19.38	13.23	159	148	251(69)	
		$9/2^-$					$257(^{-95}_{+73})$	
^{56}Ni	0^+	2^+	13.17	13.17	693	693	494(119)	600(120)
^{57}Ni	$3/2^-$	$7/2^-$	13.61	14.53	192	194		201(29)
^{58}Ni	0^+	2^+	9.48	16.87	513	582	707(145)	695(20)

for ^{52}Fe follows the trend as one moves away from a closed shell, as it is higher than that for ^{54}Fe.

A shell-model calculation was performed by Honma and Brown for the nuclei studied in the present experiment [104]. The results are summarized in Table 3.5. The calculation was performed with the conventional shell-model code MSHELL [105] with the GXFP1 interaction [96]. The transition strengths were calculated using

$$B(E2\uparrow) = \frac{(e_p A_p + e_n A_n)^2}{2J_i + 1}, \tag{3.39}$$

where e_p and e_n are the total effective charges of the proton and neutron, and A_p and A_n are the proton and neutron strength amplitudes [106]. The calculations were performed with two different sets of total effective charges. The column labeled (A) in Table 3.5 lists the predictions for $e_p = 1.5e$ and $e_n = 0.5e$, while column (B) lists predictions for $e_p = 1.3e$ and $e_n = 0.7e$. A truncation of seven particles excited out of the $f_{7/2}$ orbit for ^{52,54}Fe and ^{54,55}Ni and six particles excited out of the $f_{7/2}$

orbit for ^{56,57,58}Ni was chosen, as a calculation with the full pf shell would lead to the diagonalization of Hamiltonian matrices with unrealistically large dimensions. Comparison of the ^{52}Fe and ^{54}Fe experimental $B(E2\uparrow)$ values with the theoretical predictions show that the same trend is observed in both experiment and theory. Theory, however, appears to over-predict the increase of the ^{52}Fe $B(E2\uparrow)$ from that of ^{54}Fe.

The adopted $B(E2\uparrow)$ values for the even-even Ni isotopes [3] are shown in the middle panel of Figure 3.22, while in the bottom panel measurements from the present work are included. All Ni isotopes have a magic number of 28 protons, so $B(E2\uparrow)$ values for Ni isotopes should generally be lower than those for Fe isotopes with the same mass number A. ^{56}Ni ($N = 28$) and ^{68}Ni ($N = 40$) also have magic numbers of neutrons. Surprisingly, the transition probability for the $N = Z = 28$ doubly-magic nucleus ^{56}Ni is not as low as that for the $N = 40$, $Z = 28$ nucleus ^{68}Ni.

The doubly-magic nucleus ^{56}Ni has been the subject of theoretical interest since the measurement of $B(E2\uparrow) = 600(120)$ e^{2}fm^4 via proton inelastic scattering [10]. The results of all experimental $B(E2\uparrow)$ measurements and several theoretical predictions are summarized in Figure 3.23. A shell model calculation performed by Nakada, Sebe and Otsuka assuming a closed shell structure for ^{56}Ni predicts a $B(E2\uparrow)$ of approximately 400 e^{2}fm^4 [9]. A calculation with the Shell Model Monte Carlo method and the KB3 interaction with effective charges $e_p = 1.35e$ and $e_n = 0.35e$ predicts a $B(E2\uparrow)$ of 515(40) e^{2}fm^4 [94]. The Monte Carlo Shell Model with the FPD6 interaction calculates 610 e^{2}fm^4 [95]. The measured value from the present work of 494(119) e^{2}fm^4 is in agreement with all calculations except the most recent by Honma and Brown [104]. Comparison with the theoretical predictions in Table 3.5 indicates that the GXPF1 interaction with either choice of total effective charges over-predicts the measured value by a significant amount. The weighted average of all experimental measurements gives $B(E2\uparrow) = 548(51)$ e^{2}fm^4, which is in agreement with the theoretical predictions of Langanke *et al.* [94] and Otsuka *et al.* [95].

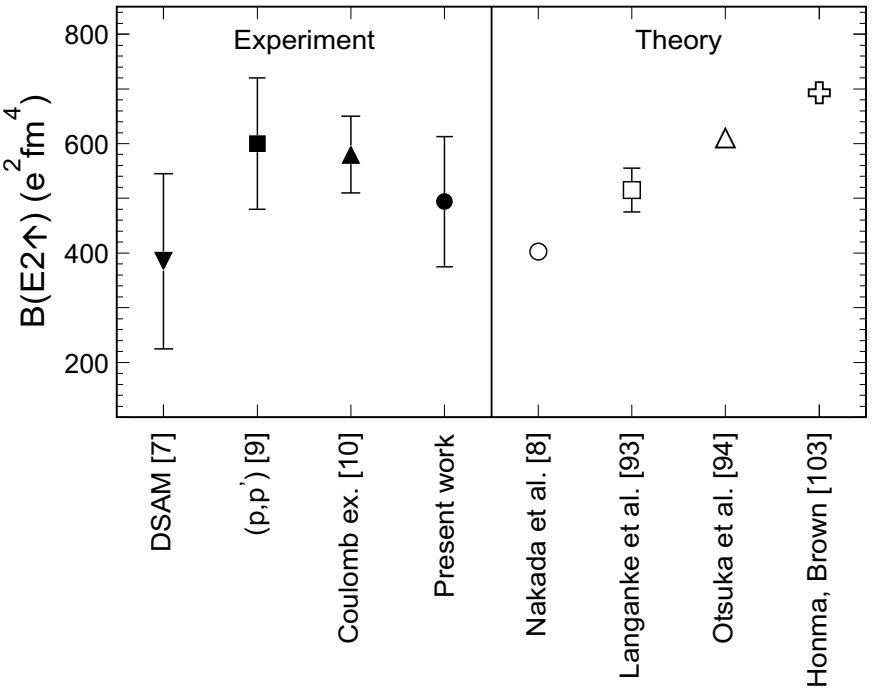

Figure 3.23: Experimental and theoretical $B(E2; 0^+ \rightarrow 2^+)$ results for ^{56}Ni. The weighted average of all experimental measurements is 548(51) e^2fm^4.

The measured $B(E2\uparrow)$ for either excited state spin and parity considered for the ^{55}Ni nucleus is higher than the prediction of Honma and Brown. Two possible explanations for this discrepancy are immediately apparent. If the excited state has spin and parity $J^\pi = 9/2^-$, there may be feeding from higher-lying states distorting the measured transition probability. It is also possible that the measured 2879(10) keV gamma ray could be a doublet of gamma rays very close in energy. The mirror nucleus ^{55}Co, with ground state spin and parity $7/2^-$, has an excited state with $J^\pi = 11/2^-$ at 2973.48(20) keV and another with $J^\pi = 9/2^-$ at 2976.34(19) keV [101]. While a spin of $J = 7/2$ has also been suggested for the higher-energy state, there is stronger evidence for $J^\pi = 9/2^-$. If the gamma ray measured at 2879(10) keV is a doublet with energies less than 5 keV apart, it would appear as one gamma ray with the present experimental conditions, and the measured transition probability would be inaccurate.

The measurement of $B(E2\uparrow) = 626(169)$ e^2fm^4 for the first excited state of ^{54}Ni is significantly higher than those predicted by Honma and Brown (324–381 e^2fm^4)

in the conventional shell model. The increase of $B(E2\uparrow)$ for ^{54}Ni with respect to ^{56}Ni is expected as the $N = 28$ neutron shell is no longer closed in ^{54}Ni. The second prediction of the Honma and Brown calculation, that the $B(E2\uparrow)$ for Ni would be lower than that for the Fe isotope with the same A, does not appear to be fulfilled. The transition probability measured for ^{54}Ni is approximately equal to the adopted value for ^{54}Fe of 620(50) e^2fm^4. A similar $B(E2\uparrow)$ for the two nuclei could be expected, as ^{54}Ni has a magic number of protons but not neutrons, while ^{54}Fe has a magic number of neutrons but not protons. The large error on the $B(E2\uparrow)$ measurement for ^{54}Ni resulting from the low number of detected gamma rays makes it difficult to make any definite conclusions. Even at the lower limit of the present measurement's experimental error, however, the $B(E2\uparrow)$ is 20% above than the higher of the two predictions for ^{54}Ni transition probability listed in Table 3.5.

Chapter 4

Summary

Two experiments have been performed at the NSCL to study nuclear structure in the $N = Z = 28$ region. The first, one-neutron knockout of ^{57}Ni, studied the single-particle structure of the ground state of ^{57}Ni as well as the excited state structure of the ^{56}Ni fragments. The second experiment studied the transition probability to the first excited state of ^{54,55,56,58}Ni and ^{52}Fe via intermediate-energy Coulomb excitation.

The E2 transition strength to the first excited state of ^{56}Ni was measured in 1994 to be 600(120) e^2fm^4 [10], in disagreement with a shell-model prediction of 400 e^2fm^4 [9]. As a result, questions arose about the closed-shell nature at $N = Z = 28$. An experiment to measure the spectroscopic factors for the low-lying states of ^{57}Ni determined that no admixtures from collective ^{56}Ni excited states were present in the wave functions of the ground and first two excited states of ^{57}Ni [50]. To investigate the nature of the $N = Z = 28$ shell closures further, experiments were performed to study both the single-particle structure of ^{57}Ni and the E2 transition strengths to the first excited state of ^{56}Ni and several neighboring neutron-deficient Ni isotopes.

One-neutron knockout of ^{57}Ni was performed using the S800 spectrograph [52] in conjunction with an array of NaI(Tl) detectors [53]. The ^{56}Ni fragments from one-neutron knockout were identified in the spectrograph focal plane [54], while de-excitation gamma rays in coincidence with ^{56}Ni fragments were detected in the

NaI(Tl) array. The spectrograph also provided momentum reconstruction for the detected fragments. Spectroscopic factors of $C^2S = 0.56(11)$ to the ground state and $C^2S = 4.3(3)$ to all excited states were measured for the ground state of ^{57}Ni. These factors exhaust only 56(11)% and 57(4)% of the theoretical predictions for the ground state and all excited states of ^{56}Ni, respectively. This reduction in observed spectroscopic factors is comparable to those observed in knockout reactions for two other well-bound nuclei, ^{16}O and ^{12}C [39]. The reduction of experimental measurements of spectroscopic factors as compared to theory for ^{12}C, ^{16}O and ^{57}Ni are all approximately 50–60%. These reductions measured via nucleon-knockout experiments are in agreement with reductions observed for nuclei from ^{12}C to ^{208}Pb in $(e, e'p)$ experiments [30]. Electron scattering experiments have been considered the standard for measurements of absolute spectroscopic factors. Thus the reductions observed for ^{57}Ni may not be due to excitations of the ^{56}Ni core, but due to experimental inability to measure the short-range part of the nucleon-nucleon interaction. It was possible to assign an angular momentum of $l = 1$ to the distribution associated with ^{56}Ni fragments left in the ground state after neutron knockout. A definite angular momentum assignment for the distribution associated with all excited states of the ^{56}Ni fragments was not possible, though a lower limit of $l = 3$ was suggested. A ^{56}Ni excited state was observed at 5661(72) keV, with de-excitation gamma rays of 1726(10) keV and 3027(71) keV. From the angular momentum selection rules, the possible spins and parities for the 5661 keV state are $J^\pi = 2^+, 3^+, 4^+$ and 5^+. This confirms an excited state at 5668 keV observed in 1985 [59], and rejects the previous tentative angular momentum assignment of $J^\pi = 6^+$.

The intermediate-energy Coulomb excitation measurements were performed using the S800 spectrograph to identify the inelastically-scattered exotic nuclei of interest. The MSU Segmented Germanium Array (SeGA) [65] was used to identify de-excitation gamma rays from the exotic nuclei. A reduced transition probability of $B(E2\uparrow) = 707(145)$ e^{2}fm^4 to the first excited state of ^{58}Ni was measured. This

result is in good agreement with the adopted value of 695(20) e^2fm^4, confirming that our method of extracting transition probabilities is accurate. A transition strength of $B(E2\uparrow) = 817(102)$ e^2fm^4 to the first excited state of ^{52}Fe was measured for the first time. This represents a significant increase over the transition probability to the first excited state of ^{54}Fe, an expected result as ^{54}Fe has a magic number of neutrons. The current measurement of the reduced transition probability for ^{56}Ni ($B(E2\uparrow) = 494(119)$ e^2fm^4) is not as high as the previous measurements from proton inelastic scattering and intermediate-energy Coulomb excitation experiments [10, 11], but agrees with both within experimental errors. A weighted average of 548(51) e^2fm^4 was determined for the three previous measurements [8, 10, 11] and the current measurement of reduced transition probabilities to the first excited state of ^{56}Ni. This value is in agreement with two theoretical predictions [94, 95], but not with a prediction that assumed a closed-shell structure similar to that for the stable isotopes [9].

A gamma ray at 2879(10) keV was observed in coincidence with ^{55}Ni particles. This gamma ray was assumed to de-excite a previously-measured state at 2888(7) keV [99]. The spin and parity of the excited state is unknown, thus transition probabilities were calculated for both $J^\pi = 9/2^-$ and $J^\pi = 11/2^-$. The measured transition strengths to the 2888(7) keV excited state with either spin and parity was significantly higher than that calculated in the shell model using the GXFP1 interaction [104]. It is possible that the de-excitation gamma ray measured in coincidence with ^{55}Ni could be an unresolved doublet. If one gamma ray was indeed measured, a $J^\pi = 9/2^-$ excited state with feeding from unobserved higher states could also explain the higher measured transition probability.

The energy of the first excited state of ^{54}Ni and the transition strength to that state were measured for the first time. The energy, at 1396(5) keV, is in agreement with the energy of the first excited state of the mirror nucleus ^{54}Fe. The reduced transition probability to the 1396(5) keV state was measured to be 626(169) e^2fm^4, higher than predicted by a shell-model calculation [104]. While the shell-model calculation

predicted the transition probability for ^{54}Ni to be lower than that for ^{56}Ni, the opposite trend was observed. This places the transition probabilities for the ^{54}Ni and ^{54}Fe mirror nuclei at approximately the same value. The increase of transition probability for ^{54}Ni with respect to ^{56}Ni reinforces the doubly-magic status of the ^{56}Ni nucleus, although the disagreement between shell-model predictions and measured reduced transition probabilities for ^{56}Ni still casts doubt on the strength of the $N = Z = 28$ shell closure.

Appendix A

Fit Method for Efficiency Calibrations

A.1 Determination of fit parameters

An accurate measurement of the efficiency for a detectors requires a careful determination of the number of counts detected. For a measurement of efficiency for a gamma-ray detector, the photopeak corresponding to each gamma-ray energy must be fit with a peak shape that describes the photopeak as accurately as possible. Thus the error on the number of counts detected and the measured efficiency is reduced. In experiments with NaI(Tl) detector arrays a Gaussian peak shape was sufficient to describe the photopeak. For the gamma rays detected in SeGA, a low-energy tail was observed that increased in magnitude with gamma-ray energy (See Figure 3.5) making it necessary to use a more complicated function to describe the photopeak.

The functional form F based on the fit function used in the program GF3 [107]

$$\begin{aligned} F &= G + S \\ G &= A\left(1 - \frac{R}{100}\right) \exp\left(-\frac{1}{2}\left(\frac{x - x_o}{\sigma}\right)^2\right) \\ S &= A\left(\frac{R}{100}\right) \exp\left(\frac{x - x_o}{\beta}\right) \operatorname{erfc}\left(\frac{x - x_o}{\sqrt{2}\sigma} + \frac{\sigma}{\sqrt{2}\beta}\right) \end{aligned} \tag{A.1}$$

provided a good description of the photopeaks. The total peak shape (F) includes two components, a normal Gaussian (G) and a skewed Gaussian (S). The parameter A is the height of the Gaussian, x_o is the centroid of the Gaussian, R is a measure of the percentage of the skewed Gaussian in the total peak area, σ is the Gaussian width, and β is the skew width.

In order to understand the dependence of the Gaussian skew parameters with energy it was necessary to parameterize σ, R, and β. A choice of $\beta = \sigma$ allowed the parameterization process to proceed most efficiently. R and σ were parameterized simultaneously after the choice of β. With $\beta = \sigma$, the source gamma rays were fit with the form given in Equation A.1, with σ and R allowed to vary freely. Plots of σ versus energy and R versus energy were created and fit with first-order polynomials. Thus σ and R in Equation A.1 were replaced by $\sigma = \sigma_1 x + \sigma_2$ and $R = R_1 x + R_2$. All gamma-ray energies from 165 to 3451 keV were used to parameterize σ, while only those above 600 keV were used for the R parameterization as the intensity of the skew was not apparent below gamma-ray energies of 600 keV. The inclusion of the lower-energy gamma rays produced an unreliable result for R.

Once the parameterization of σ and R was complete for both SeGA rings, all gamma rays from the source peaks were fit to determine the number of counts in the photopeak. Fits were performed with the form of Equation A.1 using the PAW program [108], with σ_1, σ_2, R_1, R_2 fixed to the parameters previously determined, and $\beta = \sigma$. Programs used for the fit process are presented in the next section. The area under the photopeak (N_F) for each gamma ray was determined by creating a

vector for both fit components in Equation A.1, and summing the elements of the vector. The error on the area of the photopeak was determined in a similar manner, by creating a vector from the error components. The error on the area (ΔN_F) is equal to

$$
\begin{aligned}
\Delta N_F^2 &= \Delta N_G^2 + \Delta N_S^2 \\
\Delta N_G^2 &= \left[\left(1-\frac{R}{100}\right)\sum_x \exp\left(-\frac{1}{2}\left(\frac{x-x_o}{\sigma}\right)^2\right)\right]^2 \Delta A^2 \\
&\quad + \left[-\frac{A}{100}\sum_x \exp\left(-\frac{1}{2}\left(\frac{x-x_o}{\sigma}\right)^2\right)\right]^2 \left[x_o^2\Delta R_1^2 + R_1^2\Delta x_o^2 + \Delta R_2^2\right] \\
&\quad + \left[A\left(1-\frac{R}{100}\right)\sum_x \frac{x-x_o}{\sigma^2} \exp\left(-\frac{1}{2}\left(\frac{x-x_o}{\sigma}\right)^2\right)\right]^2 \Delta x_o^2 \\
&\quad + \left[A\left(1-\frac{R}{100}\right)\sum_x \frac{(x-x_o)^2}{\sigma^3} \exp\left(-\frac{1}{2}\left(\frac{x-x_o}{\sigma}\right)^2\right)\right]^2 \\
&\qquad \times \left[x_o^2\Delta\sigma_1^2 + \sigma_1^2\Delta x_o^2 + \Delta\sigma_2^2\right] \\
\Delta N_S^2 &= \left[\frac{R}{100}\sum_x \exp\left(\frac{x-x_o}{\sigma}\right) \operatorname{erfc}\left(\frac{x-x_o}{\sqrt{2}\sigma}+\frac{1}{\sqrt{2}}\right)\right]^2 \Delta A^2 \\
&\quad + \left[\frac{A}{100}\sum_x \exp\left(\frac{x-x_o}{\sigma}\right) \operatorname{erfc}\left(\frac{x-x_o}{\sqrt{2}\sigma}+\frac{1}{\sqrt{2}}\right)\right]^2 \\
&\qquad \times \left[x_o^2\Delta R_1^2 + R_1^2\Delta x_o^2 + \Delta R_2^2\right] \\
&\quad + \left[\frac{AR}{100}\sum_x \left[\frac{1}{\sigma}\sqrt{\frac{2}{\pi}} \exp\left(\frac{x-x_o}{\sigma}\right) \exp\left(-\left(\frac{x-x_o}{\sqrt{2}\sigma}+\frac{1}{\sqrt{2}}\right)^2\right)\right.\right. \\
&\qquad \left.\left. -\frac{1}{\sigma} \exp\left(\frac{x-x_o}{\sigma}\right) \operatorname{erfc}\left(\frac{x-x_o}{\sqrt{2}\sigma}+\frac{1}{\sqrt{2}}\right)\right]\right]^2 \Delta x_o^2 \\
&\quad + \left[\frac{AR}{100}\sum_x \frac{x-x_o}{\sigma^2} \exp\left(\frac{x-x_o}{\sigma}\right)\left[\sqrt{\frac{2}{\pi}} \exp\left(-\left(\frac{x-x_o}{\sqrt{2}\sigma}+\frac{1}{\sqrt{2}}\right)^2\right)\right.\right. \\
&\qquad \left.\left. - \operatorname{erfc}\left(\frac{x-x_o}{\sqrt{2}\sigma}+\frac{1}{\sqrt{2}}\right)\right]\right]^2 \left[x_o^2\Delta\sigma_1^2 + \sigma_1^2\Delta x_o^2 + \Delta\sigma_2^2\right]. \qquad \text{(A.2)}
\end{aligned}
$$

It should be noted that Equation A.2 is valid only if $\beta = \sigma$.

A.2 Fit programs for efficiency calibration

The source gamma rays were fit in PAW using the macro `efit.kumac` and fortran function `gelifit.for` presented below. A histogram file containing the histograms to be fit must be opened in PAW prior to running the macro. The macro allows for a fit of one source peak at a time, to the spectrum contained in the histogram number `hid`. The energy range `xpl1` and `xpl2` in which the peak will be displayed such that one can choose limits for the fit and an initial guess for the centroid must be specified. The area under the photopeak and associated error are output to the screen, and the fit components are plotted overlayed on the data histogram. The fortran file `gelifit.for` is called by the macro.[1]

```
MACRO efit hid=2037 xpl1=100 xpl2=4000
* This macro fits one peak with the gelifit function type, for
* use in efficiency calibration. The area and error on the area
* under the photopeak is calculated. The data histogram with
* the two fit components is drawn followed by the residue (data-fit).
* A vector (p) of length 12 is created
* (1) height of peak (Ao)
* (2) position of peak (xo)
* (3-5) background parameters (a,b,c) p(3)+p(4)*x+p(5)*x^2
* (6-7) gaussian width (sigma) parameters: sigma = p(6)*xo + p(7)
* (8-9) skew width (beta) parameters: beta = p(8)*sigma + p(9)
* (10-11) skew intensity (R) parameters: R = p(10)*xo + p(11)
* (12) height of low energy step function
* p(12) and p(9) are always set to zero
* Errors on the fit parameters are in vector ep(12).
```

[1] In the macro as displayed here, there are several lines that begin with Z followed by several spaces. The code on these lines should be an extension of the previous line. For formatting here it was necessary to separate the lines, but if run in PAW the two lines must be joined and the Z eliminated.

```
* Arguments when calling the macro are the histogram number
* on which the fit will be performed and the limits to use for
* plotting.

*Call the fortran file that has the fitting function
call gelifit.for

* Options for plots
opt nstat
zon 1 1
set pmci 2
set hcol 2
set mtyp 29

* Plot the histogram with the limits given as arguments
h/pl [hid]([xpl1]:[xpl2]) HIST

* create the vector of fit parameters (p) and errors (ep)
VE/crea p(12)
V/CR ep(12) r 12*0.0

MESSAGE Please click on lower bound, upper bound, and centroid:
VLOCATE X Y
x1=$EVAL(X(1))
x2=$EVAL(X(2))
xc=$EVAL(X(3))

* Calculate intital estimates and limits for the parameters:
```

```
    V/CR hist($HINFO([hid],'XBINS')) r
    H/GET/CONT [hid] hist
* Initial guess for background is linear:
    dx = $EVAL(($HINFO([hid],'XMAX')+1
Z        -$HINFO([hid],'XMIN'))/$HINFO([hid],'XBINS'))
    y1 = $EVAL(HIST(INT([x1]+1)))
    y2 = $EVAL(HIST(INT([x2]+1)))
    yc = $EVAL(HIST(INT([xc]+1)))
    V/IN p(3) $eval(([x2]*[y1]-[x1]*[y2])/([x2]-[x1]))
    V/IN p(4) $eval(([y2]-[y1])/([x2]-[x1]))
    V/IN p(5) 0.0
* Initial guess for Gaussian height and centroid:
    V/IN p(1) $eval([yc]-([y1]+[y2])/2)
    V/IN p(2) $eval([xc])

* set Gaussian width parameters p(6-7)
* set skew width p(8-9) and intensity parameters p(10-11)
* separately for the different SeGA rings
if ([hid].eq.2037) then
   ve/in p(6) .0001936
   ve/in p(7) 1.382
   ve/in p(8) 1.0
   ve/in p(9) 0.0
   ve/in p(10) .011888
   ve/in p(11) 10.506
endif
if ([hid].eq.2090) then
   ve/in p(6) .00020567
```

```
   ve/in p(7) 1.31
   ve/in p(8) 1.0
   ve/in p(9) 0.0
   ve/in p(10) .016184
   ve/in p(11) 5.1855
endif

* step function is always eliminated
ve/in p(12) 0

* Set default minimum and maximum limits for
* all fit parameters to be +- 95%
sigma minp=0.05*p
sigma maxp=1.95*p
* Set specific limits for some parameters
V/IN minp(2) $eval(p(2)-3)
V/IN maxp(2) $eval(p(2)+3)
V/IN minp(5) -0.1
V/IN maxp(5)  0.1

* perform the fit, fixing sigma,R and the step height
* the gefitparam function is used, found in the file
* gelifit.for
    application HMINUIT exit
      fix 6,7,8,9,10,11,12
      minimize 3500
    exit
    histogram/fit [hid]([x1]:[x2]) gefitparam B,M 12 P ! MINP MAXP EP
```

```
* plot the histogram with fit
h/pl [hid]([xpl1]:[xpl2])

* calculate the area under the photopeak by
* creating vectors for the Gaussian, skew, and background
* and using VSUM to sum the different components.
* The vectors are also used to plot the different components.
* Calculate the error on the area via the same vector-sum method.
* Calculate vectors for all error components, sum vectors,
* add in quadrature with the appropriate parameter errors.
* The vector ep contains the errors from the fit, plus the errors
* on the fixed parameters (added into the vector below).
* ep(1) = delta A
* ep(2) = delta xo
* ep(3-5) = errors on background (not used)
* ep(6) = delta sigma1
* ep(7) = delta sigma2
* ep(8-9) = errors on beta (none)
* ep(10) = delta R1
* ep(11) = delta R2
* ep(12) = error on step (none)

* Vectors on sigma and R coefficients
if ([hid].eq.2037) then
 if (ep(6).eq.0) then
   ve/in ep(6) .0000042192
   ve/in ep(7) .0040199
```

```
 endif
 if (ep(10).eq.0) then
   ve/in ep(10) .0010579
   ve/in ep(11) 3.0765
 endif
endif
if ([hid].eq.2090) then
   ve/in ep(6) .0000095497
   ve/in ep(7) .021927
   ve/in ep(10) .00095670
   ve/in ep(11) 1.5677
endif

* create x-vector with the appropriate range, to calculate
* vectors for area and error.
sigma low = x(1) - 200
sigma high = x(2) + 200
ve/crea nch(1) I $sigma((high-low+1)*10)
ve/crea xvec($eval(nch))
sigma j=1
DO i=low,high
   sigma xi = [i]
   v/in xvec($eval(j)) xi
   sigma j = j + 1
enddo

* calculate area and error.
* NOTE: This calculation is done with beta=sigma. If
```

```
* beta does not equal sigma, the error formula must be
* corrected.
APPLICATION sigma
  sig = p(6) * p(2) + p(7)
  R = p(10) * p(2) + p(11)
  A = p(1)
  xo = p(2)
  dsig = sqrt(xo**2*ep(6)**2 + p(6)**2*ep(2)**2 + ep(7)**2)
  dR = sqrt(xo**2*ep(10)**2 + p(10)**2*ep(2)**2 + ep(11)**2)
  xdrv = array(8192,1#8192)
  bdrv = p(3) + p(4)*xdrv + p(5)*xdrv**2
  gdrv = A*(1-R/100)*exp(-0.5*((xdrv-xo)/sig)**2)
  sdrv = A*(R/100)*exp((xdrv-xo)/sig)
  sdrv = sdrv*erfc((xdrv-xo)/(sqrt(2)*sig)+sig/(sqrt(2)*sig))
  bkgdv = p(3) + p(4)*xvec + p(5)*xvec**2
  gausv = A*(1-R/100)*exp(-0.5*((xvec-xo)/sig)**2)
  skewv = A*(R/100)*exp((xvec-xo)/sig)
  skewv = skewv*erfc((xvec-xo)/(sqrt(2)*sig)+sig/(sqrt(2)*sig))
  vdg1 = (1-R/100)*exp(-0.5*((xvec-xo)/sig)**2)
  vdg2 = -(A/100)*exp(-0.5*((xvec-xo)/sig)**2)
  vdg3 = A*(1-R/100)*((xvec-xo)/sig**2)*exp(-0.5*((xvec-xo)/sig)**2)
  vdg4 = A*(1-R/100)*((xvec-xo)**2/sig**3)
  vdg4 = vdg4*exp(-0.5*((xvec-xo)/sig)**2)
  vds1 = (R/100)*exp((xvec-xo)/sig)
  vds1 = vds1*erfc(((xvec-xo)/(sqrt(2)*sig))+(1/sqrt(2)))
  vds2 = (A/100)*exp((xvec-xo)/sig)
  vds2 = vds2*erfc(((xvec-xo)/(sqrt(2)*sig))+(1/sqrt(2)))
  vds3 = (A*R)/100*(1/sig)*sqrt(2/3.141592654)*exp((xvec-xo)/sig)
```

```
  vds3 = vds3*exp(-(((xvec-xo)/(sqrt(2)*sig))+(1/sqrt(2)))**2)
  vds3 = vds3 - (A*R)/100*(1/sig)*exp((xvec-xo)/sig)*
Z        erfc(((xvec-xo)/(sqrt(2)*sig))+(1/sqrt(2)))
  vds4i = (A*R*(xvec-xo))/(100*sig**2)*sqrt(2/3.141592654)
  vds4=vds4*exp((xvec-xo)/sig-((xvec-xo)/(sqrt(2)*sig)+1/sqrt(2))**2)
  vds4 = vds4i - (A*R*(xvec-xo))/(100*sig**2)*exp((xvec-xo)/sig)*
Z        erfc(((xvec-xo)/(sqrt(2)*sig))+(1/sqrt(2)))
exit

* Sum up the vectors to get the photopeak area Ntsv
ve/crea Ngsv(1) ! $sigma(vsum(gausv))
ve/crea Nssv(1) ! $sigma(vsum(skewv))
sigma Ntsv = Ngsv + Nssv

* Sum up the vectors to get the error on the area vdat
ve/crea tdg1(1) ! $sigma(vsum(vdg1))
ve/crea tdg2(1) ! $sigma(vsum(vdg2))
ve/crea tdg3(1) ! $sigma(vsum(vdg3))
ve/crea tdg4(1) ! $sigma(vsum(vdg4))
ve/crea tds1(1) ! $sigma(vsum(vds1))
ve/crea tds2(1) ! $sigma(vsum(vds2))
ve/crea tds3(1) ! $sigma(vsum(vds3))
ve/crea tds4(1) ! $sigma(vsum(vds4))
sigma vdgt = sqrt(tdg1**2*ep(1)**2 + tdg2**2*dR**2
Z            + tdg3**2*ep(2)**2 + tdg4**2*dsig**2)
sigma vdst = sqrt(tds1**2*ep(1)**2 + tds2**2*dR**2
Z            + tds3**2*ep(2)**2 + tds4**2*dsig**2)
sigma vdat = sqrt(vdgt**2 + vdst**2)
```

```
MESSAGE The area under the peak is $eval(Ntsv) counts
MESSAGE with error $eval(vdat) counts

* plot Gaussian, skew, and background fit components
set hcol 1
ve/draw gdrv ! S
set hcol 3
ve/draw sdrv ! S
set hcol 5
ve/draw bdrv ! S

MESSAGE Enter to proceed to residue
wait

* plot the residue
set dmod 1
set hcol 2
hi/pl [hid]([xpl1].:[xpl2].) func
v/create fvec(8192)
get_vect/func [hid] fvec
h/copy [hid] 5000
put_vec/con 5000 fvec
sub [hid] 5000 5001
zon 1 2
h/pl [hid]([x1]:[x2])
h/pl 5001([x1]:[x2])
zon 1 1
```

```
return
```

This fortran function allows for a fit of the entire GF3 function, which includes a step function in addition to the Gaussian and skewed Gaussian in Equation A.1. During the efficiency calculations for the intermediate-energy Coulomb excitation experiments the step function was always set to zero.

```
      FUNCTION gelifit()
      gelifit = 0
      return
      END

      FUNCTION gefitparam(x)
      COMMON /PAWPAR/ P(12)
      REAL gefit,x,a,b,c,Ao,xo,sigma,beta,R,H
      REAL photo,skew,step,bg

C     Map parameter list to function variables:
      Ao = p(1)
      xo = p(2)
      a = p(3)
      b = p(4)
      c = p(5)
      sigma = p(6)*xo + p(7)
      beta  = p(8)*sigma + p(9)
      R = p(10)*xo + p(11)
      H = p(12)
```

```
      if ( R.le.0) then
         R = 0
      endif
      if ( sigma.ne.0. ) then
         photo = Ao*(1-R/100.)*exp(-0.5*((x-xo)/sigma)**2)
         step  = Ao*(H/100.)*(1/2)*erfcc((x-xo)/(1.414213562*sigma))
         if ( beta.ne.0. ) then
            skew  = Ao*(R/100)*exp((x-xo)/beta)*
     *           erfcc((x-xo)/(1.414213562*sigma)+
     *           sigma/(1.414213562*beta))
         else
            skew = 0.
         endif
      else
         photo = 0.
         step  = 0.
         skew  = 0.
      endif
      bg    = a+b*x+c*x**2
      gefitparam = photo + skew + step + bg

      return
      END

      FUNCTION erfcc(x)
      REAL erffc
      REAL x,t,z
C     This function returns the value of the complementary
```

```
C     error function at x by means of the Chebyshev fitting
C     method (accurate to x=1.2e-7). From Numerical Recipes
C     in FORTRAN by Press, Teukolsky, etc.
      z=abs(x)
      t=1./(1.+0.5*z)
      erfcc=t*exp(-z*z-1.26551223+t*(1.00002368+t*(.37409196+t*
     *     (.09678418+t*(-.18628806+t*(.27886807+t*(-1.13520398+t*
     *     (1.48851587+t*(-.82215223+t*.17087277)))))))))
      if (x.lt.0.) erfcc=2.-erfcc
      return
      END
```

Appendix B

Efficiency of SeGA using GEANT simulations

The cross section for Coulomb excitation is

$$\sigma = \frac{N_\gamma}{\epsilon_{tot} \times N_{beam} \times N_{target}}. \tag{B.1}$$

The total efficiency (ϵ_{tot}) includes contributions from the detector efficiency, solid angle covered by the detector array, angular distributions of emitted gamma rays due to the reaction mechanism and Lorentz boost, and absorption of gamma rays in the target material. The efficiency for a general detector array including angular distributions is discussed first, followed by the specific derivation of the total efficiency of SeGA using GEANT simulations.

The efficiency of a detector array for an isotropic, non-Lorentz boosted source is

$$\epsilon(E_\gamma)^{iso} = \frac{1}{4\pi} \int_\Omega \epsilon(E_\gamma, \theta, \phi)\, d\Omega, \tag{B.2}$$

where

$$\epsilon(E_\gamma, \theta, \phi) = \frac{\#\text{ of gamma rays detected at } \theta, \phi}{\#\text{ emitted at } \theta, \phi} \tag{B.3}$$

is the efficiency of an infinitesimal theta and phi. The total efficiency over the detector solid angle $\epsilon(E_\gamma)^{iso}$ is measured in an efficiency calibration with a standard gamma-ray source. As integral, not infinitesimal, quantities are experimentally measured, $\epsilon(E_\gamma, \theta, \phi)$ is never directly measured.

In intermediate-energy Coulomb excitation, the incoming beam particles are traveling with a velocity of 30–50% the speed of light. Thus a distinction between quantities measured in the laboratory (lab) frame and those measured in the frame of the incoming projectile (pro) is necessary. The efficiency for a gamma ray described by Equation B.2 will be the same in the laboratory and projectile frames only if the gamma ray is emitted from a stationary source in the laboratory frame, i.e. for a calibration measurement where the gamma rays are emitted from a standard source placed at a fixed position near the detector. For an intermediate-energy Coulomb excitation experiment, different efficiencies will be measured in the laboratory and projectile frames due to the Doppler shift of the gamma-ray energy (E_γ) for a moving gamma-ray source. The frame in which measurements and calculations are performed will be indicated by the labels pro and lab.

If the reaction mechanism that produces the detected gamma rays has a non-isotropic angular distribution, such as that due to the alignment of the initial m-substates for Coulomb excitation, the efficiency of the detector array must be folded with the angular distribution $W(\theta)$. In the projectile frame, ϵ_{tot} in Equation B.1 becomes [83]

$$\epsilon_{tot,pro} = \frac{\int_{\Omega_{pro}} W(\theta_{pro})\, \epsilon(E_\gamma^{pro}, \theta_{pro}, \phi_{pro})\, d\Omega_{pro}}{\int_{4\pi} W(\theta_{pro})\, d\Omega_{pro}}. \tag{B.4}$$

If a normalized angular distribution such that

$$\int_{4\pi} W(\theta_{pro})\, d\Omega_{pro} = 1 \tag{B.5}$$

is assumed, then Equation B.4 reduces to

$$\epsilon_{tot,pro} = \int_{\Omega_{pro}} W(\theta_{pro})\, \epsilon(E_{\gamma}^{pro}, \theta_{pro}, \phi_{pro})\, d\Omega_{pro}. \tag{B.6}$$

If the detector efficiency is isotropic over Ω_{pro}, $\epsilon(E_{\gamma}^{pro}, \theta_{pro}, \phi_{pro})$ can be replaced by the measured efficiency in Equation B.2, with the result

$$\epsilon_{tot,pro} = \epsilon(E_{\gamma}^{pro})^{iso} \times \frac{\int_{\Omega_{pro}} W(\theta_{pro})\, d\Omega_{pro}}{\frac{1}{4\pi}\int_{\Omega_{pro}} d\Omega_{pro}}. \tag{B.7}$$

Total efficiency calculations for intermediate-energy Coulomb excitation have been conventionally performed in the laboratory frame [56, 83]. If intermediate-energy beams are used, the angular distribution of emitted gamma rays will change due to the Lorentz boost, affecting the efficiency at different solid angles. The efficiency calibration performed with a standard gamma-ray source results in an efficiency curve from which the measured efficiency at the Doppler-boosted gamma-ray energy E_{γ}^{lab} is determined[1]. In order to integrate over the angular distribution due to the reaction mechanism $W(\theta_{pro})$ in the laboratory frame, the Lorentz boost must be included, resulting in a new angular distribution $W(\theta_{lab})^{boosted}$

$$W(\theta_{lab})^{boosted} = W(\theta_{pro})\, \frac{d\Omega_{pro}}{d\Omega_{lab}}, \tag{B.8}$$

where θ_{pro} is related the laboratory frame angle θ_{lab} by

$$\cos(\theta_{pro}) = \frac{\cos(\theta_{lab}) - \beta}{1 - \beta\cos(\theta_{lab})} \tag{B.9}$$

[1]Most detector arrays cover a range of angles, and thus a range in E_{γ}^{lab}. Consideration of the change in efficiency for different E_{γ}^{lab} must be given when calculating the measured efficiency in the laboratory frame. The use of GEANT simulations to determine the measured efficiency for SeGA eliminates the need for such calculations, thus they are omitted here.

and the quantity $d\Omega_{pro}/d\Omega_{lab}$ is defined as

$$\frac{d\Omega_{pro}}{d\Omega_{lab}} = \frac{1-\beta^2}{(\beta\cos\theta_{pro}-1)^2}. \tag{B.10}$$

The superscript 'boosted' indicates that the Lorentz boost is included in the quantity $W(\theta_{lab})$. The integral over the solid angle is also performed in the laboratory frame. Thus, from Equation B.7 the conventional laboratory-frame calculation for the total efficiency becomes

$$\epsilon_{tot} = \epsilon(E_\gamma^{lab})^{iso} \times \frac{\int_{\Omega_{lab}} W(\theta_{lab})^{boosted} d\Omega_{lab}}{\frac{1}{4\pi}\int_{\Omega_{lab}} d\Omega_{lab}}. \tag{B.11}$$

In experiments with SeGA, GEANT simulations are performed from which measured efficiencies are determined. This requires a slightly different approach than that used to achieve Equation B.11. The measured efficiency for the gamma ray of interest $\epsilon(E_\gamma^{lab})^{iso}$ is now determined from the GEANT-simulated efficiency for that gamma ray multiplied by a scaling factor. As in Equation B.11, the measured efficiency is determined in the laboratory frame. The GEANT simulation is performed with a Lorentz-boosted, isotropic distribution of emitted gamma rays. The gamma rays are detected with the appropriate energy and efficiency for the angle at which they interact with SeGA. Ideally, one would fit the Doppler-broadened laboratory-frame gamma-ray spectrum to get the number of gamma rays detected and thus the simulated efficiency, but in many cases the laboratory frame spectrum is difficult to fit. The number of gamma rays is the same in the laboratory frame and projectile frame spectra, thus the simulated projectile-frame gamma-ray spectrum is fit in order to determine the simulated efficiency

$$\epsilon(E_\gamma^{lab})^{iso,boosted} = \frac{\#\text{ of counts in simulated spectrum}}{\#\text{ of GEANT triggers}}. \tag{B.12}$$

In order to determine the measured efficiency, it is necessary to correct the simulated efficiency for some deviation from the efficiency measured with standard gamma-ray calibration sources. To correct the simulated laboratory-frame efficiency, a factor δ_{GEANT} must be multiplied by $\epsilon(E_\gamma^{lab})^{iso,boosted}$ in the calculation of ϵ_{tot}. This factor is determined by minimizing the difference between the measured efficiency at the energies of the source gamma rays used and the simulated efficiency at the same energies, such that

$$\sum_{\text{source energies}} (\epsilon_{\text{measured}} - \delta_{\text{GEANT}} \times \epsilon_{\text{GEANT}}) \simeq 0. \tag{B.13}$$

During the minimization process, the factor δ_{GEANT} is allowed to vary. This factor, once determined, is multiplied by the simulated efficiency to determine the measured efficiency of the gamma ray of interest.

The angular distribution due to the reaction mechanism $W(\theta_{pro})$ must now be calculated excluding the Lorentz boost, as the Lorentz boost is included in the simulated efficiency. Using Equation B.8, the total efficiency is now

$$\epsilon_{tot} = \epsilon(E_\gamma^{lab})^{iso,boosted} \times \delta_{\text{GEANT}} \times \frac{\int_{\Omega_{pro}} W(\theta_{pro})\, d\Omega_{pro}}{\frac{1}{4\pi}\int_{\Omega_{pro}} d\Omega_{pro}}, \tag{B.14}$$

The integral over Ω_{pro} is carried out over the angles θ_{pro} and ϕ_{pro}. Due to the non-continuous nature of SeGA, integrals over both angles should be completed taking into account the opening angle of the detectors in θ_{pro} and the granular nature of the ϕ_{pro} angular coverage. As the efficiency calculations are carried out separately for the two rings of SeGA, θ_{pro} for each ring covers a continuous range. While the integral over phi is not continuous, it is possible to cancel the ϕ_{pro} contributions in

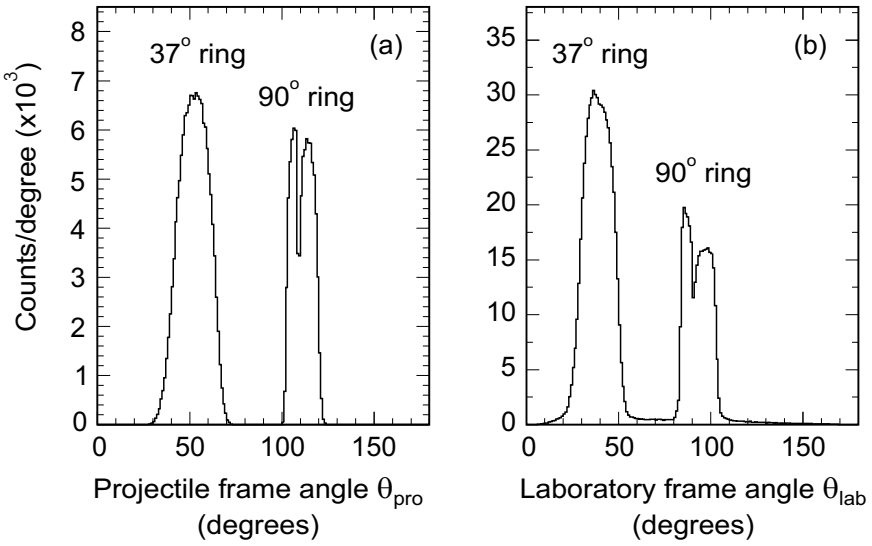

Figure B.1: Theta angles of simulated photons emitted and subsequently detected in the two rings of SeGA. Simulations were performed for 10 million 849 keV gamma rays from the de-excitation of ^{52}Fe at $\beta = 0.36$. Angles of detected photons in the projectile frame, gated on the photopeak of the simulated gamma ray in the projectile frame, are shown in panel (a). Angles of detected photons in the laboratory frame, ungated, are shown in panel (b). A clear distinction between theta angles corresponding to those photons detected in the 37° and 90° rings is apparent. Also apparent at approximately 90° in the laboratory frame and approximately 110° in the projectile frame is the effect on the detection of gamma rays due to the target absorption.

Equation B.14 as $W(\theta)$ is independent of ϕ. Thus only the integral over θ_{pro} remains:

$$\epsilon_{tot} = \epsilon(E_\gamma)_{lab}^{iso,boosted} \times \delta_{\text{GEANT}} \times \frac{\int_{\theta_{pro}} W(\theta_{pro}) \sin\theta_{pro}\, d\theta_{pro}}{\frac{1}{4\pi}\int_{\theta_{pro}} \sin\theta_{pro}\, d\theta_{pro}}. \tag{B.15}$$

The range θ_{pro} over which the integral should be taken is only approximately known experimentally. A more precise way to determine the angular distribution and solid angle integrated over θ_{pro} is to take a sum over the emitted θ_{pro} angles of the detected gamma rays, weighted by the number of detected gamma rays at each angle. In order to calculate the weighted sums, two spectra are simulated that histogram the emitted θ_{pro} angles in the projectile frame for gamma rays that are subsequently detected in the 37° and 90° rings of the array (see Figure B.1). The integrals of Equation B.15 become sums, with the additional factor N_θ representing the number

of counts for each θ_{pro} in the GEANT histogram

$$\frac{\int_{\theta_{pro}} W(\theta_{pro}) \sin\theta_{pro}\, d\theta_{pro}}{\frac{1}{4\pi}\int_{\theta_{pro}} \sin\theta_{pro}\, d\theta_{pro}} = \frac{\sum_{\theta_{pro}} N_{\theta_{pro}} W(\theta_{pro}) \sin\theta_{pro}}{\frac{1}{4\pi}\sum_{\theta_{pro}} N_{\theta_{pro}} \sin\theta_{pro}}. \tag{B.16}$$

Values of $W(\theta_{pro})$ are calculated in steps of one degree from 0° to 180°.

The contribution to the total efficiency from the target absorption, for the GEANT simulation method, is included in the weighted sum taken over the calculated angular distributions. The contribution from the target absorption of emitted gamma rays can be seen in Figure B.1 for the 90° ring of detectors. At $\theta_{pro} \simeq 90°$ in the laboratory frame, and $\theta_{pro} \simeq 110°$ in the projectile frame, there is a noticeable drop in the number of detected gamma rays. As the angular distribution is weighted with the number of detected gamma rays, the target absorption effect is included in the sum over $W(\theta)$.

Thus the total efficiency for one ring of SeGA, using the method of GEANT simulations, is

$$\epsilon_{tot} = \epsilon(E_\gamma)_{lab}^{iso,boosted} \times \delta_{\text{GEANT}} \times \frac{\sum_{\theta_{pro}} N_{\theta_{pro}} W(\theta_{pro}) \sin\theta_{pro}}{\frac{1}{4\pi}\sum_{\theta_{pro}} N_{\theta_{pro}} \sin\theta_{pro}}. \tag{B.17}$$

Bibliography

[1] M. G. Mayer and J. H. D. Jensen. *Elementary Theory of Nuclear Shell Structure.* Wiley, New York, 1955.

[2] J. H. Kelley, D. R. Tilley, H. R. Weller, and C. M. Cheves. *Nucl. Phys.*, **564**:1, 1993.

[3] S. Raman, C. W. Nestor, Jr., and P. Tikkanen. *At. Data and Nucl. Data Tables*, **78**:1, 2001.

[4] C. Thibault, R. Klapisch, C. Rigaud, A. M. Poskanzer, R. Prieels, L. Lessard, and W. Reisdorf. *Phys. Rev. C*, **12**:644, 1975.

[5] E. K. Warburton, J. A. Becker, and B. A. Brown. *Phys. Rev. C*, **41**:1147, 1990.

[6] P. G. Hansen, A. S. Jensen, and B. Jonson. *Annu. Rev. Nucl. Part. Sci.*, **45**:591, 1995.

[7] H. Junde. *Nucl. Data Sheets*, **86**:315, 1999.

[8] N. Schulz, J. Chevallier, B. Haas, J. Richert, and M. Toulemonde. *Phys. Rev. C*, **8**:1779, 1973.

[9] H. Nakada, Takashi Sebe, and Takaharu Otsuka. *Nucl. Phys. A*, **571**:467, 1994.

[10] G. Kraus et al. *Phys. Rev. Lett.*, **73**:1773, 1994.

[11] Y. Yanagisawa et al. *AIP Conf. Proc.*, **455**:610, 1998.

[12] R. Serber. *Phys. Rev.*, **72**:1008, 1947.

[13] T. Kobayashi, O. Yamakawa, K. Omata, K. Sugimoto, T. Shimoda, N. Takahashi, and I. Tanihata. *Phys. Rev. Lett.*, **60**:2599, 1988.

[14] N. A. Orr et al. *Phys. Rev. Lett.*, **69**:2050, 1992.

[15] D. Bazin et al. *Phys. Rev. Lett.*, **74**:3569, 1995.

[16] J. H. Kelley, S. M. Austin, R. A. Kryger, D. J. Morrissey, N. A. Orr, B. M. Sherrill, M. Thoennessen, J. S. Winfield, J. A. Winger, and B. M. Young. *Phys. Rev. Lett.*, **74**:30, 1995.

[17] J. H. Kelley et al. *Phys. Rev. Lett.*, **77**:5020, 1996.

[18] D. Bazin et al. *Phys. Rev. C*, **57**:2156, 1998.

[19] T. Baumann et al. *Phys. Lett. B*, **439**:256, 1998.

[20] P. G. Hansen. *J. Phys. G*, **25**:727, 1999.

[21] J. A. Tostevin. *J. Phys. G*, **25**:735, 1999.

[22] A. Navin et al. *Phys. Rev. Lett.*, **81**:5089, 1998.

[23] T. Aumann et al. *Phys. Rev. Lett.*, **84**:35, 2000.

[24] V. Guimaraes et al. *Phys. Rev. C*, **61**:064609, 2000.

[25] A. Navin et al. *Phys. Rev. Lett.*, **85**:266, 2000.

[26] V. Maddalena et al. *Phys. Rev. C*, **63**:024613, 2001.

[27] J. Enders et al. *Phys. Rev. C*, **65**:034318, 2002.

[28] L. Chen, B. Blank, B. A. Brown, M. Chartier, A. Galonsky, P. G. Hansen, and M. Thoennessen. *Phys. Lett. B*, **505**:21, 2001.

[29] P. G. Hansen. *Phys. Rev. Lett.*, **77**:1016, 1996.

[30] G. J. Kramer, H. P. Blok, and L. Lapikás. *Nucl. Phys. A*, **679**:267, 2001.

[31] A. Bohr and B. R. Mottelson. *Nuclear Structure*, volume 1, page 420. World Scientific, New Jersey, 1998.

[32] G. R. Satchler. *Direct Nuclear Reactions*. Oxford University Press, New York, 1990.

[33] J. S. Winfield, S. M. Austin, G. M. Crawley, C. Djalali, C. A. Ogilvie, R. J. Smith, Z. Chen, and M. Torres. *Phys. Lett. B*, **203**:345, 1988.

[34] H. Esbensen and G. Bertsch. *Phys. Rev. C*, **64**:014608, 2001.

[35] G. Bertsch, H. Esbensen, and A. Sustich. *Phys. Rev. C*, **42**:758, 1990.

[36] K. Yabana, Y. Ogawa, and Y. Suzuki. *Nucl. Phys. A*, **539**:295, 1992.

[37] K. Hencken, G. Bertsch, and H. Esbensen. *Phys. Rev. C*, **54**:3043, 1996.

[38] A. E. L. Dieperink and Jr. T. de Forest. *Phys. Rev. C*, **10**:543, 1974.

[39] B. A. Brown, P. G. Hansen, B. M. Sherrill, and J. A. Tostevin. *Phys. Rev. C*, **65**:061601(R), 2002.

[40] B. A. Brown and B. H. Wildenthal. *Annu. Rev. Nucl. Part. Sci.*, **38**:29, 1988.

[41] E. K. Warburton and B. A. Brown. *Phys. Rev. C*, **46**:923, 1992.

[42] B. A. Brown. *International School of Heavy-Ion Physics, 4th Course: Exotic Nuclei*, page 1. (World Scientific, Singapore), 1998. edited by R. A. Broglia and P. G. Hansen.

[43] D. R. Semon et al. *Phys. Rev. C*, **53**:96, 1996.

[44] M. R. Bhat. *Nucl. Data Sheets*, **85**:415, 1998.

[45] R. J. Glauber. *Lectures in Theoretical Physics*, volume 1. Interscience, New York, 1959. p. 1.

[46] J. S. Al-Khalili, J. A. Tostevin, and I. J. Thompson. *Phys. Rev. C*, **54**:1843, 1996.

[47] L. Ray. *Phys. Rev. C*, **20**:1857, 1979.

[48] B. A. Brown, 2002. Private communication.

[49] C. R. Gould, D. P. Balamuth, P. F. Hinrichsen, and R. W. Zurmühle. *Phys. Rev.*, **188**:1792, 1969.

[50] K. E. Rehm et al. *Phys. Rev. Lett.*, **80**:676, 1998.

[51] B. M. Sherrill. *Nucl. Instr. and Meth. B*, **70**:298, 1992.

[52] J. A. Caggiano. *Spectroscopy of Exotic Nuclei with the S800 Spectrograph*. PhD thesis, Michigan State University, 1998.

[53] H. Scheit, T. Glasmacher, R. W. Ibbotson, and P. G. Thirolf. *Nucl. Instr. and Meth. A*, **422**:124, 1999.

[54] J. Yurkon, D. Bazin, W. Benenson, D. J. Morrissey, B. M. Sherrill, D. Swan, and R. Swanson. *Nucl. Instr. and Meth. A*, **422**:291, 1999.

[55] M. Berz, K. Joh, J. A. Nolen, B. M. Sherrill, and A. F. Zeller. *Phys. Rev. C*, **47**:537, 1993.

[56] B. V. Pritychenko. *Intermediate-Energy Coulomb Excitation of the Neutron-Rich Radioactive Isotopes* $^{26,28}Ne$, $^{28-31}Na$, $^{30-34}Mg$, $^{34,35}Al$, ^{33}Si *and* ^{34}P. PhD thesis, Michigan State University, 2000.

[57] GEANT. CERN library long writeup. Technical Report W5013, CERN, 1994.

[58] P. Schneider, K. H. Bodenmiller, and S. Buhl. *Z. Phys. A*, **272**:113, 1975.

[59] J. Blomqvist et al. *Z. Phys. A*, **322**:169, 1985.

[60] M. Ramhadne et al. *Phys. Lett. B*, **432**:22, 1998.

[61] D. Rudolph, C. Baktash, M. J. Brinkman, M. Devlin, H.-Q. Jin, D. R. LaFosse, L. L. Riedinger, D. G. Sarantites, and C.-H. Yu. *Eur. Phys. J. A*, **4**:115, 1999.

[62] R. Borcea et al. *Nucl. Phys. A*, **695**:69, 2001.

[63] V. Maddalena et al. *Nucl. Phys. A*, **682**:332c, 2001.

[64] J. A. Tostevin. *Nucl. Phys. A*, **682**:320c, 2001.

[65] W. F. Mueller, T. Glasmacher, D. Gutknecht, G. Hackman, P. G. Hansen, Z. Hu, K. L. Miller, and P. Quirin. *Nucl. Instr. and Meth. A*, **466**:492, 2001.

[66] J. Enders et al. *Phys. Rev. C*, in press, 2003.

[67] J. M. Kidd, P. J. Lindstrom, H. J. Crawford, and G. Woods. *Phys. Rev. C*, **37**:2613, 1988.

[68] D. L. Olsen, B. L. Berman, D. E. Greiner, H. H. Heckman, P. J. Lindstrom, and H. J. Crawford. *Phys. Rev. C*, **28**:1602, 1983.

[69] B. Blank et al. *Nucl. Phys. A*, **624**:242, 1997.

[70] D. Cortina-Gil et al. *Phys. Lett. B*, **529**:36, 2002.

[71] D. Cortina-Gil et al. *Eur. Phys. J. A*, **10**:49, 2001.

[72] W. Schwab et al. *Z. Phys. A*, **350**:283, 1995.

[73] V. R. Pandharipande, I. Sick, and P. K. A. deWitt Huberts. *Rev. Mod. Phys.*, **69**:981, 1997.

[74] K. Alder, A. Bohr, T. Huus, B. Mottelson, and A. Winther. *Rev. Mod. Phys.*, **28**:432, 1956.

[75] K. Alder and A. Winther. *Electromagnetic Excitation*. North-Holland, Amsterdam/Oxford, 1975.

[76] A. Winther and K. Alder. *Nucl. Phys. A*, **319**:518, 1979.

[77] C. A. Bertulani and G. Baur. *Phys. Rep.*, **163**:299, 1988.

[78] T. Glasmacher. *Annu. Rev. Nucl. Part. Sci.*, **48**:1, 1998.

[79] T. Motobayashi. *J. Phys. G*, **24**:1569, 1998.

[80] T. Glasmacher. *Nucl. Phys. A*, **693**:90, 2001.

[81] A. N. F. Aleixo and C. A. Bertulani. *Nucl. Phys. A*, **505**:448, 1989.

[82] S. S. M. Wong. *Introductory Nuclear Physics*. John Wiley & Sons, Inc., New York, 1998.

[83] H. Scheit. *Low-Lying Collective Excitations in Neutron-Rich Even-Even Sulfur and Argon Isotopes Studied via Intermediate-Energy Coulomb Excitation and Proton Scattering*. PhD thesis, Michigan State University, 1998.

[84] H. Olliver, 2003. Private communication.

[85] D. J. Morrissey, B. M. Sherrill, M. Steiner, A. Stolz, and I. Wiedenhoever. *Nucl. Instr. and Meth. B*, in press, 2003.

[86] K. L. Miller, T. Glasmacher, C. Campbell, L. Morris, W. F. Mueller, and E. Strahler. *Nucl. Instr. and Meth. A*, **490**:140, 2002.

[87] H. Junde. *Nucl. Data Sheets*, **90**:1, 2000.

[88] Y. Iritani, J. Kasagi, and H. Ohnuma. *J. Phys. Soc. Jap.*, **43**:1119, 1977.

[89] C. Zhou. *Nucl. Data Sheets*, **76**:399, 1995.

[90] L. Riley, 2003. Private communication.

[91] J. Raynal. *Phys. Rev. C*, **23**:2571, 1981.

[92] T. Suomijärvi et al. *Nucl. Phys. A*, **509**:369, 1990.

[93] M. R. Bhat. *Nucl. Data Sheets*, **80**:789, 1997.

[94] K. Langanke, D. J. Dean, P. B. Radha, Y. Alhassid, and S. E. Koonin. *Phys. Rev. C*, **52**:718, 1995.

[95] T. Otsuka, M. Honma, and T. Mizusaki. *Phys. Rev. Lett.*, **81**:1588, 1998.

[96] M. Honma, T. Otsuka, B. A. Brown, and T. Mizusaki. *Phys. Rev. C*, **65**:061301, 2002.

[97] P. Hornshoj, L. Hojsolt-Poulsen, and N. Rud. *Nucl. Phys. A*, **288**:429, 1977.

[98] J. Äystö et al. *Phys. Lett. B*, **138**:369, 1984.

[99] D. Mueller, E. Kashy, and W. Benenson. *Phys. Rev. C*, **15**:1282, 1977.

[100] D. Rudolph et al. *Z. Phys. A*, **358**:379, 1997.

[101] H. Junde. *Nucl. Data Sheets*, **64**:723, 1991. Updated 2001.

[102] P. M. Endt. *At. Data and Nucl. Data Tables*, **23**:547, 1979.

[103] I. Reusen et al. *Phys. Rev. C*, **59**:2416, 1999.

[104] M. Honma and B. A. Brown, 2003. Private communication.

[105] T. Mizusaki. *RIKEN Accel. Prog. Rep.*, **33**:14, 2000.

[106] B. A. Brown and B. H. Wildenthal. *Phys. Rev. C*, **21**:2107, 1980.

[107] D. Radford, 2001. http://radware.phy.ornl.gov.

[108] PAW, 2002. http://paw.web.cern.ch/paw.